1 # Measurement of ν_e CC $\pi+$ cross section using the ND280 tracker and development of optical diffuser calibration systems for Hyper-Kamiokande

by

Sammy Lee Valder

Thesis

Submitted to the University of Warwick

in partial fulfilment of the requirements

2 for admission to the degree of

Doctor of Philosophy

Department of Physics

August 2020

Contents

List of Tables

List of Figures

Acknowledgments

Thanks go here.

Declarations

Parts of this thesis have been previously published by the author in the following:

[?]

Research was performed in collaboration during the development of this thesis, but does not form part of the thesis:

[?]

Abstract

Over the last few decades our understand of the physics that governs neutrino oscillations has evolved rapidly through an experimental program designed to measure the key parameters behind neutrino oscillations. This thesis provides an overlook into the Tokai to Kamioka (T2K) long baseline accelerator neutrino experiment, and the next generation water Cherenkov detector Hyper-Kamiokande; both designed to make precise measurements on neutrino oscillation parameters. In the T2K far detector a data excess is seen in the ν_e charged current π^+ sample, a significant channel in electron neutrino appearance studies. An analysis is presented in this thesis to investigate ν_e charged current π^+ production using the off-axis near detector (ND280) tracker of the T2K experiment. A novel selection has been developed and the systematic uncertainties evaluated to measure a flux average cross-section of $\sigma = (2.23 \pm 0.39(\text{stat.}) \pm 0.38(\text{syst.})) \times 10^{-39}$ cm^2 per nucleon. This result provides the first ever cross-section measurement of ν_e charged current π^+ production on a carbon target. With kinematic constraints applied, analogous to the far detector sample, preliminary studies indicate no data excess in the near detector sample.

Unfinished...

Sponsorships and Grants

Acronyms

CC Charged Current.

CP Charge-Parity.

HK Hyper-Kamiokande.

INGRID Interactive Neutrino GRID.

MR Main Ring.

NC Neutral Current.

ND280 Near Detector at 280 m.

SK Super-Kamiokande.

T2K Tokai-to-Kamioka.

Symbols

δ_{CP} Charge-Parity violating phase factor

Chapter 1

Introduction

From the postulation of the neutrino to the proposals of next generation detectors, the field of neutrino physics has continuously evolved throughout it's 90 year history. Neutrinos are the weak isospin partners of the standard model charged leptons. Existing in three flavour states, neutrinos are electrically neutral, extremely light, and interact with other particles exclusively via the weak interaction. Nevertheless, the neutrino is not feted for its place in the standard model, but rather its role in conclusively confirming the standard model was incomplete. At the turn of the 21st century, a series of discoveries provided experimental proof for neutrino oscillations. The standard model of particle physics predicts neutrinos to be massless [1]. However, the underlying theory for neutrino oscillations requires neutrinos to be massive, which is in direct contradiction to the standard model. Such a discovery provided one of the first experimental indications of physics beyond the standard model.

Over the last two decades an experimental program to measure the key parameters that govern neutrino oscillations has been undertaken. Global fits are applied to data, collated across a number of experiments, to give constraints on best fit values for the oscillation parameters. These parameters, which are defined and discussed in detail in Chapter 2, are summarised for the three-flavour neutrino picture in table 1.1. Different experiments have varying sensitivities to different oscillation parameters, often characterised by the source of neutrino (solar, atmospheric, reactor, accelerator). An overview of which types of experiments contribute to the present determination of oscillation parameters is shown in table

Oscillation Parameter	Normal Ordering		Inverted Ordering	
	Best Fit $\pm 1\sigma$	3σ Range	Best Fit $\pm 1\sigma$	3σ Range
$\sin^2\theta_{12}/10^{-1}$	$3.10^{+0.13}_{-0.12}$	$0.275 \to 0.350$	$3.10^{+0.13}_{-0.12}$	$0.275 \to 0.350$
$\theta_{12}/^\circ$	$33.82^{+0.78}_{-0.76}$	$31.61 \to 36.27$	$33.82^{+0.78}_{-0.75}$	$31.61 \to 36.27$
$\sin^2\theta_{23}/10^{-1}$	$5.82^{+0.15}_{-0.19}$	$0.428 \to 0.624$	$5.82^{+0.15}_{-0.18}$	$0.433 \to 0.623$
$\theta_{23}/^\circ$	$49.7^{+0.9}_{-1.1}$	$40.9 \to 52.2$	$49.7^{+0.9}_{-1.0}$	$41.2 \to 52.1$
$\sin^2\theta_{13}/10^{-1}$	$2.240^{+0.065}_{-0.066}$	$2.044 \to 2.437$	$2.263^{+0.065}_{-0.066}$	$2.067 \to 2.461$
$\theta_{13}/^\circ$	$8.61^{+0.12}_{-0.13}$	$8.22 \to 8.98$	$8.65^{+0.12}_{-0.13}$	$8.27 \to 9.03$
$\delta_{CP}/^\circ$	217^{+40}_{-28}	$135 \to 366$	280^{+25}_{-28}	$196 \to 351$
$\Delta m^2_{21}/10^{-5}$ eV^2	$7.39^{+0.21}_{-0.20}$	$6.79 \to 8.01$	$7.39^{+0.21}_{-0.20}$	$6.79 \to 8.01$
$\Delta m^2_{32}/10^{-5}$ eV^2	$2.525^{+0.033}_{-0.031}$	$+2.431 \to +2.622$	$-2.512^{+0.034}_{-0.031}$	$-2.606 \to -2.413$

Table 1.1: The best fit 3ν oscillation parameters (from nu-fit [2]) to global data, published in 2019 [3]. Values assuming both normal ordering (NO) and inverted ordering (IO) are shown. All values shown been calculated to include tabulated Super-K atmospheric data measurements [4].

1.2. Reactor experiments measuring $\bar{\nu}_e$ disappearances from inverse β-decay provide excellent constraints on θ_{13}, especially with a short-medium baseline on the order of 1 km. Solar experiments have primary sensitivity to θ_{12} and Δm^2_{21}. Longer baseline reactor experiments, such as KamLAND [5], also have sensitivity to Δm^2_{21}. Both reactor and Solar experiments measure neutrinos in the few-MeV energy range. With a wide range of oscillation baselines, atmospheric neutrino experiments have sensitivity to most oscillation parameters but focus primarily on Δm^2_{32} and θ_{23}. Atmospheric experiments measure neutrinos through the decays of π and K mesons created through cosmic ray interactions with the Earth's atmosphere. Long baseline accelerator neutrino experiments use a beam of pure $\nu_\mu(\bar{\nu}_\mu)$ to measure $\nu_\mu(\bar{\nu}_\mu)$ disappearances, as well as $\nu_e(\bar{\nu}_e)$ appearances, at far detectors situated on baselines $O(100$ km). Measuring neutrinos on the GeV-scale, they have sensitivity to θ_{13}, θ_{23}, Δm^2_{31}, Δm^2_{32}, and δ_{CP}. Long baseline accelerator experimentation is the primary neutrino detection method used within thesis.

The 20-30 years have seen a revolution in neutrino physics. Major recent accomplishments include the establishment of non vanishing neutrino masses in

Experiment	Dominant	Important
Solar Experiments	θ_{12}	Δm^2_{21}, θ_{13}
Reactor LBL (KamLAND)	Δm^2_{21}	θ_{12}, θ_{13}
Reactor MBL (Daya-Bay, Reno, D-Chooz)	θ_{13}, $\lvert\Delta m^2_{31,32}\rvert$	
Atmospheric (SK, IC-DC)		θ_{13}, θ_{23}, $\lvert\Delta m^2_{31,32}\rvert$, δ_{CP}
Accel. LBL ν_μ, $\bar{\nu}_\mu$ Dissapp. (K2K, MINOS, T2K, NOνA)	θ_{23}, $\lvert\Delta m^2_{31,32}\rvert$	
Accel. LBL ν_e, $\bar{\nu}_e$ App. (MINOS, T2K, NOνA)	δ_{CP}	θ_{13}, θ_{23}

Table 1.2: The different experiments contributing to the current determination of bes fit oscillation parameters. LBL and MBL define long and medium baselines respectively. Reproduced from [1].

oscillation experiments, which in turn has lead to a solution to missing solar neutrinos. Nevertheless, there are are several fundamental question that remain unanswered. Most notably is the existence, and magnitude, of CP violation in the leptonic sector. CP violation is primarily characterised by the δ_{CP} parameter. Currently T2K and NOνA have sensitivity to δ_{CP} and can provide hints and constraints on the magnitude, but do not have the sensitivity to confirm CP-violation. The future long baseline neutrino experiments Hyper-Kamiokande and DUNE, with larger detectors and more sophisticated detection techniques, have the measurement of δ_{CP} as a primary goal.

The objectives of this thesis can be summarised in two distinct projects: The first is a cross-section measurement to constrain far detector processes using near detector data; the second is a research and development project in optical calibration of water Cherenkov detectors. Both projects are allied towards a common overarching experimental goal of constraining and measuring CP-violation in long baseline neutrino experiments. In detail, chapter 2 will begin with a brief history of experimental neutrino physics, before delving into a discussion of the theoretical models behind neutrino oscillations and neutrino-nucleus interactions. Detailed overviews of the current long baseline water Cherenkov accelerator experiment T2K, and the next generation sister experiment Hyper-Kamiokande, are provided in chapters 3 and 5 respectively. The first measurement of the ν_e CC π^+ interaction cross-section on a carbon target is introduced in chapter 4, and provides the preliminary insights into data excesses observed in the T2K far detector. Chapter 6 summarises the research and development into diffuser technology for optical calibration systems currently proposed for Hyper-Kamiokande. This chapter will examine the performance of diffuser systems in the context of both laboratory measurements, and recent deployments in the Super-Kamiokande detector. Finally, chapter 7 will discuss the research and results presented throughout the thesis, closing with a summary of potential avenues for future research.

Chapter 2

Background

2.1 A Brief History of Neutrinos

The postulation and eventual discovery of the neutrino arose from interrogating the method in which beta decay occurs. In 1930 the beta decay process was thought of as being the transition of a neutron to proton with the emission of an electron in the form:

$$^{A}_{Z}N \rightarrow \, ^{A}_{Z+1}N' + e^{-} \tag{2.1}$$

As an example of a two-body decay process, conservation of energy and momentum requires the energy spectrum for the emitted electron to be theoretically monotonic in shape, appearing likely as a sharp peak. Despite this, empirical data revealed the observed energy spectrum was a wide distribution symptomatic of a 3-body decay. A continuous distribution contradicting the 2-body decay picture thus caused a significant problem for the scientific community at the time. Furthermore, the suggested beta decay process also violated angular momenta conservation when including spin, as a single spin $\frac{1}{2}$ particle cannot produce a final state consisting of exactly two spin $\frac{1}{2}$ particles.

Later in that year, Wolfgang Pauli would propose a solution to this problem. Pauli postulated the existence of a third outgoing particle, which he christened the "neutron", thereby generating a three-body decay process. This third particle would take the form of a neutral fermion and was hypothesised to be light and minimally interacting. In 1932 the term "neutron" was given to the newly discovered neutral nucleon, and thus from then on Pauli's particle was known as the neutrino - meaning "little neutral one" in Italian.

Given the neutrinos weakly interacting nature, it took a further 20 years for the first experimental evidence of the neutrino's existence. Published in 1952, Rodeback and Allen used the electron capture of ^{37}Ar to measure the recoil energy of the nucleus [6]. But it wasn't until 1956 and the advent of nuclear fission reactors that Reines and Cowan published the discovery of the neutrino [7]. Reines and Cowan used close proximity with the Savannah River nuclear reactor, among the strongest source of (anti)neutrinos at the time, to measure the reaction:

$$\bar{\nu}_e + p \rightarrow e^+ + n \tag{2.2}$$

A coincidence of the 511 keV photon associated with the outgoing positron annihilation and a neutron capture reaction a few μs later would signal a detection. The experiment consisted of a water tank with dissolved $CdCl_2$. Surrounding the tank two liquid scintillators were used to detect both the photons produced from the positron annihilation, as well as from the ^{113}Cd(n,γ)^{114}Cd reaction after neutron capture [8]. The experiment demonstrated that an increased signal was seen when the reactor was running relative to when it was dormant, an observation attributed to the neutrino's discovery. Reines' and Cowan's achievement would be acknowledged with Frederick Reines receiving the 1995 Nobel Prize in Physics, 21 years after the death of Clyde Cowan.

Reines and Cowan had successfully discovered the anti-electron neutrino ($\bar{\nu}_e$) yet the story wasn't finished. In 1962 at the Brookhaven National Laboratory, the muon neutrino (ν_μ) was discovered [9]. The experiment used a proton beam to produce pions which subsequently decay to muons and muon (anti)neutrinos[1]:

$$\pi^\pm \rightarrow \mu^\pm + \overset{(-)}{\nu}_\mu \tag{2.3}$$

[1] Note the similarity to the muon neutrino beam approach used by T2K contributing to the work presented throughout this thesis.

Brookhaven detected the resulting muon (anti)neutrinos using an aluminium spark chamber. The sole production of only one flavour of neutrino demonstrated that neutrino flavour states are distinct; work that lead to Ledermen, Schwartz, and Steinberger receiving the 1988 Nobel Prize in Physics.

By the late 1970's three different lepton flavours had been discovered; in contrast, despite two more decades passing, only two flavours of neutrinos were known to exist. It therefore came as no surprise when the Large Electron Positron collider (LEP) at CERN hinted at the existence of three light active neutrino flavour states [10]. Over the next decade, searches for the missing neutrino ensued, coming to an end in the new millennium when the DONUT (Direct Observation of NU Tau) experiment discovered the ν_τ [11].

2.1.1 Discovery of Neutrino Flavour Mixing

Solar Neutrino Problem

With the discovery of the electron neutrino and the new understanding of the Sun's nuclear engine through solar models, Ray Davies was inspired to study solar neutrinos as a means of observing the heart of the Sun [12]. Davies headed the Homestake experiment [13], named after the gold mine in which it was located 1,500 m underground. Homestake used a tank filled with pure C_2Cl_4 to observe an inverse beta decay process converting the chlorine to argon via:

$$^{37}\mathrm{Cl} + \nu_e \rightarrow {}^{37}\mathrm{Ar} + e^- \tag{2.4}$$

^{37}Ar has a half-life of approximately 35 days; radioactive decay results in 2.82 keV X-rays or Auger electrons from K-capture at a ratio of 10:90 [14]. Roughly once a month the argon atoms were extracted by bubbling helium through the tank. The electron neutrino flux was then estimated through the detection of it's radioactive decay products. Homestake observed neutrinos at a significantly lower rate than accurate solar models could predict. This observation was further supported by other experiments such as GALLEX [15] and SAGE [16]. Both experiments used inverse-beta decay of gallium into germanium:

$$^{71}\mathrm{Ga} + \nu_e \rightarrow {}^{71}\mathrm{Ge} + e^- \tag{2.5}$$

By using gallium these experiments had access to lower energy higher flux neutrinos from the pp-chain in which Homestake was blind to. The lower energy threshold relative to other experimental targets, such as chlorine (Homestake) and water (Super-K), can be seen in figure 2.1. Interestingly, GALLEX and SAGE observed smaller deficits which would suggest an energy dependence. Nevertheless all experiments saw large discrepancies with the standard solar model, which became known as the "solar neutrino problem".

Atmospheric Neutrino Anomaly

Somewhat ironically the solution for the solar neutrino problem wouldn't begin by probing the Sun as a source, rather it would start through exploring neutrinos from our very own atmosphere. Importantly, for chlorine and gallium experiments the vast majority of solar neutrinos studied were below an energy threshold for ν_μ and ν_τ charged current interactions. This can be seen in figure 2.1. Therefore previous solar neutrino experiments had sensitivity only to (anti)electron neutrinos. Atmospheric experiments however can observe multiple neutrino flavours produced from muon decays in the atmosphere. In particular a double ratio, consisting of the ratio of the rstio of predicted to measured rate of ν_μ to ν_e events, was measured. Super-Kamiokande (SK), described in section 3.4, discovered that the double ratio was lower than expected and the neutrino flux was a function of the zenith angle [18]. Lower ratios was an indication of either ν_μ disappearance or ν_e appearance. Furthermore, changing the zenith angle is equivalent to varying the distance in which the neutrino propagates, thus implying the flux has a dependence on distance travelled. A combination of these two phenomena led to the proposal of neutrino oscillations.

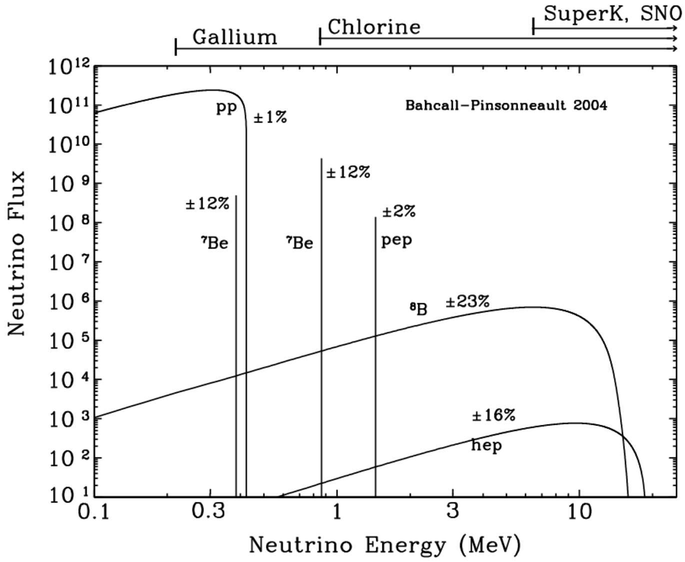

Figure 2.1: The neutrino flux emission as a function of neutrino energy for different fusion processes within the Sun. Regions of neutrino energy space in which experimental detectors are sensitive is also shown. Taken from [17].

.

Evidence of Neutrino Oscillations

If previous atmospheric and solar neutrino experiments were not able to measure ν_μ and ν_τ through charged current interactions, perhaps it would be possible via neutral current (NC) interactions. The Sudbury Neutrino Observatory (SNO) aimed to accomplish this through the use of heavy water as a target [19]. SNO aimed to detect solar neutrinos using Cherenkov radiation much like Super-Kamiokande. The use of heavy water however allowed SNO to exploit the flavour insensitive NC interactions on the deuterium:

$$\nu_x + {}^2D \rightarrow \nu_x + p + n \tag{2.6}$$

Whereby x can be anyone of the three neutrino flavour states. Furthermore the neutrons produced can interact with another deuteron, producing tritium and importantly a 6.3 MeV photon.

$$n + {}^2D \rightarrow {}^3T + \gamma \tag{2.7}$$

The interaction's flavour neutrality stems from the fact no charged leptons are produced. Coincidences between the interactions in equations 2.6 and 2.7 could be identified and tagged as NC events. The rate of neutral current interactions seen by SNO matched that predicted by the solar models [19]. This led to the conclusion that unseen neutrinos of previous experiments were not "missing", rather they couldn't be detected as the neutrinos had changed flavour states through oscillations. Moreover, SNO also probed charged current interactions and, much like experiments before, measured a deficiency in neutrino flux. A combination of these two findings led to the discovery of flavour changing neutrino oscillations [20] and the awarding of Nobel Prize in Physics to Takaaki Kajita (Super-K) and Arthur McDonald (SNO) in 2015.

2.1.2 The LSND Anomaly and Sterile Neutrinos

The Liquid Scintillator Neutrino Detector (LSND) [21, 22] was an experiment that took data from 1993-1998. LSND measured $\nu_\mu \rightarrow \nu_e$ oscillations over a short baseline, using a 167 t mineral-oil-based liquid scintillator detector with a cylindrical geometry. An excess on the predicted number of oscillations was observed at low energies, which has subsequently become known as "the LSND anomaly". The result was inconsistent with the atmospheric and solar results in a three-flavour model. Furthermore, confirmation of only three weakly interacting neutrinos, lighter than half of the Z^0 boson mass, existed from the LEP experiment [23]. The LSND anomaly needed a fourth neutrino generation that was unable to couple with the weak force; this became known as sterile neutrino.

Experiments have since attempted to test the LSND result. Most notably the MiniBooNE [24, 25] at FermiLab, uses a 0.8 kt mineral oil Cherenkov detector over a short baseline in an attempt to measure the same excess in low energy $\nu_\mu \rightarrow \nu_e$ oscillations. Whilst an excess of low energy electron-like CCQE events was found [26], the signal produced by electrons and converted photons is indistinguishable. Some have suggested this could explain the original LSND anomaly, nevertheless searches for the sterile neutrino are ongoing.

2.2 Neutrino Oscillation Theory

The solution of the solar neutrino problem described in section 2.1.1 provided strong evidence the neutrinos have mass. For non-vanishing rest masses, the weak and mass eigenstates are not necessarily identical. This is a phenomena that has already been studied and observed in great detail in the quark sector whereby the relationship between flavour and mass states is governed by the Cabibbo-Kobayashi-Maskawa (CKM) matrix [27]. Pontecorvo drew analogy to the previously observed $K^0 \rightarrow \bar{K^0}$ mixing and suggested that neutrinos could oscillate in a similar manner, if their flavour and mass states were different [28]. The analogous $\nu \rightarrow \bar{\nu}$ process has not yet been observed, but it did lay the foundation to which a full theory of neutrino oscillations was formed[2].

A more general formalism without constraints on the number of flavour states for neutrino oscillations can be found at [29], and sophisticated derivations performed using quantum field theory can be found here [30, 31]. For the purpose of this discussion it is acceptable to simplify the picture to one considering the more experimentally relevant case of three different lepton flavour states ($|\nu_\alpha\rangle$, $\alpha = e, \mu, \tau$). Neutrinos interact solely in these flavour states, and only propagate in the three neutrino mass eigenstates ($|\nu_i\rangle$, $i = 1, 2, 3$). The flavour and mass eigenstates are connected via the unitary mixing matrix, U:

$$|\nu_\alpha\rangle = \sum_i U_{\alpha i} |\nu_i\rangle \tag{2.8}$$

In the case of antineutrinos, $U_{\alpha i}$ has to be replaced by it's complex conjugate such that:

$$|\bar{\nu}_\alpha\rangle = \sum_i U^*_{\alpha i} |\bar{\nu}_i\rangle \tag{2.9}$$

This unitary matrix, U, is known as the PMNS (Pontecorvo-Maki-Nakagawa-Sakata)

[2] It should be noted that such oscillations through neutrino flavours do not conserve individual lepton flavour numbers, only conserving total lepton number

matrix, and can be written in full generality as:

$$U = \begin{bmatrix} U_{e1} & U_{e2} & U_{e3} \\ U_{\mu 1} & U_{\mu 2} & U_{\mu 3} \\ U_{\tau 1} & U_{\tau 2} & U_{\tau 3} \end{bmatrix} \tag{2.10}$$

$$= \begin{bmatrix} 1 & 0 & 0 \\ 0 & c_{23} & s_{23} \\ 0 & -s_{23} & c_{23} \end{bmatrix} \begin{bmatrix} c_{13} & 0 & s_{13}e^{-i\delta_{CP}} \\ 0 & 1 & 0 \\ -s_{13}e^{i\delta_{CP}} & 0 & c_{13} \end{bmatrix} \begin{bmatrix} c_{12} & s_{12} & 0 \\ -s_{12} & c_{12} & 0 \\ 0 & 0 & 1 \end{bmatrix} \begin{bmatrix} e^{i\alpha_1/2} & 0 & 0 \\ 0 & e^{i\alpha_2/2} & 0 \\ 0 & 0 & 1 \end{bmatrix} \tag{2.11}$$

Here the terse notation $c_{\alpha\beta} = \cos(\theta_{\alpha\beta})$ and $s_{\alpha\beta} = \sin(\theta_{\alpha\beta})$ is used for simplicity. The off-diagonal terms in the PMNS matrix give rise to neutrinos being created in a superposition of mass states. This mixing of states means that there is a finite possibility that a neutrino created in one flavour state may be observed sometime later as a different flavour state. Neutrinos can therefore be considered to change their flavour state through propagation. This is known by the more common term "neutrino oscillations".

The unitary matrix, U, can be written as the product of four sub-matrices as demonstrated above. The initial three sub-matrices are separated to contain different respective mixing angles $(\theta_{12}, \theta_{13}, \theta_{23})$. Distinct types of neutrino experiments exploit different sensitivities to each of the mixing angles. Solar and atmospheric neutrino experiments constrain values for θ_{12} and θ_{23} respectively. Reactor neutrino experiments have sensitivity to θ_{13} and θ_{12}. Whereas accelerator neutrino experiments can measure θ_{13} and θ_{23}. Furthermore the submatrix containing θ_{13} also contains a Dirac CP-violating phase (δ_{CP}) in which reactor and accelerator neutrino experiments will also have sensitivity to.

The fourth matrix is included only if neutrinos are considered as Majorana particles. It contains an additional two Majorana CP-violating phases (α_1 and α_2), but will only have physical consequences if neutrinos are their own antiparticle. Nevertheless it should be noted that even if neutrinos are Majorana, neutrino oscillations are unaffected by the Majorana CP-violating phases since oscillation probability only has a dependence on UU^*, where the Majorana phases cancel out.

2.2.1 Flavour Oscillation Probability

When it comes to neutrino oscillation experiments it is important to design the experiment to maximise the probability of oscillations. Using natural units (i.e. $\hbar = c = 1$) the mass eigenstates of the neutrinos $|\nu_i(x,t)$ are stationary states and can be modelled with a time dependence of

$$|\nu_i(x,t)\rangle = e^{-iE_it}|\nu_i(x,0)\rangle \tag{2.12}$$

assuming that the neutrinos are emitted by a source from $x = 0$ at time $t = 0$ with momenta p, it is possible to rewrite this equation as

$$|\nu_i(x,0)\rangle = e^{ipx}|\nu_i(x,t)\rangle \tag{2.13}$$

given the neutrinos are relativistic it is safe to make the assumption that $p \gg m_i$ and the total neutrino energy $E \approx p$. Therefore the energy of the propagating neutrino can be written as

$$\begin{aligned} E_i &= \sqrt{m_i^2 + p_i^2} \\ &\simeq p_i + \frac{m_i^2}{2p_i} \\ &\simeq E + \frac{m_i^2}{2E} \end{aligned} \tag{2.14}$$

using this and $t \approx L$, whereby L is the distance travelled by the neutrino, equation 2.12 can be rewritten as

$$|\nu_i(L)\rangle = e^{-im_i^2L/2E}|\nu_i(0)\rangle \tag{2.15}$$

illustrating that different neutrino masses aquire a different phase factor. Because neutrinos are produced and detected only as flavour states, the neutrino with flavour

$|\nu_\alpha\rangle$ emitted by a source at $t = 0$ propagates in time into a state $|\nu_\beta\rangle$ by

$$|\nu(x,t) = \sum_i U_{\alpha i} e^{-iE_i t} |\nu_i\rangle = \sum_{i,\beta} U^*_{\beta i} U_{\alpha i} e^{ipx} e^{-E_i t} |\nu_\beta\rangle \tag{2.16}$$

Combining the two equations previous, the amplitude $A_{\alpha\to\beta}$ and thus probability $P_{\alpha\to\beta}$ of neutrino oscillation from state α to state β can be calculated as

$$P_{\alpha\to\beta} = |A_{\alpha\to\beta}|^2 = |\langle\nu_\beta(t)|\nu_\alpha\rangle|^2 = \left|\sum_i U^*_{\beta i} U_{\alpha i} e^{-im_i^2 L/2E}\right|^2 \tag{2.17}$$

expanding out, the transition probability becomes

$$\begin{aligned} P(\alpha\to\beta) &= \sum_i \sum_j U_{\alpha i} U^*_{\alpha j} U^*_{\beta i} U_{\beta j} e^{-i(E_i - E_j)t} & (2.18) \\ &= \sum_i |U_{\alpha i} U^*_{\beta i}|^2 + 2Re \sum_{j>i} U_{\alpha i} U^*_{\alpha j} U^*_{\beta i} U_{\beta j} \exp\left(-i \frac{\Delta m^2_{ij}}{2}\right) \frac{L}{E} & (2.19) \end{aligned}$$

whereby $\Delta m^2_{ij} = m_i^2 - m_j^2$. The first term in equation 2.19 represents the average transition probability; the second term describes the time (or spacial) dependence of the flavour oscillation. Assuming CP invariance and taking only real terms we can simplify equation 2.19 to

$$P(\alpha\to\beta) = \delta_{\alpha\beta} - 4 \sum_{j>i} U_{\alpha i} U_{\alpha j} U_{\beta i} U_{\beta j} \sin^2\left(\frac{\Delta m^2_{ij}}{4} \frac{L}{E}\right) \tag{2.20}$$

This derivation means that the flavour content of the final state differs from that of the initial state. Moreover, it demonstrates the importance of neutrino mass differences in oscillations. Despite the small difference in neutrino masses the effect can still be large at macroscopic distances. Furthermore, it can now be seen from equations 2.19 and 2.20 that three flavour neutrino oscillations can be described by a CP-violating phase term and mixing angles from the PMNS matrix, combined with the neutrino mass state differences. These are the parameters neutrino oscillation experiments aim to measure.

2.2.2 CP Violation

A primary objective of neutrino oscillation experiments is confirmation and measurement of CP-violation is the leptonic sector. To explain what CP-violation is, a quantum mechanical charge conjugate operator, $\hat{C}$, must first be introduced. The operator has the function of replacing particles with their anti-particle counterparts.

$$q \rightarrow -q \tag{2.21}$$

Here the charged carried by the particle is given as q. With one half of CP represented, it is natural now to define a parity operator, $\hat{P}$, which reverses the sign of spatial dimensions:

$$t \rightarrow t \qquad x \rightarrow -x \qquad y \rightarrow -y \qquad z \rightarrow -z \tag{2.22}$$

The eigenvalues of these operators can hold values of ± 1. This is because the operators returns the original value when applied twice, i.e. $\hat{C}^2 = \hat{P}^2 = 1$. In particular, the eigenvalues of the charge conjugate is obtain through the product of the $\hat{C}$ eigenvalues of its components. The $\hat{C}$ eigenvalue is more commonly known as C-parity; by convention, fermions and anti-fermions are given a parity of $+1$ and -1 respectively.

The standard model conserves parity and C-parity in EM and strong interactions. However, weak interactions have been observed to violate parity [32]. The product of C-parity and parity is often referred to as CP. Evidence of CP violation in the quark sector has been observed through Kaon decays via a minority of weak interactions [33, 34]. The search for CP violation in the leptonic sector is a major goal for particle physics, including neutrino oscillation experiments. CP violation, alongside Baryon number and C-symmetry violation, is one of the processes that could help understand the observed matter anti-matter asymmetry seen in the universe.

2.2.3 Matter Effects

When considering experimental searches for neutrino oscillation parameters, one must consider that all neutrino oscillation experiments require neutrinos to pass

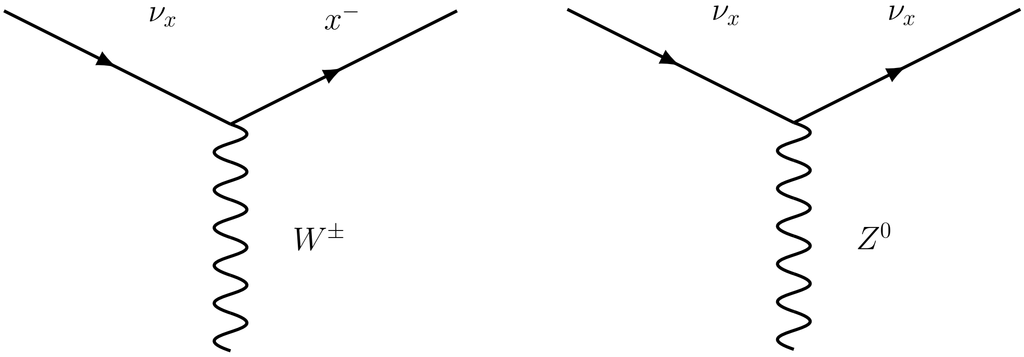

(a) Charged Current Interaction

(b) Neutral Current Interaction

Figure 2.2: Feynman diagrams for the different types of electroweak interactions neutrinos can experience.

through matter either at the source, and/or through the Earth. Neutrinos are susceptible to interactions as they pass through matter, this will modify the vacuum oscillation probablities we discussed in section 2.2. In particular, as neutrinos travel through the Sun or the Earth, ν_e can experience neutral current and charged current scatterings with leptons because of the existence of electrons in the propagation medium. Conversely ν_μ and ν_τ can only interact via neutral current scatterings. These interactions are represented in figure 2.2.

As was shown in equation 2.20, neutrino oscillations in a vacuum are only sensitive to the magnitude square of the neutrino mass splittings, $|\Delta m^2_{ij}|$. In addition, matter effects also have sensitivity to the signs of the mass splitting. This helps experiments determine the ordering (i.e. heaviest to lightest) in which the neutrino mass states occur. Using solar neutrino observations it has been determined that the mass state ν_2 is larger in value to that of ν_1 [35]. Nevertheless, whilst measurements of atmospheric mass splitting (Δm^2_{31}) have been made [36], it is not yet known whether ν_3 is the heaviest or lightest of the three neutrinos. These two occurrences are more commonly referred to as 'normal neutrino mass ordering' and 'inverted neutrino mass ordering' respectively, and is demonstrated in figure 2.3. The neutrino mass ordering problem is currently one of the most active areas of research and interesting questions to the field of neutrino physics. The next generation of neutrino oscillation experiments aim to exploit matter effects within the Earth to resolve the mass ordering picture.

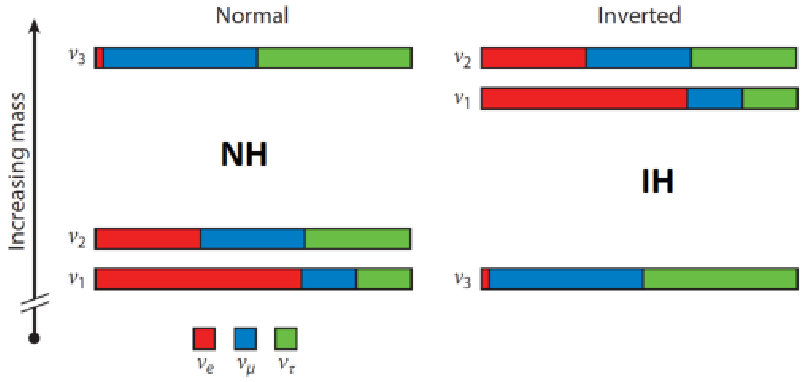

Figure 2.3: An illustration demonstrating the normal hierarchy (NH) and inverted hierarchy neutrino mass orderings. The relative proportions of flavour sharing due to mixing is also shown for each mass eigenstate. Figure is taken from [37].

Interestingly, antineutrinos cannot interact via the charged current channel shown in figure 2.2a. This has big implications on how the matter effect alters any neutrino oscillation measurement. In particular, this could induce an inequality in the probability for neutrino and antineutrino oscillations which one could determine to be a form of CP violation. However, this discrepancy does not inform us of the fundamental asymmetries in matter and antimatter that neutrino experiments are trying to observe. Therefore it is paramount that matter effects are taken into account when constraining values on CP violating phase factors such as δ_{CP}.

2.3 Neutrino-Nucleus Interactions

It is thought that in the near future the limiting factor in precise neutrino oscillation parameter measurements will be the systematic uncertainties in neutrino nucleus interactions. The topic of neutrino interactions is vastly complex, particularly for intermediate energies between approximately 0.1-20 GeV. In this energy region there are multiple processes competing against one another, as shown in figure 2.4. Within the lower and higher energy regions charged current quasi-elastic (CCQE) and deep inelastic scattering (DIS) processes are dominant; an important contribution to the total ν-N cross-section within the intermediate range are resonance (RES) processes. Additionally, a primary neutrino interaction can interact with multiple different components within the nucleus; a neutrino could interact with a parton, a single

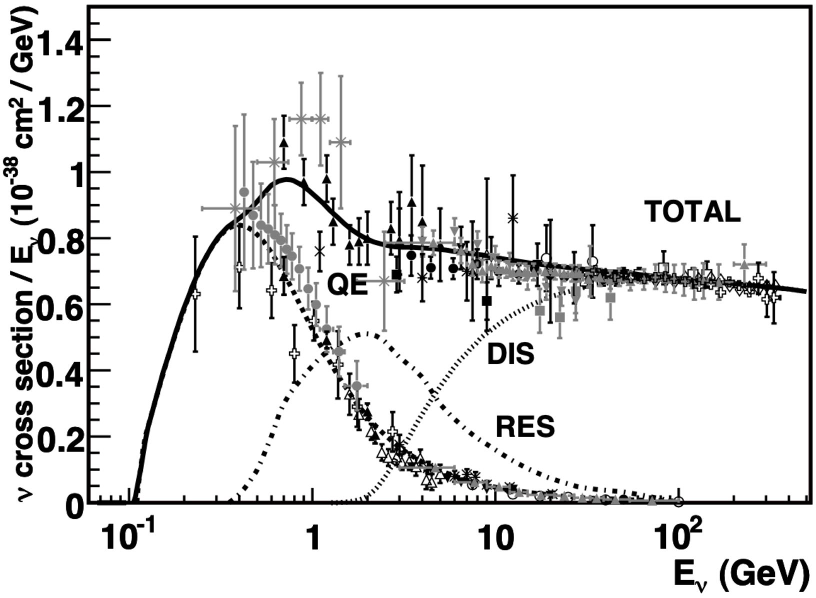

Figure 2.4: The total ν_μ cross section as a function of neutrino energy. The contributions of constituent the interaction modes; quasi-elastic (QE), deep inelastic scattering (DIS), and resonance (RES) are also shown as predicted by NUANCE [38]. Data available up until 2012 is overlaid. Figure taken from [39].

nucleon, or even the entire nucleus. Moreover, any component of the nucleus will also be bound in nuclear potential and have non-zero momentum which needs to be accounted for. For these reasons, good nuclear models are needed to describe the behaviour of nucleons inside a nuclear potential.

2.3.1 Nuclear Models

The simplest nuclear model is the Fermi Gas (FG) model [40] which assumes that the nucleons are bound in some average nuclear potential and are only co-dependent on each other through the Pauli exclusion principle. Illustrated in figure 2.5 the FG picture models the nuclear potential as a rectangular well which is shallower for protons due to their electromagnetic repulsion. Within the potential, nucleons occupy discrete energy states up to their respective Fermi energies. In reality this picture is flawed and can only theoretically exist in temperatures of absolute zero. Advancements upon the FG model exist and are being tested by current experiments: Examples of these include the Relativistic Fermi Gas (RFG) [41] model and the

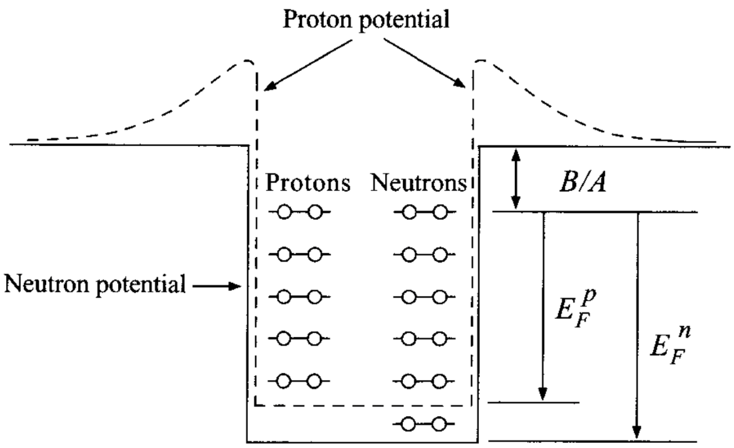

Figure 2.5: The nuclear potential energies for protons and neutrons according to the Fermi Gas Model. The Fermi energies E_F^p and E_F^n are shown for protons and neutrinos respectively, as well as the binding energy B/A.

Spectral Function (SF) model [42]. The RFG model extends the FG model to include relativistic kinematics, whereas the SF model takes a new approach by including nuclear shell structure models to determine nuclear momentum probability densities [43].

2.3.2 Neutrino Interactions in Nuclei

The primary interaction is the first action along a chain of events that have to be accounted for when considering neutrino-nucleus interactions and cross-section measurements. There are multiple ways in which a neutrino can interact with a nucleus. This thesis will provide an account of the four main process in which neutrinos can primarily interact. These are charged current quasi elastic, which is the predominant interaction limiting the T2K oscillation analysis; deep inelastic scattering, resonance and coherent interactions which are the dominant sources within the cross section analysis described in this thesis.

Charged Current Quasi-Elastic

Charged Current Quasi-Elastic (CCQE) and Neutral Current Elastic (NCE) scatterings occur when the neutrino scatters off an entire nucleon, usually liberating it from the nucleus. For NCE the leptonic component of the interaction remains the same through a Z^0 boson exchange. Whereas for CCQE the exchange of a $W^{\pm}$ boson causes the incoming neutrino to change into its counterpart lepton particle with identical flavour. These are represented by the following interaction modes:

$$\nu + N \rightarrow \nu + N \tag{2.23}$$

$$\nu_l + n \rightarrow l^- + p \tag{2.24}$$

$$\bar{\nu} + p \rightarrow l^+ + n \tag{2.25}$$

Elastic and quasi-elastic scattering interactions are of particular importance to the T2K neutrino oscillation analyses as CCQE scatterings dominate the area of kinematic space below ~1.5 GeV, which corresponds to the neutrino energy region used to exploit the first oscillation maxima. Calculating the cross-sections of such processes analytically can be very challenging. Nevertheless, parametrising the cross-section is possible through the Llewellyn Smith model [44]. The parameters can then be measured through electron scattering and β-decay measurements.

Resonance

The largest contributing mechanism for pion production in neutrino interactions, excluding DIS, is that of Resonance production (RES). This is particularly important for the cross-section analysis described in chapter 4 which involves π^+ production in the final state. In resonance interactions the incoming neutrino excites the nucleon to a baryonic resonance. The resonance state then decays back to the ground state, liberating a new final state particle. The most typical resonance state occurs when the neutrino-nucleus interaction centre of mass energy is greater than the mass of a Δ (1232) baryon, which then decays to produce a single pion. For this process the charged current interaction channels are:

$$\nu_l + p \rightarrow l^- + p + \pi^+ \tag{2.26}$$

$$\nu_l + n \rightarrow l^- + n + \pi^+ \tag{2.27}$$

$$\nu_l + n \rightarrow l^- + p + \pi^0 \tag{2.28}$$

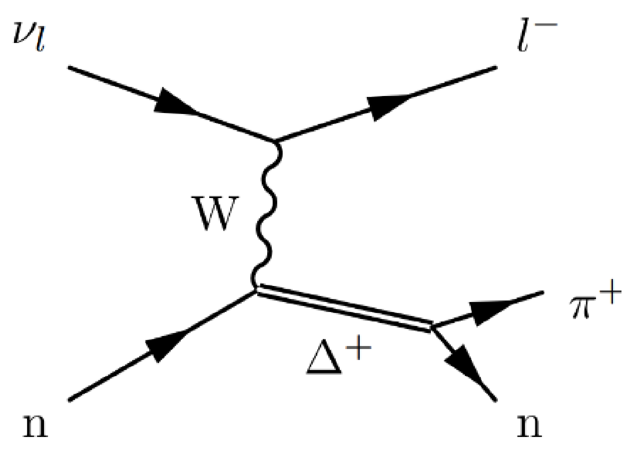

Figure 2.6: An example of a resonance interaction resulting in π^+ production. Figure taken from [45].

Neutral current resonance processes are also possible but do not lead to the formation of a charged lepton in the final state. Instead the neutral current resonance production of single pions is described by four processes:

$$\nu_l + p \rightarrow \nu_l + p + \pi^0 \tag{2.29}$$

$$\nu_l + p \rightarrow \nu_l + n + \pi^+ \tag{2.30}$$

$$\nu_l + n \rightarrow \nu_l + p + \pi^- \tag{2.31}$$

$$\nu_l + n \rightarrow \nu_l + n + \pi^0 \tag{2.32}$$

Whilst single pion production is most common, higher resonances also have the ability to produce kaons, photons, other mesons, as well as multiple pions. A representation of process 2.27 is also shown as a Feynman diagram in figure 2.6

As shown in figure 2.4, resonance production is an important interaction mode for neutrinos of energies between 1.5 GeV and 5 GeV. Neutrino interaction simulations typically describe resonance production through the Rein-Seghal model [46].

Deep Inelastic Scattering

As neutrino energies get higher the neutrino begins to be able to resolve the internal structure of the nucleon. Interactions with individual quarks via W or Z boson exchanges can break apart the nucleon and produce a jet of hadrons. This process is knows as Deep Inelastic Scattering (DIS) and becomes the dominant neutrino-nucleus interaction mode above approximately 5-10 GeV (see figure 2.4). DIS is also a significant process for pion production and is thus an important factor in the analysis described in chapter 4.

Deep Inelastic Scatterings are well understood for high energy neutrinos given the historical nature of using DIS as a means to validate the standard model and probe nuclear structure [47–49]. However, there is less understanding of how RES merges into DIS at the lower energies more relevant to long baseline neutrino experiments. It is also relatively unclear the accuracy with which current DIS models can be extrapolated to these lower energies.

Coherent Scattering

Another method in which pions can be produced is via both neutral and charge current Coherent scattering (COH). In coherent pion production the neutrino scatters off the whole nucleus, producing a single pion at a small angle relative to the incident neutrino:

$$\nu_l + A \rightarrow \nu_l + A + \pi^0 \tag{2.33}$$

$$\nu_l + A \rightarrow l^- + A + \pi^+ \tag{2.34}$$

The recoiling nucleus does not fragment and remains in the ground state. This interaction is only possible at low Q^2, therefore at neutrino energies relevant to long baseline neutrino experiments COH scatterings have very small interaction cross-sections. Coherent interaction simulations are most often modelled with the Rein-Seghal coherent model [46].

2.3.3 Final State Interactions

After the primary interactions have occurred the end products then need to propagate through the nucleus before they escape into the detector and measurements can be made. During this time the hadrons have the possibility to re-interact inside the nuclear medium. These interactions are known as the Final State Interactions (FSI). At neutrino energies most relevant to long baseline neutrino experiments, the π mesons are the most common form of hadrons produced in primary interactions. Taking the π^+ meson example, the most frequent forms of FSI are elastic scattering (equation 2.35), pion absorption (equation 2.36), and charge exchange reactions (equation 2.37):

$$\pi^+ + N \to \pi^+ + N \tag{2.35}$$

$$\pi^+ + N \to N' \tag{2.36}$$

$$\pi^+ + n \leftrightarrow \pi^0 + p \tag{2.37}$$

Consequently, the original pion can not only be absorbed, but can also have its kinematics altered or even stimulate the emission of more hadrons inside the nuclear medium.

Modelling FSI is extremely complex, and imposing constraints on FSI with experimental data is also very difficult. Nevertheless attempts to model FSI through cascades has been attempted in neutrino interaction simulations [38]. In such models, each hadron leaving the interaction vertex is treated independently and a number of discrete steps are defined on route to the hadrons potential escape. The size of each step is based on the particles mean free path. At every step each FSI mode has the potential to occur based on a calculated probability. This process continues until the hadron either leaves the nucleus or is absorbed. Further details of how neutrino interaction simulations treat FSI can be found at [50, 51].

Chapter 3

The T2K Experiment

Situated on two sites on opposite sides of Japan, Tokai-to-Kamioka (T2K) [52] is a long-baseline neutrino oscillation experiment to measure parameters of the PMNS matrix that govern neutrino oscillations. On the east coast of Japan in Tokai-mura, the Japan Proton Accelerator Research Complex (J-PARC) [53, 54] provides a high purity ν_μ beam using a 30 GeV proton synchrotron. J-PARC also hosts a number of near detector facilities aimed at observing beam flux and quality before oscillations and characterising neutrino interaction processes useful for oscillation analyses. 295 km west of J-PARC lies the far detector Super-Kamiokande (SK). Stationed under Mount Ikenoyama in the Mozumi mine, Super-Kamiokande is a water Cherenkov detector measuring the status of the neutrino beam post oscillations. Figure 3.1 gives a schematic overview of T2K.

Characterising parameters of the PMNS matrix in T2K is achieved by studying both ν_μ disappearance and ν_e appearance probabilities in the far detector respectively.

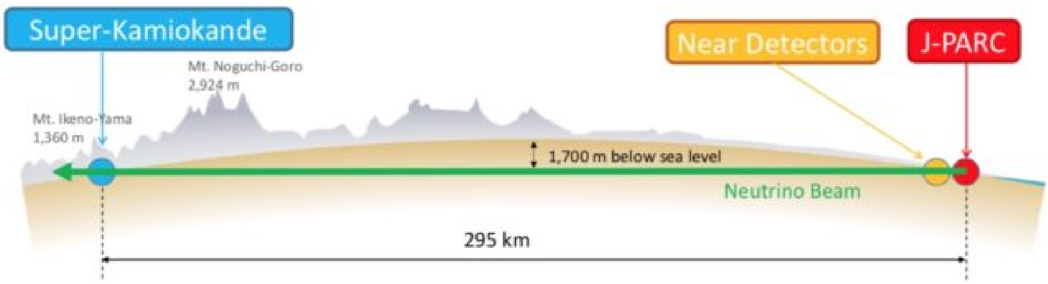

Figure 3.1: An overview of the T2K experiment.

In 2014 T2K became the first experiment to successfully measure the $\nu_\mu \rightarrow \nu_e$ appearance channel [55]. A total of 28 events were observed at a significance of 7.3σ. The latest oscillation analysis publication from T2K [56] gives up-to-date measurements on the oscillation parameters. T2K finds $\sin^2(\theta_{23}) = 0.53^{+0.03}_{-0.04}$ for both neutrino mass orderings. T2K also found, assuming the normal (inverted) mass orderings, $\Delta m^2_{32} = (2.45 \pm 0.07) \times 10^{-3}$ ($\Delta m^2_{13} = (2.43 \pm 0.07) \times 10^{-3}$) eV^2/c^4 respectively. The best fit values for δ_{CP} and statistically dominated 1σ (68%) uncertainties, assuming normal (inverted) mass orderings, are $-1.89^{+0.70}_{-0.58}$ ($-1.38^{+0.48}_{-0.54}$). The T2K results show a preference for values of δ_{CP} that are near maximal CP Violation. Furthermore CP conserving points, $\delta_{CP} = 0$ and $\delta_{CP} = \pi$, are ruled out at a 95% confidence level.

Whilst not strictly one of T2K's primary goals, the near detector complex has provided T2K a means of making neutrino cross-section measurements. These measurements are extremely important in understanding the intricate nature of neutrino-nucleus interactions, and thus are pivotal in constraining systematic uncertainties [57]. A number of cross-section measurements have been published. Muon neutrino cross-sections have been studied over a number of target materials and final states. Published in 2013, the flux-averaged total charged current inclusive ν_μ cross-section was measured to be $\langle \sigma_{CC} \rangle = (6.91 \pm 0.13(stat) \pm 0.84(syst)) \times 10^{-39}$ cm^2 per nucleon for a mean neutrino energy of 0.85 GeV [58]. The ν_e charged current inclusive cross-section has also been published and is outlined in section 4.2.

3.1 Beam

3.1.1 Proton Beam

T2K's beam is provided by J-PARC's 30 GeV main ring synchrotron. A H^- beam is linearly accelerated to 400 MeV, before being converted to H^+ at the entry point to the next acceleration phase - a rapid cycling synchrotron (RCS) injection point. The protons are accelerated to 3 GeV before supplying approximately 5% to the main ring, where they are further accelerated up to 30 GeV. Each spill, consisting of eight bunches, has a spill width of 5 μs and cycles at 0.5 Hz. Fast extraction mode is used

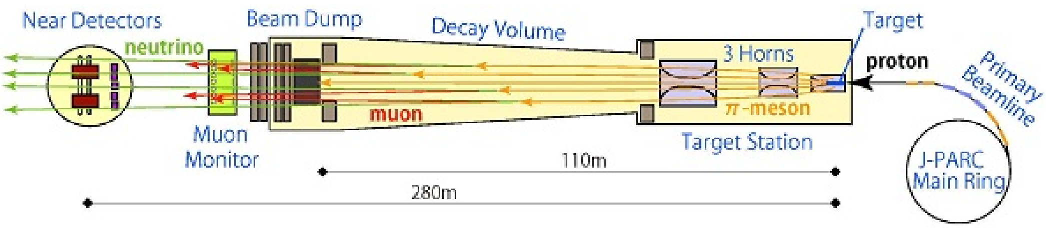

Figure 3.2: A schematic representation of the primary and secondary neutrino beamlines at J-PARC, used for the T2K muon neutrino beam. Reproduced from the J-PARC public website.

for the neutrino beam-line, whereby all eight proton bunches are extracted within a single turn.

3.1.2 T2K Neutrino Beamline

The T2K neutrino beamline [59] consists primarily of two separate segments shown in figure 3.2. The primary beamline takes the protons from the MR, steers them ultimately towards the far detector and collides the protons with a graphite target. The 2.6 cm diameter 1.8 g/cm^3 target core has a thickness of 91.4 cm, corresponding to 1.9 interaction lengths. The core is surrounded by a 2 mm thick graphite tube which together are sealed inside 0.3 mm titanium case. Cooling from the pulsed beam heat load is provided by helium gas flowing through the gaps between the core and tube, as well as between the tube and case. Upstream of the target an Optical Transmission Radiation monitor (OTR) is used to monitor the proton beam profile. The OTR uses titanium-alloy foils placed 45° incident to the beam to produce visible light in the form of transition radiation. The light is then directed, through iron and concrete shielding, via four aluminium 90○ off-axis parabolic mirrors to a charge injection device camera, producing an imagine of the proton beam profile.

The secondary beamline collects mesons from the primary beamline, provides a decay volume and finishes with a beam dump at the far end. Downstream from the secondary beam-line are three magnetic horns. Running the magnets in forward horn current mode (FHC) and reverse horn current mode (RHC) will yield beams dominated by ν_μ and $\bar{\nu}_\mu$ respectively. The reason for this is the magnetic horns are there to focus mesons with the correct charge for the (anti)neutrino production

T2K Run Number	Start Date	End Date	FHC POT (x10^{19})	RHC POT (x10^{19})
Run 1	23 Jan. 2010	26 Jun. 2010	3.288	-
Run 2	18 Nov. 2010	11 Mar. 2011	11.341	-
Run 3	08 Mar. 2012	09 Jun. 2012	16.081	-
Run 4	19 Oct. 2012	08 May. 2013	36.363	-
Run 5	21 May. 2014	24 Jun. 2014	2.465	5.145
Run 6	02 Nov. 2014	01 Jun. 2015	2.149	35.766
Run 7	01 Feb. 2016	27 May. 2016	4.890	35.272
Run 8	27 Oct. 2016	12 Apr. 2017	72.557	-

Table 3.1: T2K data information from runs 1-8 with the recorded POT in both FHC and RHC modes. Information gathered from [61].

of interest and deflect those that do not. All focussed mesons now pass through a decay volume approximately 96 m long. Any particles that do not decay under this volume will hit the beam dump removing any remaining hadrons. It is probably that muons with momenta above 5 GeV/c can pass through the beam dump; these can be measured using muon monitors, such as MUMON. Using an ionisation chamber and a Si pin photodiode, the MUMON monitors can infer the beam intensity to better than 3% and the beam direction to within 0.25 mrad [60].

The beam intensity is measured by five Current Transformers (CTs) which consist of a 50-turn toroidal coil around a ferromagnetic coil. As the protons pass through a current is induced in the coils which can be used to infer the proton flux. The fifth current transformer CT5 is stationed furthest downstream in the primary beam-line, it can therefore be used to count the number of incident protons on the graphite target. Table 3.1 reports the T2K protons-on-target (POT) figures separated by run number; a metric used for data collecting.

3.2 Off-Axis Measurement

This thesis will focus primarily on work performed in FHC mode. There are multiple decay methods in which the neutrinos can be produced in FHC mode. There are three primary meson decays from π^+, K^+ and K^0_L; as well as one meson decay from μ^+. Figure 3.3 demonstrates the predicted flux of neutrinos from the beam in

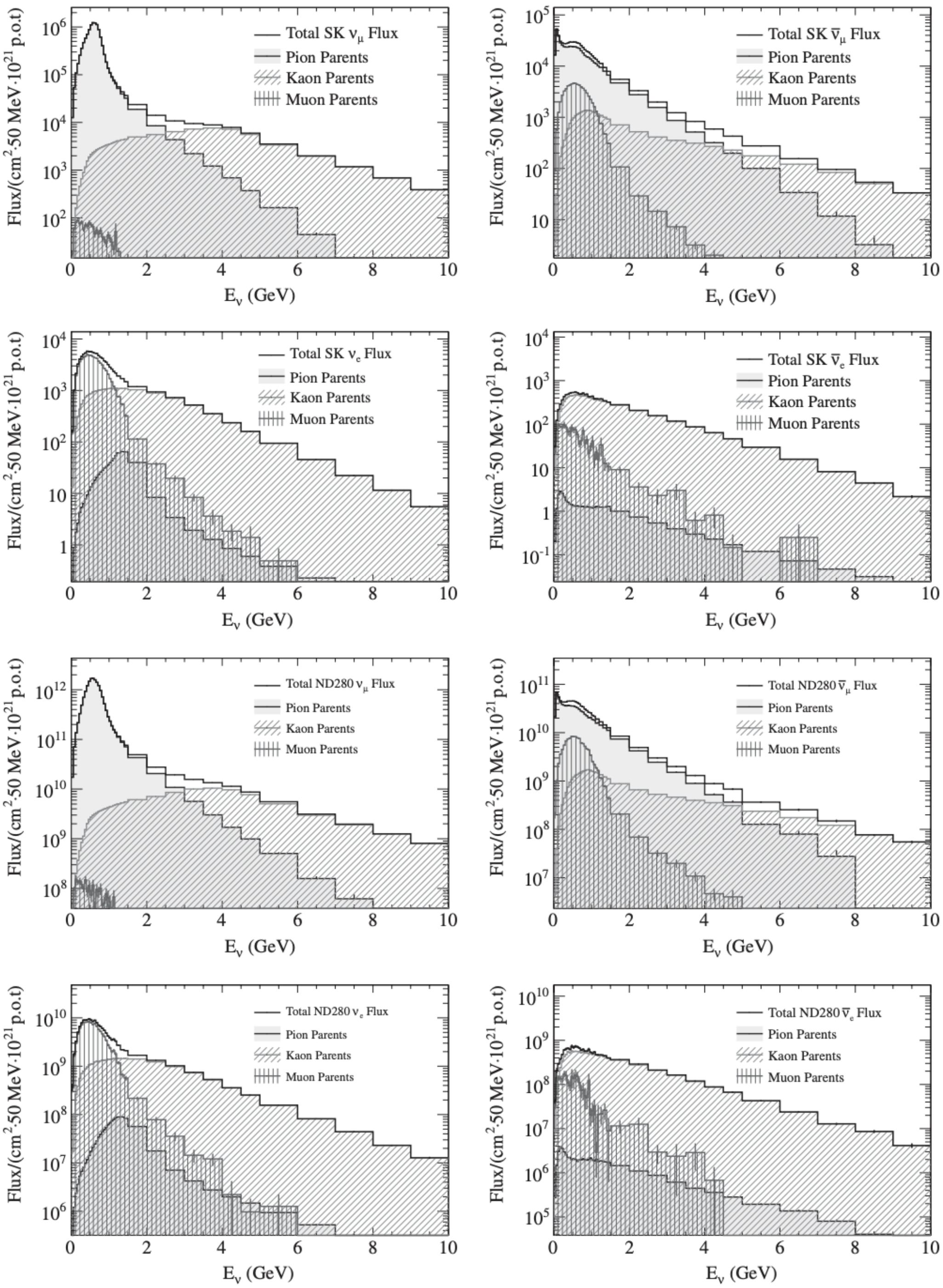

Figure 3.3: The neutrino flux prediction at ND280 and Super-Kamiokande for both ν_μ and ν_e as well as their respective antiparticles. Note due to a large MC statistical error, the error bars in most energy bins are too small to be seen. Figure taken from [59].

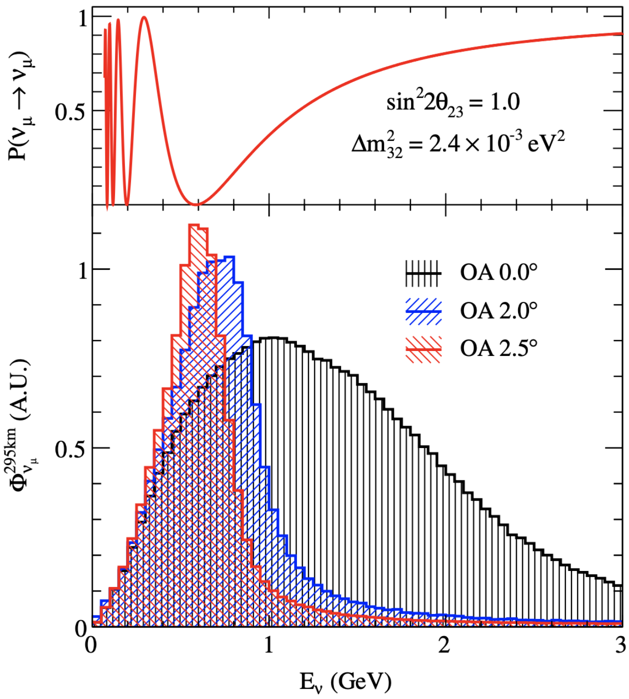

Figure 3.4: The muon neutrino oscillation probability (above) alongside the arbitrarily normalised neutrino flux (below) as a function of neutrino energy over a range of off-axis angles. This figure is used to justify a peak neutrino beam energy of 0.6 GeV and an off-axis angle of 2.5°. Taken from [59].

reference to the parent particle. It can be seen in this figure that the dominant parent of both ν_μ and $\bar{\nu}_\mu$ are π, with a contributions from K above 3 GeV. Pion kinematics are also integral to the energy spectrum shape of the neutrinos. Figure 3.4 shows that by moving off-axis the energy spectrum both narrows and shifts favouring lower energies. T2K was the first experiment to exploit this phenomena with the "off-axis technique", in which the far and near detector complexes are offset from the neutrino beam centre [62]. The positive effects of this are two-fold: (1) it focusses and reduces the neutrino peak energy so that it aligns with the first oscillation maximum for ν_μ disappearance channel, and (2) it reduces backgrounds present in the high energy tail, improving sensitivity to both ν_e and ν_μ appearance and disappearance channels respectively.

3.3 Near Detector Complex

The near detector complex is located 280m downstream of the beam target, it supplies a home for two main near detectors. Located on axis is the Interactive Neutrino GRID (INGRID) and off-axis in line with the far detector is Near Detector at 280m (ND280). The near detector complex equips T2K with beam quality assurance and control, as well as constraints on processes valuable to oscillation analyses. Both detectors are situated 37 metres below ground level in an open air pit lined with concrete surrounded by sand.

3.3.1 INGRID

Using an off-axis technique, it is critical for T2K to understand the neutrino beam properties to a precision of a few percent. The Interactive Neutrino GRID (INGRID) detector [63] is used to measure neutrino flux and beam direction on a spill-by-spill basis to discount any beam discontinuities. INGRID is located in the near detector complex 280 m downstream of the beam target and is centrally aligned to the beam centre axis. The detector is constructed out of 14 identical modules orientated in a cross-shape, as seen in figure 3.5. Each INGRID module consists of a "sandwich" of 9 iron plates and 11 scintillator layers, surrounded by veto planes on each side to reject cosmic backgrounds. The modules are arranged such that 7 exist both horizontally and vertically, and 2 are located at the off-diagonal. At 280 m downstream from the beam target the neutrino beam width (1σ) is about 5 m, therefore INGRID was designed to sample the beam in a transverse section of 10 m x 10 m. INGRID has the capability of measuring beam directionality to 0.2 mrad - resolving the neutrino beam centre to 5 cm. In context it has been estimated that an offset of 1 mrad yields an uncertainty of approximately 2-3% on the neutrino energy scale [52]. INGRID can also measure the event rate with an uncertainty of less than 2%. Additionally, an extra module called the Proton Module is used to detect the muons and protons produced by the neutrino beam in INGRID. The module consists of scintillator planes without any iron plates. The goal of this module is constrain the quasi-elastic channel for comparisons of beamline and neutrino interaction simulations. More

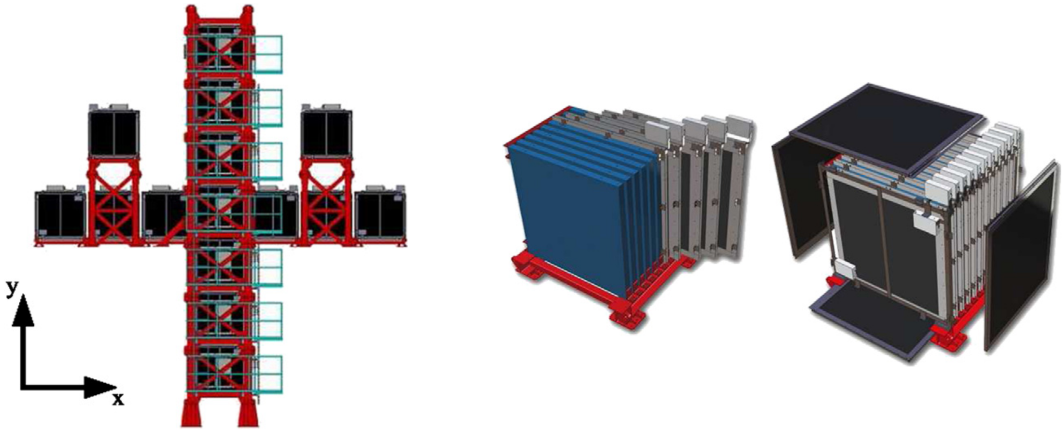

(a) (b)

Figure 3.5: Schematic representations of both the INGRID detector (a) and the modules used inside (b). In (b) the left module (blue) shows the tracking planes, the right module (black) shows the veto planes. Taken from [52].

recently for a sample of T2K runs, an INGRID water module has been added giving the capabilities of measuring neutrino interactions on water [64].

3.3.2 ND280

The near detector complex also houses an off-axis detector called Near Detector at 280m (ND280). Being off-axis, the role of ND280 is to provide a measurement of the near neutrino flux to compare with the far neutrino flux observed in Super-Kamiokande. Primary goals of ND280 were to provide measurements of ν_μ and ν_e interactions for neutrino oscillation studies with the far detector. Nevertheless, due to ND280's ability to accurately track and reconstruct particles from primary scattering in the vertex. An important extra contribution of ND280 is to measure and study neutrino interaction cross-sections.

Figure 3.6 gives a schematic diagram of the components inside of ND280. The ND280 detector consists of 3 time projection chambers (TPCs) and 2 fine grained detectors (FGDs) arranged in an alternating pattern. This region is often referred to as the "tracker". Upstream of the tracker region a π^0 detector (P0D) is located. Surrounding the inner subdetectors are lead scintillator sampling electromagnetic calorimeter modules (ECals). The next layer of ND280 is a UA1 magnetic yoke which

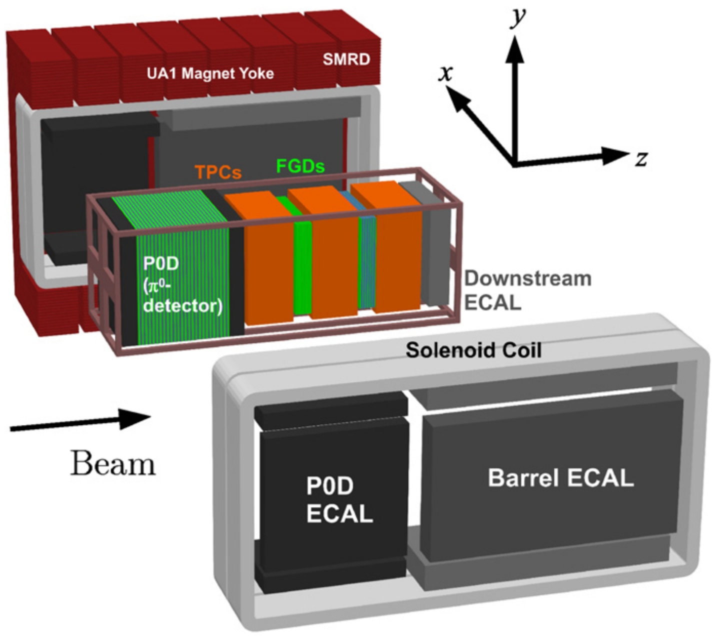

Figure 3.6: An exploded view of the ND280 detector. Taken from [59].

provides a 0.2 T magnetic field for accurate sign selection in the TPCs. A Side-Muon Range Detector (SMRD) made from plastic scintillator strips is interleaved within the magnetic yoke. The SMRD contributes high angle muon tracking and also acts as ND280's cosmic trigger.

Pi-zero Detector

The most upstream component of ND280's inner sub detectors is the π^0-Detector (P0D) [65]. Surrounded by ECALs the P0D consists of 40 modules containing scintillator bars for tracking interleaved with lead/brass sheets. Within each module are 134 vertical bars (2200 mm long) and 126 horizontal bars (2340 mm long), arranged in perpendicular arrays. Furthermore, the P0D includes pouches that can be filled with water, giving options to run in water or air mode. The two different interaction target modes were designed to allow the P0D to measure neutrino interaction cross-sections on water through subtraction. Given the prominent π^0 background in the ν_e appearance channel at Super-Kamiokande, the P0D was

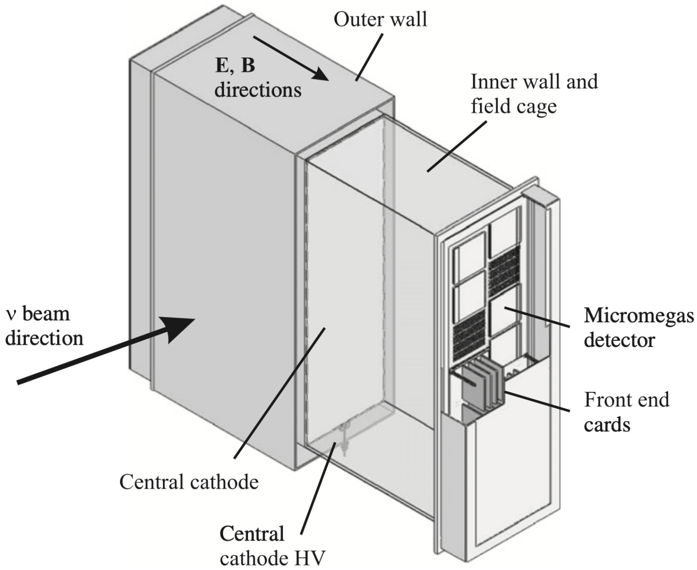

Figure 3.7: A diagram demonstrating the main aspects of the time projection chambers in ND280. Taken from [59].

primarily designed to measure the neutral current process:

$$\nu_\mu + N \to +\pi^0 + X \tag{3.1}$$

on a water target [65]. The P0D has also been used to constrain the ν_e contribution to the beam flux [66], a key intrinsic background for the oscillation analysis. Moreover, a number of cross-section analyses using the P0D as a water target are still ongoing.

Time Projection Chambers

Moving upstream the next sub detector is the first of three gaseous Time Projection Chambers (TPC) [67]. The TPCs are situated in an alternating sequence with the FGDs, as shown in figure 3.6. Each TPC specialises in the high-resolution tracking of charged particles. Such tracking is important to provide measurements of particles momentum and identification of particle type. The three TPCs are labelled numerically in ascending order from 1 for the most upstream TPC, and 3 for the most downstream. Each of these TPCs consists of two gas-tight boxes, one nested inside of the other. A schematic of the TPCs is shown in figure 3.7. The inner box contains an argon-based gas doped with small quantities of CF_4 ($\sim$3%) and iC_4H_{10} ($\sim$2%). To assemble a drift field in the same orientation as the ND280 magnetic field, a central cathode plane dissects the inner box into two separate halves. At either end wall, readout planes consisting of 12 micromegas modules [68] are placed parallel to the cathode plane. Conducting strips connected by precision resistors are used in the side walls to create a voltage divider and thus produce a uniform electric field in the desired drift direction. The outer box, filled with CO_2, adds gas contamination protection from the atmosphere, as well as providing electrical insulation between the inner box and ground.

As charged particles propagate through the TPCs they ionise the gas. The resulting electrons then drift, away from the central cathode, towards the readout planes. These electrons drift under an electric field of around 280 V/cm, over a maximum distance of approximately 90 cm. Each micromegas module in the readout plane consists of a two stage parallel plate avalanche chamber separated by an amplification region, combined with a conversion-drift space [69]. The advantage of such a design allows for the fast removal of positive ion signal produced during avalanche, yielding the potential for sub nanosecond precision signals. Each micromegas modules' objective is to record the charge and arrival time of the drifting particles. These are combined over the 12 modules in each plane to produce 3D reconstructed paths of traversing particles through the TPC.

The TPC makes up part of the ND280 tracker region, which is designed to study charged current neutrino interactions. The tracking performance requirements, based at 700 MeV, are to measure the transverse momentum of charged particles with a resolution of 0.1 p_T or less, whereby the transverse momentum is perpendicular to the magnetic field direction. Furthermore to measure ν_e interaction signal, the resolution in ionisation energy loss needs to be at least 10%. This is because the ionisation loss of electrons in 1 atm of argon gas is approximately 45% more relative to muons around the regions of interest in momentum space [67]. To achieve such goals the TPC operates in a magnetic field of 0.2 T with a sampling length of 700 mm, and pad segmentation of 70 mm^2.

Particle identification (PID) is also a key goal of the TPCs. Distinguishing

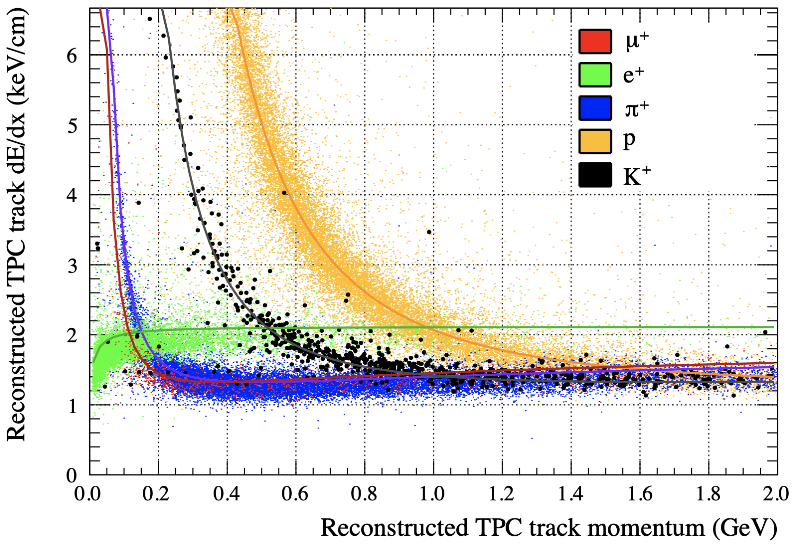

Figure 3.8: The reconstructed energy loss (dE/dx) as a function of reconstructed track momentum in the TPC. The curves show the expected distributions from calibration studies, the scatter points are reconstructed distributions from neutrino interaction simulations in ND280. Taken from [70].

between different particle types is achieved by measuring the energy loss (dE/dx) as a function of momentum. The amount of ionisation gives estimates on the energy loss and is characterised by the particles velocity, whilst the curvature of a track yields the particle's momentum which largely depends on both velocity and mass. These two quantities together can be used to identify particle types - which can be seen clearly in figure 3.8.

Fine Grained Detectors

Interlaced among the TPC modules reside two Fine Grained Detectors (FGDs) [71], labelled FGD1 and FGD2 for the most upstream and downstream detectors respectively. A single functioning unit of each FGD is an extruded polystyrene scintillator bar oriented perpendicular to the beam axis. Each scintillator bar has dimensions of 9.6 mm x 9.6 mm x 1864.3 mm, and together they are arranged into "XY modules". With 192 bars in both the horizontal and vertical direction, each module is able to achieve the fine granularity and high spatial resolution the name suggests. FGD1 is comprised of 15 modules, whilst FGD2 has seven; giving them a

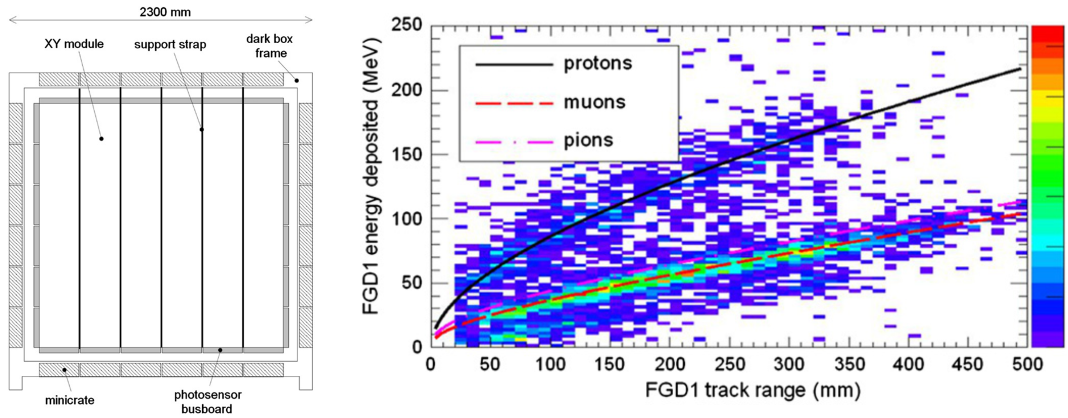

(a) (b)

Figure 3.9: (a) A cross section schematic representation of FGD1. (b) The energy deposited in FGD1 as a function of the track range. The scatter-plot is created with stopping particles in neutrino beam data, the curves show the expectation for pions, muons, and protons from MC. Both images sourced from [71].

total of 5760 and 2688 scintillator bars respectively. In addition to the bars, FGD2 includes 6 water target modules providing a layer of water as an interaction target. By comparing interaction rates in both FGD1 and FGD2 it is possible to discriminate cross-sections between carbon and water targets. A diagram representing the first FGD module can be seen in figure 3.9a. Each FGD has a total heigh tof 2300 mm, a width of 2400 mm, and depth 365 mm, corresponding to the beam direction. FGD1 has a fiducial mass of 919.5 kg, which translates to $(5.54 \pm 0.04)\times10^{29}$ target nucleons.

Interactions in the FGD are measured via the production of scintillation light from propagating charged particles through the scintillator bars. Light is then channelled down a wavelength shifting fibre to a 667 pixel multi-pixel photon counter (MPPC) [72–74]. The MPPC determines both the charged particle's time of arrival, and energy deposited through the light intensity measured in number of photoelectrons recorded.

The primary objective of the FGDs is to provide neutrinos with potential interaction targets[1], whilst also maintaining a degree of tracking ability required by T2K for neutrino interaction rates on water. Furthermore, the FGD can also assist

[1]The tracker must contain approximately 1 tonne of target mass to yield a sufficient statistical sample of events

the TPC in PID through measuring total energy deposited and track length. The main objective is to differentiate protons from pions and muons. The distributions for protons is distinct from the latter and is demonstrated in figure 3.9b.

Electromagnetic Calorimeters

The Electromagnetic Calorimeters (ECal) [75] are lead-scintillator sampling calorimeters organised into three regions that surround ND280: the Barrell-ECal (BrECal) enclosing the tracking region, and the P0D-ECal surrounding the P0D; both consist of six separate modules (2 top, 2 bottom, 2 side)[2]. Additionally, the DownStream-ECal (DS-ECal) is made up of a single module and is located furthest downstream after the final TPC. This equates to a total of 13 ECal modules. For the purpose of this thesis the DS-ECal and BrECal will be referred to collectively as the tracker-ECal, a terminology used commonly given the similar physics motivations of each region.

Each module is made up of multiple layers of scintillating polystyrene bars bonded to lead sheets. The polystyrene bars have a cross section of 40 mm x 10 mm in all modules, whereas the lead sheets have a thickness of 1.75 mm and 4.00 mm in the tracker-ECal and P0D-ECal respectively. The size of such components is constrained by the ECals position between the inner ND280 detectors and the magnet, as demonstrated by figure 3.6.

The goal of all ECal modules is to provide a measurement of the energy of particles escaping the inner tracker. Nevertheless, physics aims for the tracker-ECal and P0D-Ecal modules differ from each other. The tracker-ECal is designed as a tracking calorimeter providing detailed reconstruction of electromagnetic showers to complement the charged-particle identification and tracking capabilities of the TPCs [75]. An advantage of this is the ability to measure the energy of neutral particles and assist with particle identification in the ND280 tracker. There are 31 scintillator-lead layers in the BrECal and 34 layers in the DS-ECal. This equates to 10 and 11 radiation lengths, X_0, a quantity that was determined to best contain electromagnetic showers of photons, electrons and positrons of energies up to 3 GeV. At least 10 X_0

[2]The BrECal and P0D-ECal are attached to the magnet and thus must have two top and bottom modules to allow the magnet to be opened

are needed to ensure more than 50% of the energy resulting from photon showers initiated by a π^0 decay is contained within the ECal. 3D reconstruction of tracks and showers is also achieved through rotating alternate layers by 90 degrees. The energy resolution for tracker-ECal modules is approximately $10\%/\sqrt{E}$ [76].

The role of the P0D-ECal is to tag escaping energy from the P0D and distinguish between photons and muons. In contrast to the tracker-ECal, shower reconstruction is not needed in the P0D-ECal as it is already performed by the P0D itself. Therefore, the P0D-ECal has only six scintillator layers (approximately 4.3 X_0 for reference), but requires thicker lead sheets to promote the higher detection efficiency of photons, the containment of showers, and that photon showers can be recognised from muons.

The UA1/NOMAD Magnet

The magnet installed at ND280 is built around the UA1/NOMAD magnet previously commissioned at CERN [77, 78]. The magnet provides a horizontally orientated dipole magnetic field of 0.2 T. The dipole magnetic field is created by water-cooled aluminium coils. Additionally the magnet also consists of a flux return yoke, split into 2 sections each made of eight C-shaped yokes providing magnetic insulation for the surrounding detector. The external dimensions of the magnet are 7.6 m x 5.6 m x 6.1 m. Nevertheless, it is the internal dimensions at 7.0 m x 3.5 m x 3.6 m that yeild the main spatial limitations on ND280s subdetector modules [52].

The ND280 magnet has a key role in particle identification through measurements of momenta and determination of the signs of charged particles, produced by neutrino interactions within the TPCs.

Side Muon Range Detectors

The Side Muon Range Detector (SMRD) [79] is situated inside the magnetic return yoke described previously. Shown in figure 3.10 the SMRD is placed in the inner-most gaps and surrounds the entire ND280 ECal, P0D and tracker sections. The SMRD consists of 2008 scintillator bars of dimensions 7 mm x 167 mm x 875 mm arranged in 192 horizontal and 248 vertical modules. The purpose of the SMRD is to identify

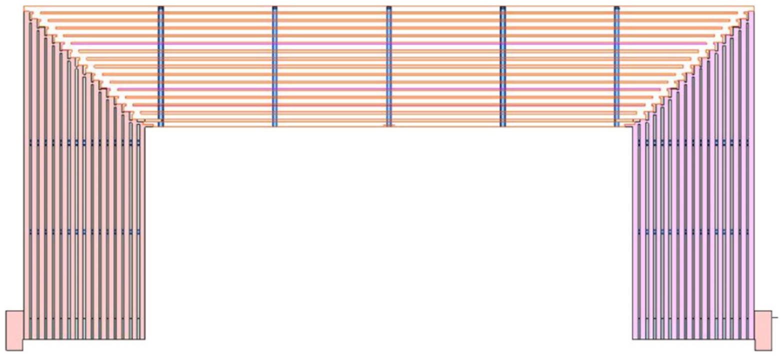

Figure 3.10: An engineers drawing of a single yoke in the UA1 magnet showing the interleaved SMRD. Adapted from [79].

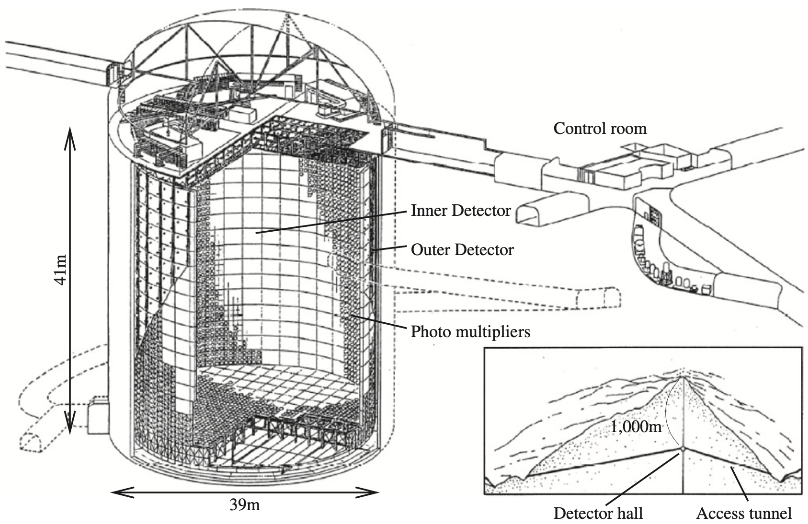

Figure 3.11: A diagram of the Super-Kamiokande detector. Taken from [81].

high angle muons that escape from the inner detector leaving behind little or no TPC hits. Furthermore, the SMRD acts as both a trigger and a veto for cosmic muons.

3.4 Far Detector

Located 285 km away from J-PARC inside the Kamioka mine, Super-Kamiokande (SK) acts as the far detector for the T2K experiment [80]. The mine is located 1000 m deep under mount Ikenoyama. This is the equivalent of 2700 m.w.e (metre equivalent water) and thus acts as a natural shield to cosmic rays.

A diagram of Super-Kamiokande is shown in figure 3.11. The 41.4 m x 39.3 m tank has a cylindrical geometry orientated in the vertical direction. The vessel is made from stainless steel and the detector is split into two coaxial cylinders called the inner (ID) and outer (OD) detectors, with inner dimensions of 36.2 m x 33.8 m. The ID and OD are separated by a black Tyvek sheeting. Tyvek is used for it's high reflectivity, reaching a maximum value of 98.5% at wavelengths of approximately 400 nm [82]. The tank is filled with ultra-pure water providing a 22.5 kton fiducial volume. The ID is surrounded by 11,129 20-inch Hamamatsu R3600 hemispherical photomultiplier tubes (PMTs) directed inwards of the detector, providing approximately 40% photo-coverage. Moreover, the OD has 1,885 8-inch Hamamatsu R1408 PMTs facing outwards - the objective here to provide a veto for the inner detector. Each PMT has single photon detection capabilities and has a combined quantum and collection efficiency of 20%. The working wavelength range of each PMT is 350 nm - 500 nm, with a maximal quantum efficiency reached at approximately 400 nm.

The primary method for particle detection in SK is through the production of Cherenkov light from charged particles after neutrino interactions. If a charged particle moves faster than the speed of light with respect to the medium it's propagating through, a respective cone of Cherenkov light will be emitted around its direction of travel. The subsequent ring from this cone seen at any one time has signature properties that can be used for particle identification. The "fuzziness" of the ring, a by-product from the degree of scattering, can be used to differentiate between muons and electrons. Heavier particles, such as muons and pions, will generally without scattering in the medium, whereas electrons being lighter particles will scatter more frequently and produce EM showers when travelling. The contrast of the two will produce clear rings and fuzzier rings for muons and electrons respectively.

SK is also capable of detecting delayed signals from Michel electrons as well as detecting charged current interactions with one charged pion in the final state. Furthermore tracks with kinked trajectories are used to discern scattered pions from muons.

In the summer of 2018, SK was drained for scheduled maintained. Furthermore, gadolinium doping in the water was introduced which will add the capability of neutron tagging [83, 84]. Data taking has since resumed in autumn 2019.

Chapter 4

Measurement of ν_e CC π^+ with the ND280 Tracker

4.1 Motivation

For long baseline neutrino oscillation experiments such as T2K and NOVA, as well as the future generation experiments Hyper-Kamiokande and DUNE, ν_e charged current π^+ production provides a significant contribution to the ν_e appearance channel. Despite this, there is currently no measurement of exclusive ν_e charged current π^+ production on a Carbon target in the literature to date.

For appearance studies at T2K, the far detector uses two electron neutrino appearance samples in FHC mode: 1-ring ν_e CCQE, and a 1-ring ν_e CC $1\pi^+$ sample. An effort to produce a 2-ring ν_e CC $1\pi^+$, where both e-like and π^+-like rings sample are reconstructed, is also in development for the oscillation analysis, but is not yet implemented. The T2K far detector data collected to date displays an excess of events over the background prediction in the FHC 1 decay electron sample [85]. It can be seen in figure 4.1 that the expected number of events, assuming maximal CP-violation, is 7; whereas 15 events are observed in data. The probability of observing an excess at least this large in one of T2K's five samples is 6.9% for the best fit value of the oscillation parameters [56]. Currently, T2K has no direct constraint on this process from the near detector.

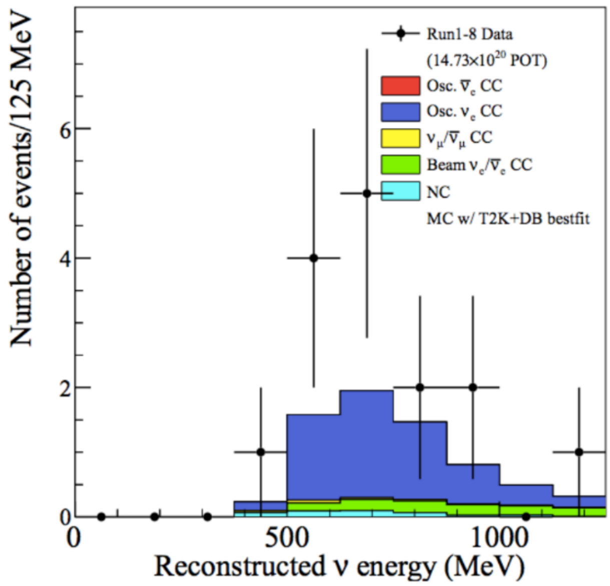

Figure 4.1: The number of events in Super-Kamiokande as a function of reconstructed neutrino energy expected for simulated MC and seen in data.

The ν_e CC π^+ analysis within this thesis aims to produce the world's first exclusive ν_e CC π^+ cross-section measurement on a Carbon target. Furthermore, the goal of the analysis is to develop a constraint on $\nu_e\pi^+$ background due to intrinsic ν_e contamination in the T2K beam using ND280 Tracker data. Data and MC comparisons in the low energy region of phase-space relevant to the far detector can also provide initial insights into whether an excess, similar to that observed in the far detector data, is also seen in the near detector dataset.

4.2 ν_e Inclusive Cross Section Measurement

The analysis outlined in this thesis inherits from a previous study to measure the ν_e CC inclusive cross-section using the ND280 tracker [86–88]. The primary motivation of that analysis was to develop a constraint on the intrinsic electron neutrino contamination in the T2K beam, the single largest background in the measurement of electron neutrino appearances at the far detector. The inclusive analysis measured electron neutrino and anti-neutrino cross-sections, in both FHC and RHC modes. Nevertheless, in this section we will only discuss electron neutrino

MC	Measured σ [10^{-39}cm^2 per nucleon]	Nominal σ [10^{-39}cm^2 per nucleon]	$< E >$ [GeV]
NEUT 5.3.2	6.62 ± 1.32(stat.) ± 1.30(syst.)	7.18	1.28
GENIE 2.8.0	6.93 ± 1.40(stat.) ± 1.33(syst.)	6.87	1.28

Table 4.1: Measurement of the ν_e inclusive cross-section result for two different MC sets, compared against the nominal predicted value. The mean neutrino energy, $<E>$, is also shown. Reproduced from [88].

measurements in FHC mode, as is the most relevant to the ν_e CC π^+ cross-section analysis provided in this thesis.

The ν_e CC inclusive signal was defined as any event that originated from a charged current electron neutrino interaction in the FGD1 fiducial volume, with additional phase space cuts applied to the outgoing electron; the inclusivity of the signal means it is not concerned with the composition of the hadronic final state of the interaction. The selection of electron neutrino candidates followed two distinct paths; the first rejected large muon backgrounds[1], the second reduced a prevalent photon background. The selection required excellent particle identification and was later adapted for the ν_e CC π^+ analysis in section 4.7.1. The dominant background post-selection comes from photon interactions primarily from π^0 decays. Approximately 60% of the photon background originated inside the FGD1 fiducial volume; the remaining fraction had interactions occurring in other parts of the ND280 detector, or through sand interactions. A significant amount of photon background was found to populate the low momentum and high angle regions, which was then constrained by an independent photon control selection. A summary of the selection depicted significant data-MC discrepancies in regions dominated by photon backgrounds. These regions are also dominated by large systematic uncertainties. Full details of the ν_e inclusive and photon sideband selections can be found in [86, 87].

The total ν_e inclusive cross-section was measured over a limited predefined phase-space ($p > 300$ MeV/c and $\theta \leq 45°$) using NEUT 3.2.0 and GENIE 2.8.0 MC; the results have been reproduced in table 4.1. Both results agree within error with the cross-section predictions given by their respective nominal MC. The data

[1]Pion and proton backgrounds are also rejected here but these backgrounds are smaller in magnitude

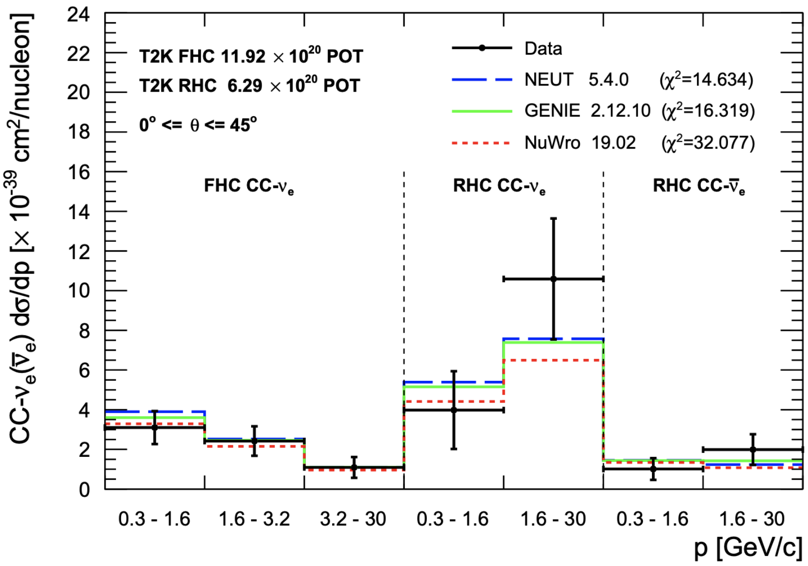

Figure 4.2: Flux integrated ν_e CC inclusive differential cross-section results, in a limited phase-space, as a function of reconstructed lepton momentum. Comparisons to different neutrino event generator models were made. Plot taken from [88].

was compared to cross-section predictions from recent neutrino generator models in NEUT 5.4.0, GENIE 2.12.10, and NuWro 19.02. The resulting plot, split into predefined regions of momenta space, is shown in figure 4.2. The best agreement over both FHC and RHC for (anti-)electron neutrinos is observed with NEUT 5.4.0. Nevertheless, all models agree within error for FHC electron neutrino interactions. The ν_e inclusive analysis provided the first CC-ν_e cross-section measurement using both FHC and RHC fluxes.

4.3 T2K Software

The T2K software framework used to perform the majority of this analysis was Highland2 (HIGH Level Analysis and the ND280 version 2) [89]. Highland2 provides a framework to analyse Monte-Carlo (MC) simulated and real data on an event-by-event basis. Event selection and cuts are performed on reconstructed objects based on their characteristics. Truth information is parsed throughout, and is used to test the relative performance of the selection.

Detector systematic uncertainties and error propagation are calculated and performed by Psyche (Parametrisation of SYstematics and CHaracterisation of Event) [89], a software package called by Highland2. The cross section and flux systematic uncertainties are evaluated using a combination of the T2KReWeight package, and parts of the nueXsLLFitter package which in turn has been used for the recent ν_e inclusive cross section result [88].

4.4 Data and Monte-Carlo Samples

The data sample analysed includes T2K runs 2-4, corresponding to 5.87×10^{20} POT after beam and ND280 data quality cuts are applied. In addition, T2K run 8 data is used giving an additional 5.73×10^{20} POT. The total exposure of the dataset used in this analysis is 11.60×10^{20} POT. The full set of ND280 MC produced for runs 2, 3, 4, and 8 was used. The exposure for this MC sample was 7.38×10^{21} POT for water in and 11.59×10^{21} POT for water out configurations, and a total of 18.96×10^{21} POT for the full MC sample. Only FHC mode data and MC are used for this analysis, therefore RHC runs 5-7 are not considered. Both MC and data samples were processed in T2K's software production 6T.

4.5 Signal Definition

The analysis presented in this chapter aims to measure the cross-section of charged current ν_e interactions that produce at least one positively-charged pion in the detector (after FSI). The following signal criterion are imposed on this analysis:

- The event must include an electron neutrino charged current interaction in the FGD1 sub-detector fiducial volume (FV). The FGD1 FV cut dimensions are $|x| < 874.51$ mm, $|y - 55| < 874.51$ mm, and $136.875 < z < 446.955$ mm. Where the x and y cuts are defined to match the outer boundaries of the central 182 scintillator bars[2], and the z cut is placed just after the first XY module but includes all remaining downstream modules [90].

[2]The 55 mm accounts for an offset relative to the ND280 coordinate system

- The interaction must produce an electron and at least one positive pion must exit the nucleus.

Any events that pass all of these criteria are defined as signal. For the cross-section measurement, additional phase-space constraints applied to the signal definition; these are outline further in section 4.9.1.

It should be noted that the analysis is not designed to select pions stopping in the FGD. Therefore when quantifying selection efficiency performance, a third signal criterion is imposed requiring at least one positively charged pion to pass from the FGD1 to the neighbouring downstream TPC. It should be noted that events in which the positively charged particle is mis-reconstructed as a pion, for example a CC-ν_e event whereby the π^+ is isolated in the FGD1 but the proton escapes, are defined to be signal events.

4.6 Significant Background Topologies

There are multiple background topologies that impose significant contributions to this analysis. For clarity, these will be grouped and defined as such:

- The most prominent background topologies in the analysis come from the production of π^0 which consequently decay into photons. There are a number of processes that can produce π^0 which each can mimic signal in different ways. These are:
  - γ **background OOFGD** - Interactions that occur outside of the FGD1, which produce π^0 that decay to photons. A significant contributing background to the ν_e inclusive analysis (40%), these background events can often mimic ν_e interactions as external photons interact in the FGD to produce electron positron pairs.
  - γ **background OOFGDFV** - Analogous to OOFGD photon background, this topology is based on photon production within the FGD, but outside the fiducial volume defined in section 4.5.

- γ **background ν_μ CC** - This photon background channel consists of events in which a ν_μ CC π^0 interaction that occurs in the FGD. This channel can mimic signal for a number of reasons, the most frequent being poor or no reconstruction of high angle muons in the FGD and/or TPC. Instead the selected lepton track is the final electron from the $\pi^0 \to 2\gamma \to e^+e^-$ decay chain. True positive pions are sometimes present in the event, but often positrons and protons are selected as the pion candidate track at low and high track momenta respectively. This occurs as the dE/dx curves used for particle identification intersect one another, as can be seen in figure 4.3. The true particle selected for the pion candidate track for this background can be seen in the appendix, figure A.1a.
- γ **background NC** - This topology is defined as π^0 production via neutral current interactions. Alongside the aforementioned ν_μ CC photon background, these two topologies make up the dominant photon background in this analysis, and mimic signal in similar manners. The outgoing neutrino remains undetected, whilst the selected lepton remains the electron from pair production. The true pion candidate track for this topology as a function of reconstructed momenta is shown in figure A.1b.

- The ν_e charged current background is split into two sample topologies. The largest single ν_e CC background contribution comes from ν_e CC 0π interactions. All other charged current topologies are defined as ν_e CC other.

- At ND280 the ratio of the total ν_e flux to total ν_μ flux, integrated over all energy space, is approximately 0.012. Naturally, the predominant background before selection cuts is from ν_μ interactions. The initial selection cuts, inheriting from the ν_e inclusive analysis, are designed to inhibit this background and promote selection of electrons as the main lepton track. Nevertheless, muons are occasionally selected as the lepton track, a problem more prominent within this analysis at higher energies.

4.7 ν_e CC π^+ Selection

The selection for this analysis inherits from the event selection used for the ν_e charged current inclusive measurement which is described in reference [86–88]. The principal philosophy of the ν_e CC π^+ selection was to stay as close to the ν_e inclusive selection as possible, to allow for comparisons to be made where necessary. All plots are created with P6T nominal NEUT 5.4.0 MC and, unless otherwise stated, are normalised to data by POT on a run-by-run basis. Plots that do not show data, typically representing truth level information, are normalised by total POT to the full data set.

4.7.1 Selection Cuts

A number of cuts are used during the selection to create a sample of events that maximises both selection efficiency and purity. The efficiency of a sample is the percentage of true signal events that remain in the sample post selection, relative to the number of true signal events pre selection. One can also measure the quality of a sample by the purity, defined as the fraction of signal events in the sample. In general, the addition of selection cuts increases signal purity at a cost to efficiency.

Starting from the ν_e inclusive selection, given in [86, 87], a number of cuts designed to reduce out-of-fiducial-volume (OOFV) photon background were removed. This increases signal efficiency, and can be done because the addition of selecting over a pion track naturally has the same effect. The final cuts for the ν_e CC π^+ selection are described below in the order in which they are implemented in the analysis. Unless otherwise stated, each plot demonstrating individual selection cuts is taken with $N-1$ cuts (all cuts but the one in question) applied.

Beam and ND280 Event Quality

The event must pass both T2K's beam quality and ND280's data quality cuts. Furthermore, the event time has to be reconstructed within one of the eight distinct beam bunches.

Track Multiplicity

At least two tracks must pass into the TPC downstream of FGD1.

TPC Track Quality

The TPC track quality cut is taken from the ν_e CC inclusive analysis. The most energetic negatively charged track that starts in the FGD fiducial volume is selected as the primary lepton. If this track passes into one of the Tracker-ECal modules, it is required to have at least 18 reconstructed hits within the TPC. Otherwise, it must contain 36 TPC hits. The minimum number of hits required is based on a previous study outlined in [91].

Particle Identification in the TPC and ECal

The particle identification cuts for the electron neutrino beam component, using the TPC and Tracker-ECal sub-detectors, was originally developed in 2013 [91]. The PID cuts are based on the measurement of the truncated mean of the ionisation loss (C_T) by the charged particles as it crosses the TPC gas. The mean value of the charge deposited by charged particles on MicroMegas columns across the TPC is computed. A truncated mean is used to avoid distributions being affected by Landau tails from ionisation processes in the gas. Only the mean value of 70% of the MicroMegas columns recording the least charge are considered. This value has been optimised and TPC performances are outlined in [92, 93]. The distribution of the truncated mean versus the reconstructed TPC momentum is shown for positive and negative tracks in figure 4.3. To perform particle identification a pull variable, δ_i, is defined as:

$$\delta_i = \frac{C_T^{meas} - C_T^{exp}(i)}{\sigma^{exp}(i)} \tag{4.1}$$

where i represents different particle species hypotheses, C_T^{meas} and C_T^{exp} are the measured and expected energy losses of particle i respectively, and σ^{exp} is the resolution of the deposited energy measurement.

Pull values for cuts have since been defined for the ν_e inclusive analysis, and are outlined in [87]. For this analysis, pull values were once again tuned to maximise

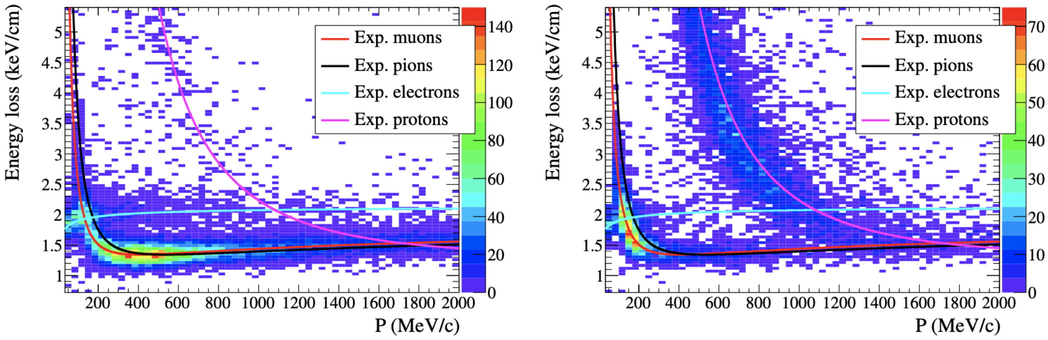

Figure 4.3: Distribution of TPC ionisation loss as a function of reconstructed TPC momentum. The distribution is for the candidate lepton track starting within the FGD fiducial volume. Negative tracks are shown left, positive tracks are shown right. The expected curves for typical particle types are superimposed.

signal efficiency and purity, using nominal control MC which is then tested on a different set of MC.

If the selected lepton candidate track does not pass into the ECal, it is rejected if it fails any of the following cuts.

- $-1.5 > \delta_e$, or $\delta_e < 2.5$
- $-2.5 < \delta_\mu < 3.0$
- $-2.5 < \delta_\pi < 3.0$

These cuts are shown in figure 4.4.

In addition to the TPC pull cuts, if the momentum of the selected track is less than 300 MeV/c and enters the ECal, it must pass the ECal MIP-Shower PID cut, MIPEM > 0. If the selected lepton tracks momentum is above 300 MeV/c, the TPC and ECal PID criteria for selection are changed. The threshold of 300 MeV/c is chosen because above this value, the Ecal PID can separate MIP from showers with good accuracy. A relaxed TPC electron pull criterion of $-2.0 < \delta_e < 2.5$ is first used. The ECal PID cut is then dependent on the lepton's momentum. If the selected track has a momentum larger than 800 MeV/c it and is fully contained in the ECal, it must have an ECal energy greater than 1000 MeV to pass the PID. This is shown in figure 4.5a. Otherwise, if $p < 800$ MeV/c or the ECal track is not fully

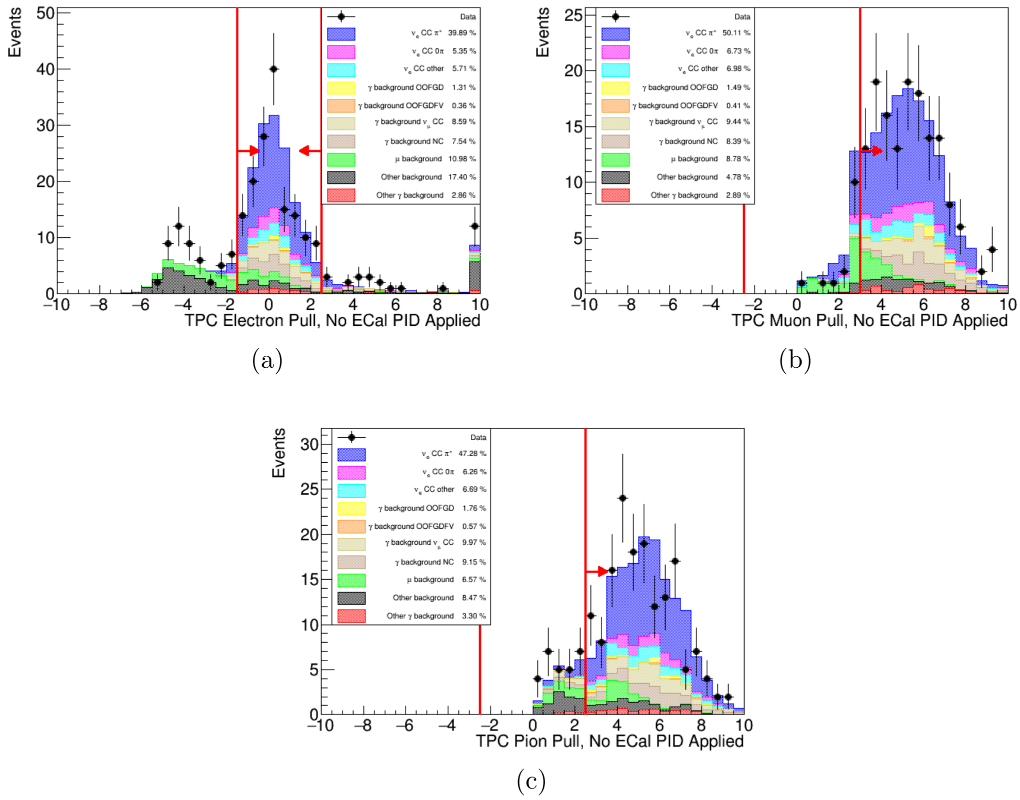

Figure 4.4: The TPC particle identification cuts on (a) the electron pull, (b) the muon pull, and (c) the pion pull.

contained, the track must pass an ECal MIP-Shower PID, MIPEM > 5, shown in figure 4.5b. Furthermore if the track does not contain at least 36 hits in the TPC, it must pass the same pion pull as the TPC PID.

Second TPC PID

Often the main lepton track can propagate into the TPC3 subdetector, the second TPC downstream of the FGD1. If the lepton track has at least 18 TPC3 hits it is subject to a second PID cut. The track is rejected if the muon pull falls between $-2.0 < \delta_\mu < 1.5$. The cuts main objective is to reduce muon background and is shown in figure 4.6. The cut window was chosen to match the CC ν_e inclusive analysis [86].

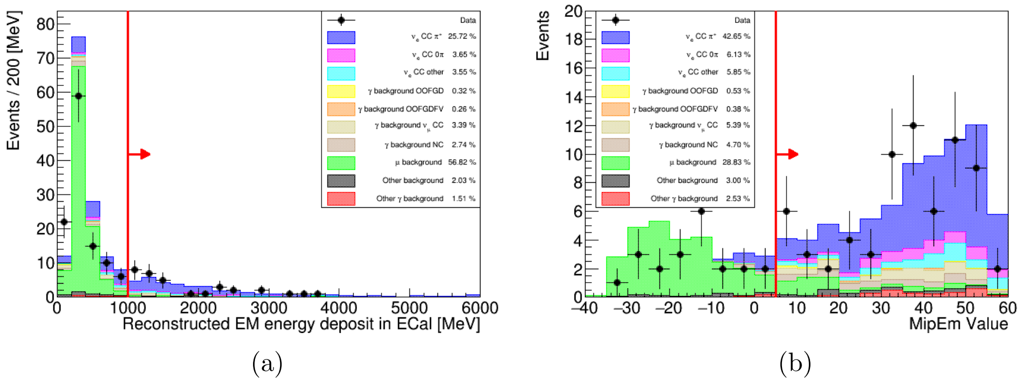

Figure 4.5: (a) The number of events as a function of reconstructed EM energy deposited in the ECal. Cut is used on tracks with momentum above 800 MeV/c. (b) A MIP-Shower cut used on tracks fully contained in the ECal with momentum below 800 MeV/c. A negative value indicates more MIP-like, a positive value indicates more EM shower like.

Momentum

Inherited from the ν_e inclusive selection, the main lepton tracks that pass the initial TPC quality and PID cuts are required to pass a lower bound momentum cut of $p > 200$ MeV/c. The reason for the cut is the observed large background of electrons from neutrino induced photons, which can be seen in figure 4.7.

Pion Selection

The previous cuts up to now all had the primary objective of selecting ν_e events. For this analysis we want to investigate ν_e events that produced at least one π^+ in the final state through charged current interactions. To find π^+ candidate tracks, all secondary tracks (that are not the main selected lepton track) that originate from a vertex in the FGD1 and propagate into the TPC2 are considered. The candidate track must have a positive charge and originate within 40 mm of the start of the main lepton track. A cut of 40 mm was established through figure 4.8a. Here, it can be seen that a cut of 40 mm optimises the selection purity, reducing the overall photon background levels. Bins of 10 mm were chosen to match the z-dimensions of each FGD scintillator bar.

Once positive pion candidate tracks have been found, the tracks must pass a

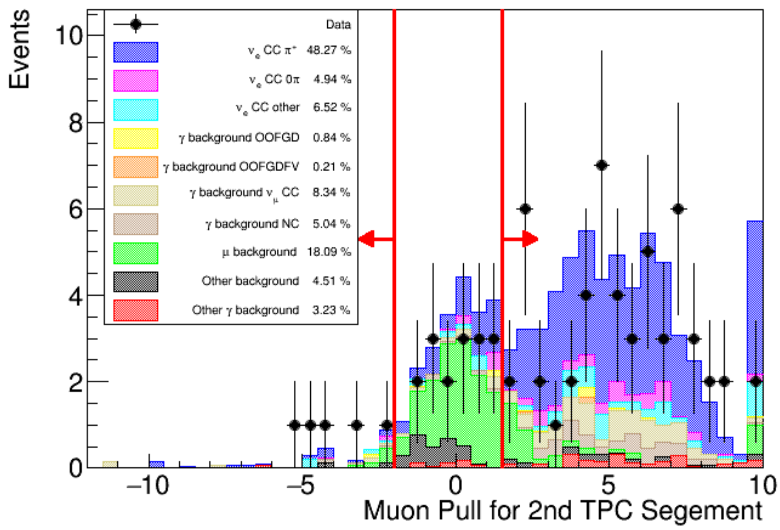

Figure 4.6: The number of events as a function of muon pull in the TPC3. Used for the second TPC PID cut to remove muon background.

particle identification cut. The track is rejected if the pion pull does not lie within $-4.0 < \delta_\pi < 4.0$, as shown in figure 4.8b. These boundaries were found to optimise selection purity in samples of nominal MC. If multiple tracks pass the cuts described above, the highest momenta track is selection as the pion candidate track moving forward in the analysis.

Invariant Mass

Selecting a π^+ in the final state effectively removes a large fraction of the OOFGD photon background that is a significant background in the ν_e inclusive analysis. Nevertheless, an additional invariant mass cut is used to veto the OOFGD and OOFGDFV background further. The invariant mass cut takes the preselected main lepton and pion candidate tracks as a pair. The invariant mass for the pair of tracks is then calculated using the following expression:

$$m_{\text{inv}}^2 = m_i^2 + m_j^2 + 2(E_i E_j - \mathbf{p_i} \cdot \mathbf{p_j}) \tag{4.2}$$

Whereby particles i and j are represented by their mass, m, energy, E, and momentum three-vector, $\mathbf{p}$. The particle tracks are assumed to be an electron positron pair, and

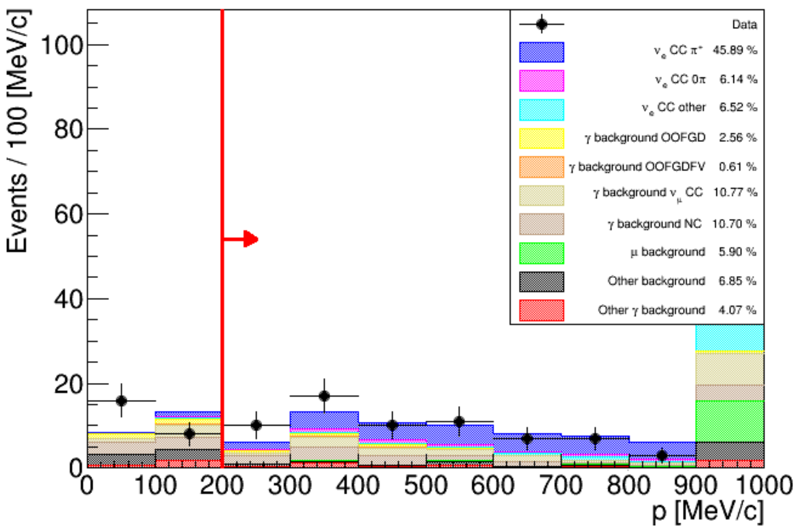

Figure 4.7: The number of events as a function of reconstructed lepton momentum, for the low momentum cut reducing photon background.

thus equation 4.2 becomes:

$$m_{inv} = \sqrt{2m_e^2 + (E_1E_2 - \mathbf{p_1} \cdot \mathbf{p_2})} \tag{4.3}$$

Here, 1 and 2 represent the main lepton and pion candidate tracks respectively, and the electron rest mass, m_e, is taken as 0.511 MeV. A cut is placed rejecting all tracks that do not have $m_{inv} > 110$ MeV, assuming they originated from a photon. A threshold of 110 MeV was chosen to follow the ν_e inclusive analysis. The cut can be seen in figure 4.9, and is successful in reducing large amounts of photon backgrounds.

Momentum Quality

The momentum quality cut removes track above 200 MeV/c with negative muon or pion TPC pulls. It was observed in [86] that tracks with negative muon (pion) pull fall below the TPC muon (pion) dE/dx curves and as a result are far away from the TPC electron hypothesis, this is seen in figure 4.3. The cut is named the 'momentum quality' cut as the majority of events attributed to this region are low momenta events mis-reconstructed to a higher momentum. The performance of the

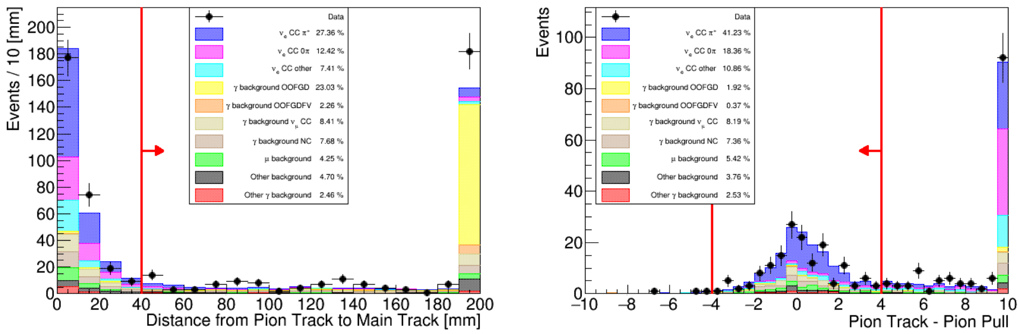

(a) (b)

Figure 4.8: The cuts used in positive pion selection. (a) The distance between the pion candidate track and the main lepton track. (b) The pion TPC pull used for PID.

cuts can be seen in figure 4.10.

ECal Veto

Post pion selection and invariant mass cut, the most predominant photon background comes from ν_μ CC, and NC, π^0 production (described in section 4.6). The background usually arises due to mis-reconstructed muons in the FGD or TPC, predominantly caused by high incident angle. It was noticed many of these high angle muons are often reconstructed in tracker ECal modules. To veto this type of event, all reconstructed ECal objects are considered. A vector is then drawn between the start of the main lepton track, and the most upstream segment of the ECal object. This is demonstrated in figure 4.11. The polar angle, θ, with respect to the z-axis is then taken. A cut is made rejecting events below 1 GeV with $\cos(\theta) < 0.6$, removing potential high angle muon events. The cut is shown visually in figure 4.12, and it can be seen that the majority of background events rejected are ν_μ CC photon events.

4.7.2 Full Selection

A summary of the ν_e CC π^+ selection, after all cuts are applied, is outlined in this section. The number of events post selection as a function of reconstructed kinematic phase space for the selected lepton and pion tracks, is shown in figures 4.13 and 4.14 respectively. In general, the selection favours forward going lepton tracks recon-

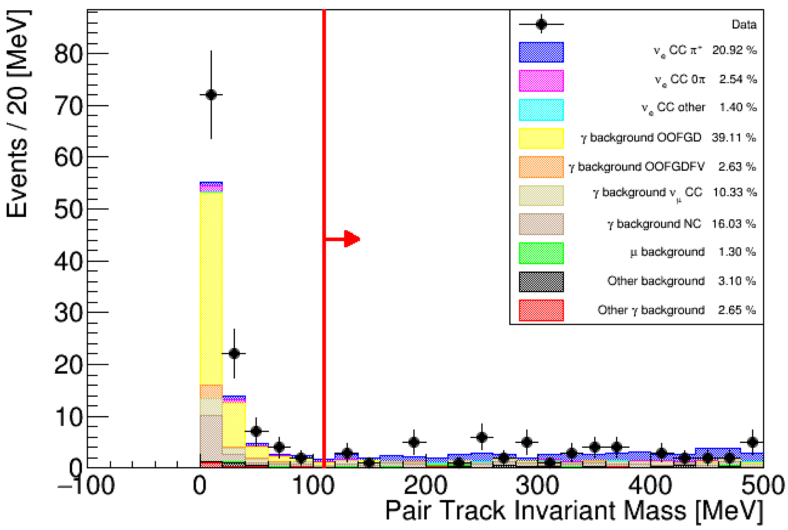

Figure 4.9: The invariant mass of the pion candidate track - main lepton track assuming an e^+e^- pair. The cut aims to removes out of fiducial volume photon interactions.

structed in the low momenta region (above $p > 300$ MeV/c). Detector systematic uncertainties on MC are shown, and errors in data are driven from statistics. The data-MC agree within error, particularly with respect to track direction. The total number of data events selected is 152, to be compared with the a total number of POT normalised selected MC events of 160.6. The predominant background in the low lepton track momenta region up to 1.5 GeV is from ν_μ charged current and neutral current π^0 interactions, liberating photons inside the FGD1 fiducial volume. Above 1.5 GeV, the total background has a larger relative contribution from other ν_μ CC interactions, and are the dominant background at high momenta. Finally, backgrounds from other ν_e charged current interactions are most prominent up to approximately 3 GeV.

With a signal selection purity of approximately 51% the total number of signal MC events predicted is 82. The signal events can be further broken down into reaction topology to investigate the relative contributions of each interaction mode in ν_e CC π^+ production. The interaction topologies are shown in figure 4.15a as a function of reconstructed lepton momentum. The vast majority of signal events originate from deep inelastic scattering ($\sim$56%) and resonant ($\sim$40%) interactions. Charged current

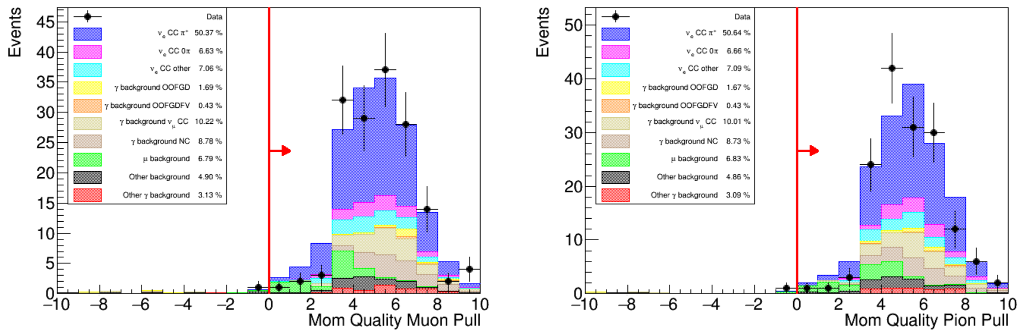

(a) (b)

Figure 4.10: The momentum quality cut removing tracks above 200 MeV/c if they have negative (a) muon pull, or (b) pion pull.

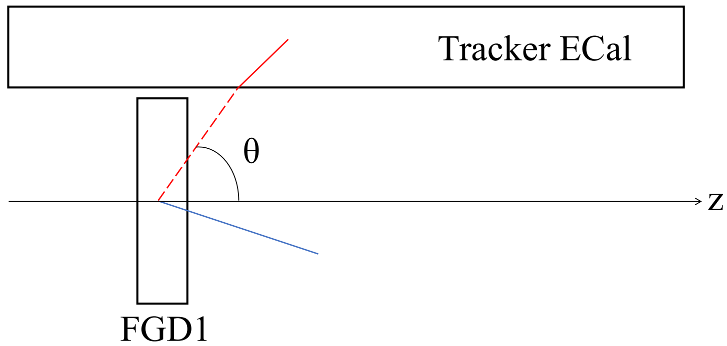

Figure 4.11: Schematic representation of the θ variable used in the ECal Veto cut. The main lepton candidate track is shown in blue, the red solid line represents a reconstructed ECal object, and the red dotted line is the vector joining the two. The FGD1 and Tracker-ECal are shown for context, the other ND280 modules are not shown.

coherent scattering interactions also provide a non-negligible contribution to the total number of signal events. The true number of π^+ particles exiting the same vertex as the lepton track in signal events is shown in figure 4.15b. Approximately 84% of signal events liberate exactly one positive pion from the true interaction vertex. The remaining events, with more than one π^+ produced, originate from DIS interactions only. The true particles selected for both the reconstructed lepton and pion candidate tracks, as a function of track momentum, is broken down in the appendix, figure 4.16. It can be seen that in the full selection, an e^- is correctly selected as the main lepton track roughly 90% of the time. The main sources of misidentification arise from selecting μ^- (6.6%) and π^- (1.6%) from the muon

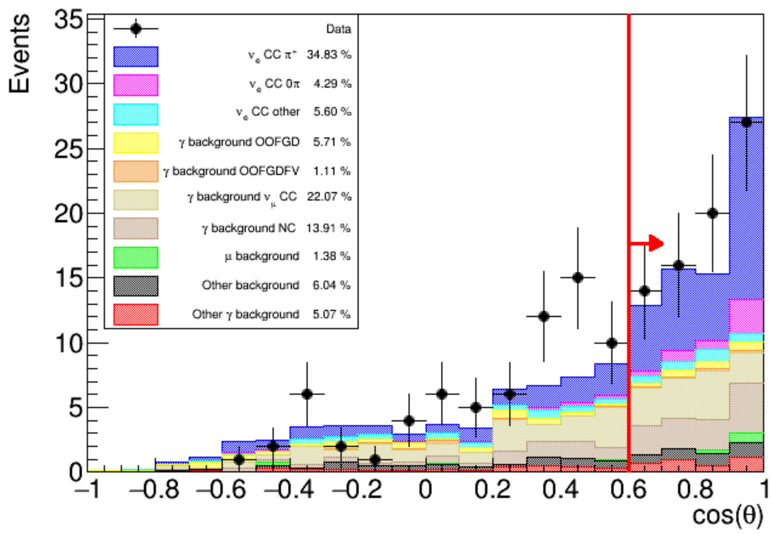

Figure 4.12: The number of events as a function of polar angle used in the ECal veto cut. The angle θ is schematically represented in figure 4.11.

background ,and other background topologies, respectively. The relative performance of pion track selection is divided with respect to momentum space. Below 1.2 GeV, positive pions are selected roughly 77% of the time, whereas above this threshold π^+ tracks are only selected 28% of the time with protons selected at a rate of 62%. This is because the pions and protons have similar energy loss curves in gaseous TPCs above approximately 1.2 GeV (figure 4.3) and thus become indistinguishable through PID pulls. For the signal topology only, π^+ selection is better at 89% and 41% in low and high momenta regions respectively. It should also be noted that events in which a proton is selected as the π^+ candidate track are still signal assuming at least one true π^+ particle is liberated from the same true vertex as the main lepton track.

4.7.3 Efficiency & Purity Of Selection

The performance of the selection criteria is indicated by the signal efficiency and sample purity. The efficiency defines how many of the signal events pass particular cuts in question (equation 4.4). The purity defines the number of signal topology events as a fraction of the total events (equation 4.5). The efficiency is calculated at

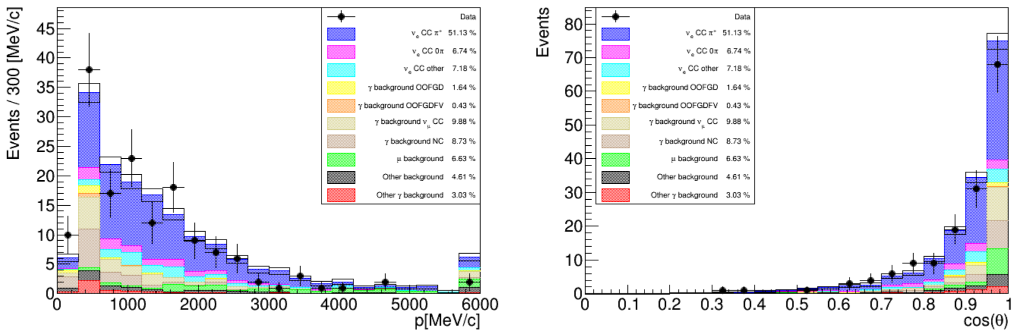

(a) (b)

Figure 4.13: The full selection as a function of the lepton track reconstructed kinematic variables.

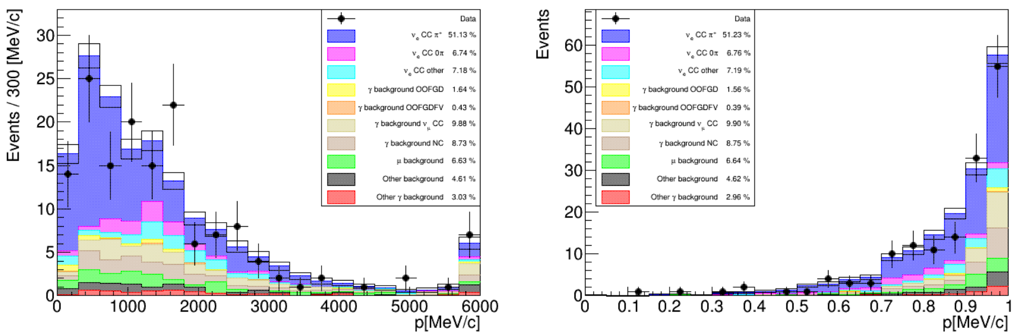

(a) (b)

Figure 4.14: The full selection as a function of the pion candidate track reconstructed kinematic variables.

the truth level, whereas the purity is measured at the reconstructed level.

$$\text{Selection Efficiency} \;=\; \frac{\text{Number of true signal events selected}}{\text{Total number of true signal events}} \tag{4.4}$$

$$\text{Selection Purity} \;=\; \frac{\text{Number of signal events selected}}{\text{Total number of events selected}} \tag{4.5}$$

The values for selection efficiency and purity, tracked over the full selection cut-by-cut, is shown in figure 4.17. This plot provides a good representation of the efficiency and purity performance as the selection cuts are made. However, one should not evaluate individual cut performance from this plot as there is a dependence on the ordering of such cuts. Instead, to evaluate individual cut performance, the $N-1$

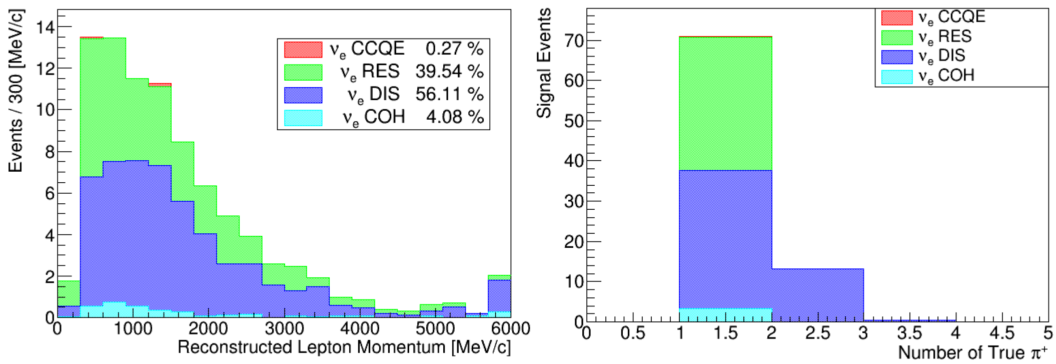

(a) (b)

Figure 4.15: (a) The number of signal events as a function of reconstructed lepton momentum broken down by interaction types. (b) The true number of π^+ particles produced in the signal, broken down by interaction type.

plots shown in section 4.7.1 are better estimators.

Using the signal definition defined in section 4.5, efficiency and purity values for the full selection can be quantified. The efficiency post-selection, without any phase-space constraints applied, is calculated to be $(13.8 \pm 0.3)\%$. The signal purity in the final selection is $(51.1 \pm 0.9)\%$. Imposing the optional signal criterion that the true pion passes from the FGD1 to the neighbouring downstream TPC, the selection efficiency is $(19.9 \pm 0.5)\%$. With phase space constraints applied, as defined in section 4.9.1 for the cross-section measurement, the efficiency increases to $(25.4 \pm 0.6)\%$ over the full selection. The uncertainties in efficiency and purity are taken as the binomial error in calculating them. Calculations of systematic uncertainties affecting the signal efficiency are outlined in section 4.8.

4.8 Systematic Uncertainties

The experimental methodology of this analysis at it's most fundamental level is a measurement of reconstructed event rates both in MC and real data. The MC predictions on reconstructed event rates at the near detector can be generally described for this analysis as:

$$R(x) = \int_{E_\nu} \Phi_{\nu_e} \times \sigma(E_\nu) \times T \times M(x_{true},\ x_{reco}) \times \epsilon(x_{true}) \tag{4.6}$$

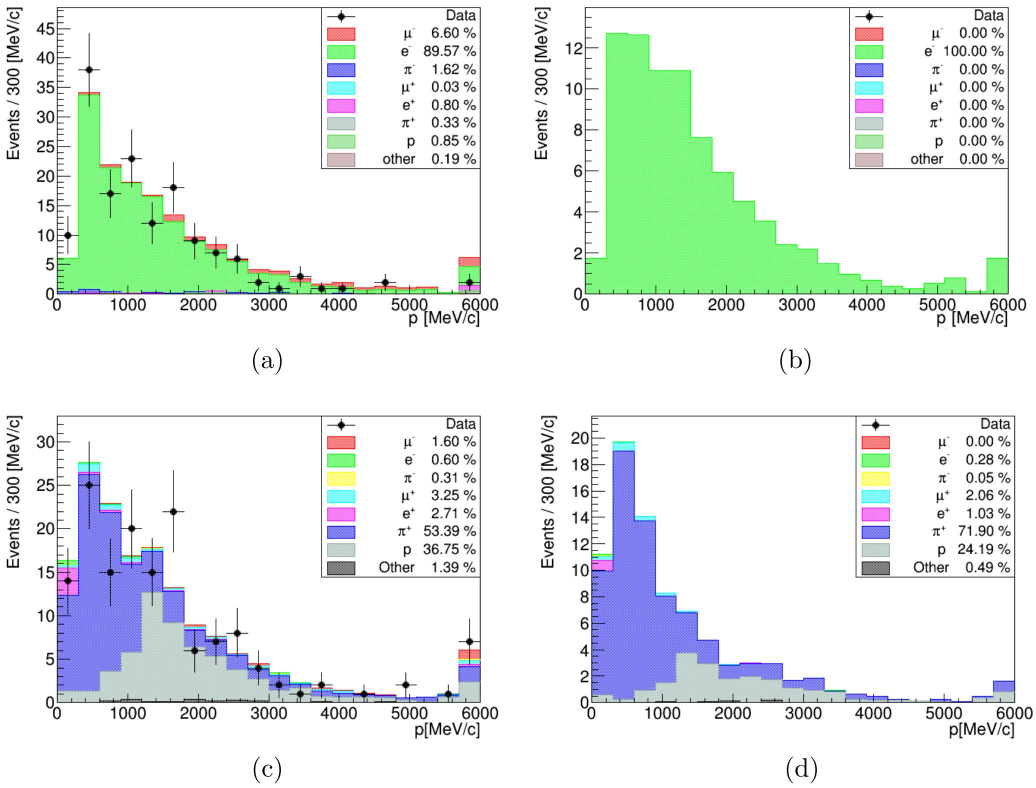

Figure 4.16: The true particle information for the reconstructed lepton track (above) and pion candidate track (below), as a function of track momentum. The full selection is displayed on the left, the signal only is on the right.

where R is reconstructed event rate as a function of reconstructed variables, x, for this analysis; Φ_{ν_e} is the electron neutrino flux; σ is the neutrino interaction cross-section as a function of neutrino energy; T is the number of target nucleons; M describes the migration matrix from true to reconstructed variables; and is the ϵ is the detector efficiency as a function of true variables. Equation 4.6 shows the importance of understanding flux, cross-section model, and detector systematic uncertainties in order to accurately predict the expected number of reconstructed events observed in the near detector. This section will discuss the calculation and propagation of the relevant errors associated to these three sources of systematic uncertainties. Unless stated otherwise, all systematic uncertainties have been evaluated over one global momentum bin from 0 to 30 GeV, and verified using one bin covering the entire angular phase space, $\cos(\theta) = -1$ to $\cos(\theta) = 1$.

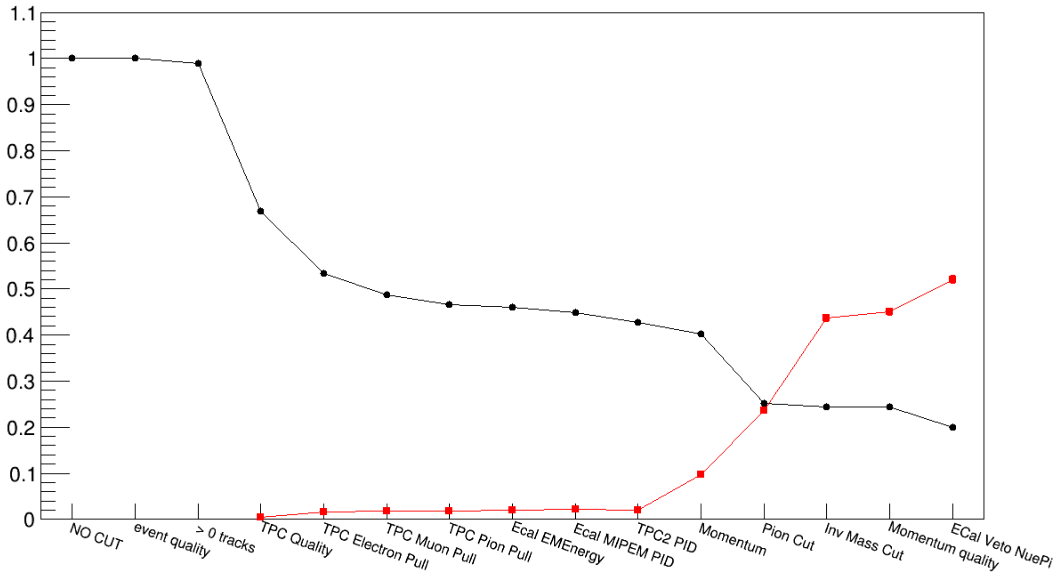

Figure 4.17: Selection efficiency (black) and selection purity (red) as a function of the cuts applied, shown for each stage of the selection. The purity is only shown from the TPC quality cut, but can be assumed to be negligible before this cut.

4.8.1 Detector Systematic Uncertainties

The detector systematic uncertainties encapsulate the performance of each ND280 sub-detector. The systematic uncertainties are evaluated using the Highland2/Psyche software packages. The systematic uncertainties are split into two categories: variation and weight. Variation systematic uncertainties modify the properties of objects at the event level, whereas weight systematic uncertainties alter the final weight of the event passing the selection. The decision of whether a systematic uncertainty is parsed as weight or variation, is defined by the systematic uncertainties affect on the event. For example, if the uncertainty affects a continuous parameter it must be implemented as variation; however if the uncertainty affects only event normalisation it can be treated as a weight. The exception here is if the systematic affects a binary parameter, for example charge identification. In this case, it may be implemented as either variation or weight. Efficiency systematic uncertainties are applied as a weight that depends on more than one variable, and are calculated through comparisons of data and MC predictions for well known control samples.

A full list of the detector systematic uncertainties for both variations and

Systematic Uncertainty	Type	Fractional Error (%)
TPC PID	Variation	1.80
TPC Momentum Resolution	Variation	0.48
TPC Momentum Scale	Variation	0.16
B-Field Distribution	Variation	0.19
ECal EM Energy Scale	Variation	0.31
ECal EM Energy Resolution	Variation	0.07
TPC-ECal Matching Efficiency	Weight	1.91
TPC-FGD Matching Efficiency	Weight	0.17
TPC Track Efficiency	Weight	1.29
TPC Cluster Efficiency	Weight	0.01
FGD Mass	Weight	0.58
Charge ID	Weight	0.68
OOFV	Weight	1.26
Pion Secondary Interactions	Weight	2.01
Proton Secondary Interactions	Weight	2.04
ECal PID	Weight	0.75
ν_e CC π^+ ECal Pile Up	Weight	0.48
FGD Vertexing	Other	1.40
Total	-	4.51

Table 4.2: A full summary of the fractional errors of all detector systematic uncertainties considered for this analysis. The systematic type is also shown. Fractional errors on the number of selected events for the full selection have been calculated over 250 toys.

weights can be seen in table 4.2. The fractional error on predicted number of events over the full selection was calculated using 250 toy experiments for each systematic uncertainty. The majority of the ND280 tracker systematic uncertainties are shared with the ν_μ and ν_e inclusive analyses; full descriptions of these systematic uncertainties can be found at [94] and [88] respectively. As a brief overview the systematic uncertainties and their relative affects on the selection are described below:

- The **TPC PID** systematic for muons, electrons, and pions is estimated using dedicated control samples directly extracted from beam events. The systematic is then estimated from the data-MC differences observed in the pull distributions, which is computed using a Gaussian and considering the correct particle hypothesis.

- The **TPC momentum resolution** compares the differences in TPC and global momentum resolutions of data and MC. A smearing factor is then applied as the systematic parameter is propagated through event selection. **TPC momentum scale** uncertainty is taken from the B-field measurement described in [95].

- **B-field distribution** systematic performs corrections using two separate methods. The main correction applies a $\vec{B}$ field map, at the reconstruction level, developed using measurements of the magnetic field inside the ND280 basket. The second, an empirical correction, is based on a laser system which illuminates aluminium dots on the cathode where expected and measured positions are compared. Magnetic field systematic uncertainties are described fully in [96].

- All ECal systematic uncertainties are discussed in full detail in [97]. The ECal EM energy systematic uncertainties are evaluated by comparing first and second moments measured by the TPC. The fractional difference is defined as:

$$\text{Fractional Difference} = \frac{\text{EM Energy} - \text{TPC Momentum}}{\text{TPC Momentum}} \tag{4.7}$$

  The systematic mean and standard deviation define the **ECal EM Energy Scale** and **ECal EM Energy Resolution** systematic uncertainties respectively.

  Control samples for the **ECal PID** systematic use cuts of MIP-EM $>$ 0 and EM-HIP $>$ 0. The efficiency for each particle type is then calculated for both data and MC. Any difference in data and MC samples is interpreted as the systematic error in the modelling of the ECal PID for that particle type.

- The **TPC cluster efficiency** is the probability of finding a cluster (group of adjacent single TPC pad hits) that corresponds to one point in the long trace of ionized gas created by charged particle tracks in the TPC. Data-MC discrepancies over both horizontal and vertical directions are used to calculate cluster efficiencies.

- The ability in which tracks crossing the TPC are able to be reconstructed is held within the **TPC track efficiency** parameter. Included in the systematic is the evaluation of both TPC pattern recognition and likelihood fit.

- **Charge sign identification** systematic assesses global charge identification based on the combination of ND280 subdetectors. Two errors are propagated here: The probability of swapping the local TPC charge identification, and probability of the global tracking to swap the sign of the charge. The systematic is explained in full in [98].

- **TPC-FGD** and **TPC-ECal matching efficiencies** characterise the performance of matching reconstructed tracks in the associated subdetectors. Descriptions of the control samples and performances of TPC-FGD and TPC-ECal matching efficiencies can be found in [97] and [99].

- The **FGD mass** systematic compares the areal density of an XY FGD module to MC values in the ND280 software. This is then combined in quadrature to the spread in masses over XY modules to give the full systematic uncertainty. Full detailed are given in [100].

- **Secondary interaction** systematic uncertainties, for both pions and protons, characterise the uncertainty in the probability for each particle type to undergo interactions outside the nucleus in which it was produced. The pion secondary interactions are modelled using the NEUT cascade method described in [101]. Proton secondary interactions are modelled through Geant4 [102]. Proton secondary interaction uncertainties play an important role in this analysis given the difficulty in separating pions and protons identification at high momenta (see figure 3.8), and therefore likelihood of selected protons as pion candidates. These systematic uncertainties account for discrepancies between data and the models used in MC, and are significant in this analysis.

- The **OOFV** systematic characterises the case in which the event is reconstructed as originating within the FGD fiducial volume, yet the true vertex is outside. A recent study [103] estimated that the OOFV error could be as large as 100% for analyses with predominant photon backgrounds. If the true vertex is outside of the FGD a conservative systematic uncertainty of 100% is assumed, following the ν_e inclusive analysis [87]. If the true vertex originates inside the FGD but outside the FV, data-MC discrepancies in control samples are used, following the treatment in [104].

ν_e CC π^+ ECal Pile Up Systematic Uncertainty

The dominant uncertainty associated to the Ecal veto cut is event pile up in the side Tracker-Ecals. In the case where a sand muon event is in coincidence with a magnet event, the activity caused by the sand muon may trigger the veto. This behaviour is not simulated in the MC, and therefore needs to be characterised in the ν_e CC π^+ ECal pile up systematic.

The systematic is evaluated by counting the number of ECal events in a separate sand muon MC sample with a fixed POT. The data intensity, defined as POT/$\mathrm{N_{Spills}}$, (for data, MC and sand MC) is then computed from the respective data samples and used to calculate the effective number of spills. With eight bunches per spill, the number of ECal events per spill can be translated to bunches for each dataset. The number of events should be reduced in the MC since pile up is not considered. Therefore a re-weight reduction factor is used:

$$w_c = (1 - C_{\mathrm{pileup}}) \tag{4.8}$$

where C_{pileup} is the correction to be applied and is defined as the number of sand ECal events per bunch.

There is an intrinsic 10% uncertainty in the total rate of sand muon interactions in neutrino simulations [104]. This value is used for both ν_μ and ν_e T2K cross-section analyses. Moreover, there are potential differences between data and MC arising from actual and simulated beam and detector properties. The uncertainty

	ECal/bunch (%)				
Sample	Data	MC	Sand	C_{pileup}	σ_{pileup}
Run 2 - Water Out	16.6265	12.0846	4.23594	0.0423594	0.00423594
Run 2 - Water In	14.3929	10.4291	3.61622	0.0361622	0.00361622
Run 3b - Water Out	15.1766	11.7413	4.16571	0.0416571	0.0073044
Run 3c - Water Out	18.1378	12.9605	4.59826	0.0459826	0.00579119
Run 4 - Water Out	22.4739	16.3985	5.81668	0.0581668	0.00581668
Run 4 - Water In	20.1549	14.5733	5.11788	0.0511788	0.00511788
Run 8 - Water Out	39.7411	30.0092	11.722	0.11722	0.0199007
Run 8 - Water In	35.0465	26.18	10.1318	0.101318	0.0126531

Table 4.3: Table showing the correction, C_{pileup}, and systematic uncertainty, σ_{pileup}, values over each run sample for data, nominal MC, and sand MC. The number of ECal events per bunch is also shown.

in data-MC differences is evaluated by

$$\Delta_{\text{data}-\text{MC}} = C_{\text{data}} - (C_{\text{MC}} + C_{\text{pileup}}) \tag{4.9}$$

where C_{data} and C_{MC} are the number of data and nominal MC ECal events per bunch respectively. Combining these two uncertainties is double counting, and thus the larger uncertainty of the two is taken as the pile up systematic uncertainty, σ_{pileup}. Table 4.3 shows the final values for C_{pileup} and σ_{pileup} for ECal pileup for each data period. A more detailed breakdown of the numbers used to evaluate the correction systematic uncertainties is shown in table A.1.

FGD Vertexing Systematic Uncertainty

Within the pion cut, described in section 4.7.1, a parameter is defined to measure the distance between the start of the lepton track and start of the pion candidate track, as described in figure 4.8. This parameter is most sensitive to the ability to accurately reconstruct the position of vertices within the FGD.

A selection has been developed to create a control sample of electron-positron pairs in the FGD1, in which the main lepton track is the electron. The selection uses the electron neutrino selection cuts, described in section 4.7.1, up to and including the

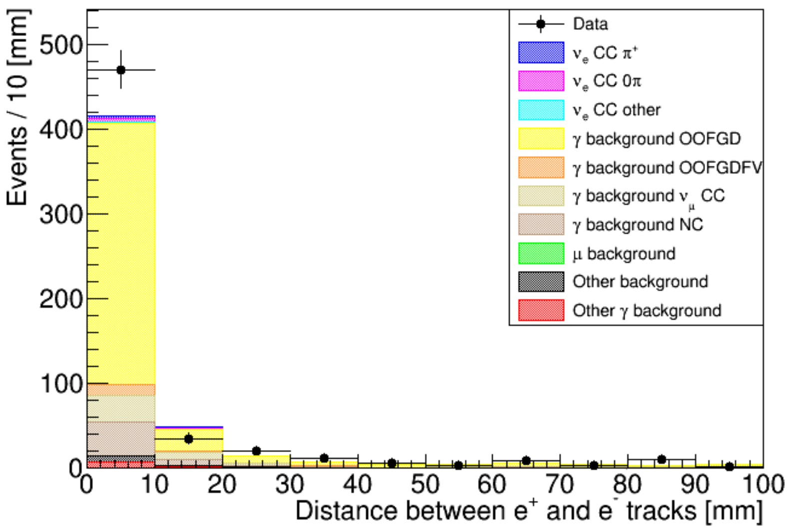

Figure 4.18: The distance between the selected tracks in electron-positron pairs used to calculate the vertexing systematic.

momentum cut. An additional cut to veto electron-positron pairs is then applied. All FGD1 to TPC2 tracks with opposite charge to the main lepton track are considered as pair candidates. Electron-like particle identification is performed using the longest segment of the reconstructed track inside the TPC, which in turn must pass TPC track quality cuts. The track is accepted as a pair candidate if it passes an electron pull PID of $-3.0 < \delta_e < 3.0$. Next, partnered with the main lepton track, the pion candidate track must have an invariant mass $<$ 110 MeV/c, the inverse cut to that described in section 4.7.1.

Analogous to the separation of pion and lepton tracks in figure 4.8a, the distance from the electron and pair candidate track is shown in figure 4.18. The distribution of data here appears narrower than MC. To attribute a systematic uncertainty, the efficiency of any cut on the given distribution was calculated using:

$$\epsilon_{data} = \frac{N_{data\,<\,x}}{N_{data}} \tag{4.10}$$

$$\epsilon_{MC} = \frac{N_{MC\,<\,x}}{N_{MC}} \tag{4.11}$$

where ϵ is the cut efficiency and x is the chosen value for the cut. To match the pion selection, x is chosen to be 40 mm. The vertexing error is then calculated by:

$$\text{Vertexing Error} = 1.0 - \left(\frac{\epsilon_{\text{data}}}{\epsilon_{\text{MC}}}\right) \tag{4.12}$$

This equates to a vertexing error of 1.4% at a cut value of 40 mm. The vertexing error is of course a function of the cut value, and can thus be increased (decreased) by tightening (relaxing) the pion selection cut respectively. A cut value of 40 mm was deemed to be tight enough to optimise selection purity without introducing a dominant systematic error.

In verifying the relevance of this systematic uncertainty to the ν_e CC π^+ selection, potential kinematic differences between the FGD vertexing sample and the ν_e CC π^+ selection sample have been considered. Different Q^2 values in ν_e CC π^+ and e^+e^- interactions could lead to different angular distributions between the two selected tracks. The angle between the two selected tracks in each sample is shown in figure A.2, where no major differences in distribution shape were found.

Discussion of Detector Systematic Uncertainties

The largest detector systematic uncertainties are in the secondary interactions of pions and protons. This is expected given the pion selection within the analysis, and the fact secondary interactions are known to be a large systematic uncertainty in T2K. The interactions pions and protons undergo, outside the nucleus it was produced in, are found to differ greatly between interaction models such as Geant4 and NEUT, and in comparison to external data [104]. The proton secondary interactions contribute similarly to pions as above approximately 1.2 GeV, protons and pions a relatively indistinguishable through energy loss methods in the TPC. In addition TPC PID and TPC-ECal matching efficiencies are significant detector errors to this analysis. All detector systematic uncertainties were cross-checked and validated against the ν_e inclusive analysis found in [86]. The major differences between these analyses is the additional selection of a π^+ candidate track, as well as the subsequent suppression of OOFV photon backgrounds. Errors including TPC PID, TPC track efficiency, Charge ID, and TPC-ECal matching efficiency see comparable increases from the

	γ Bkg (%)	ν_e CC Bkg (%)	All Other Bkg (%)	Signal Efficiency (%)
Systematic Uncertainty	3.12	2.10	2.82	4.13

Table 4.4: A summary of the combined detector systematic uncertainties on background topology event yields. Each background topology uncertainty is normalised relative to its contribution to the total background. The detector systematic fractional error on signal efficiency in a limited phase space is also shown.

Background Topology	Fraction of Total Background (%)
γ Background	47.8
ν_e CC Background	28.6
All Other Background	23.6

Table 4.5: The relative fraction each predefined background topology contributes to the total background event yield.

ν_e inclusive analysis due to the identification and tracking of an additional particle. Conversely, the previously dominant OOFV systematic has decreased significantly with the reduction on OOFV photon background yields. Nevertheless, no unexpected differences in detector systematic uncertainties can be seen between the two analyses that cannot be explained by inherent differences in the selection methods.

For cross-section measurements it can be more useful to measure the effect of systematic uncertainties on the event yields to different final state topologies, as well as the signal efficiency. Table 4.4 shows the combined effect detector systematic uncertainties have on different background topologies and the signal efficiency. Each background topology uncertainty is normalised to the relevant fraction each topology contributes the total background event yield, as shown in table 4.5. Weighting the uncertainties to topology size provides more context on the detector systematic effects on the full sample. The effect of detector systematic uncertainties upon the total background event yield is 6.08%. The ν_e inclusive analysis sees a background uncertainty from detector effects of approximately 12.7%. The decrease in uncertainty in this analysis is attributed to the significant drop in OOFV photon background. The uncertainty on signal efficiency due to detector effects without phase space constraints applied is 4.22%. In the limited phase space defined in section 4.9.1, the uncertainty on signal efficiency due to detector effects is 4.13%. These are an increase on the ν_e inclusive value of 2.96%, largely because of the effects an additional π^+ selection has on the detector systematic uncertainties stated previously. The magnitudes of the total detector systematic uncertainties are significantly smaller than the data statistical error of approximately 17%.

4.8.2 Cross-section Model Systematic Uncertainties

A notable source of uncertainty comes from the model choices and parameters used in simulation, and their ability to accurately describe all of the physics undergone in the relevant interactions. Most noteworthy are parameters defining neutrino interactions, nuclear final state interactions and cross-section parameters. T2K estimates prior uncertainties on model parameters using external data constraints. A list of the cross section systematic uncertainties, provided by the T2K NIWG group [105], with their prior values and associated errors is shown in table 4.6. Detailed descriptions of all the cross-section systematic parameters can be found in [106, 107]. A brief overview of each systematic is given below:

- The axial mass term, M_A, for the axial form factor is implemented for both quasi-elastic and resonance interactions.

- The Fermi momentum, p_F, is the highest momentum state in Fermi gas models such as RFG. The Fermi momentum parameter has a dependence on the number of nucleons in the nucleus, therefore it is implemented for both Carbon and Oxygen targets.

- Two-particle two-hole effects, 2p2h, are contributions to the interaction cross section arising from multi-body processes. The contribution to 2p2h interactions can be split into three primary components: meson exchange current, MEC; nucleon-nucleus correlations; and the interference between the two.

- The binding energy, E_B, is implemented for CCQE interactions on both Carbon and Oxygen targets. There is currently no treatment of binding energy in resonance interactions in the latest oscillation analysis, and thus is not included for this analysis.

Cross Section Parameter	Prior Value and Error	NEUT	Units
M_A^{QE}	1.2 ± 0.41	1.2	GeV/c^2
M_A^{RES}	1.07 ± 0.15	0.95	GeV/c^2
p_F ^{12}C	223.0 ± 31.0	217	MeV/c
2p2h ^{12}C	1.0 ± 1.0	1.0	None
E_B ^{12}C	25.0 ± 9.0	25	MeV
p_F ^{16}O	225.0 ± 31.0	225	MeV/c
2p2h ^{16}O	1.0 ± 1.0	1.0	None
E_B ^{16}O	27.0 ± 9.0	27	MeV
2p2h Other	1.0 ± 1.0	1.0	None
C_A^5 (RES)	1.01 ± 0.12	1.01	None
Isospin $= \frac{1}{2}$ Background	0.96 ± 0.4	1.3	None
ν_e/ν_μ	1.0 ± 0.028	1.0	None
CC Coherent ^{12}C	1.0 ± 1.0	1.0	None
CC Coherent ^{16}O	1.0 ± 1.0	1.0	None
CC Other Shape	0.0 ± 0.4	0.0	None
NC Coherent	1.0 ± 0.3	1.0	None
NC Other	1.0 ± 0.3	1.0	None
FSI Inelastic Low Energy	0.0 ± 0.41	0.0	None
FSI Inelastic High Energy	0.0 ± 0.34	0.0	None
FSI Pion Production	0.0 ± 0.5	0.0	None
FSI Pion Absorption	0.0 ± 0.41	0.0	None
FSI Charge Exchange Low Energy	0.0 ± 0.57	0.0	None
FSI Charge Exchange High Energy	0.0 ± 0.28	0.0	None

Table 4.6: A list of cross section model systematic uncertainties, their respective prior values with expected range, and their initial values in NEUT nominal MC.

- Resonance interactions and their associated form factors introduce new parameters to cross-section models. The first is C_A^5 which affects the scale of the axial form factor at $Q^2 = 0$ GeV/c^2. The second is an isospin $\frac{1}{2}$ background scaling factor.

- The difference in ν_e and ν_μ cross-sections is another source of systematic error that is accounted for. The overall effect of this is approximately 3%, and is labelled in table 4.6 as ν_e/ν_μ.

- Remaining neutrino interactions not covered in fits to external data are characterised in the following errors:

  - Charged current coherent pion production carries a 100% error brought forward from similar motivation to the oscillation analysis, namely that the external data is consistent with no coherent production in this region of neutrino energy [106].
  - The energy shape dependence on other charged current interactions, such as: CC multi-π production, CC DIS, and CC0π resonant interactions that include γ, K, and η production.
  - Neutral current coherent pion production which has a 30% normalisation error from [108].
  - Other neutral current interactions which complements the CC other sample described previously. Poor constraints to external data means a recommended 30% error from [108] is used for this analysis.

- Final state interaction systematic uncertainties have the effect of migrating events between different observable detector topologies and change pion kinematics. For example, pion absorption in the nucleus can move events into CCQE-like samples. FSI uncertainties are broken down into 3 main categories: Inelastic, charge exchange, and pion absorption and production. Uncertainties on FSI parameters are estimated through pion-nuclear scattering data from fits to Carbon (most prominently from the DUET experiment [109]), to the cascade model parameters in NEUT [106].

Cross section model systematic uncertainties are evaluated using the T2KReWeight package, which produces splines for each model parameter over a 1σ standard deviation; each model parameter can affect both the shape and normalisation. The fractional error of each systematic uncertainty on the event yields and signal efficiency is evaluated over 250 toy experiments for each parameter. Either the event yields for a given topology, or signal efficiency are plotted, and the RMS computed as the fractional systematic uncertainty. For simplicity, background topologies are grouped into three categories: Photon background, which covers all background events originating from π^0 decays; ν_e CC background, which is defined as any charged

Systematic	γ Bkg (%)	ν_e CC Bkg (%)	Other Bkg (%)	Total Bkg (%)
M_A^{QE}	0.04	17.24	1.83	5.43
M_A^{RES}	2.87	4.58	3.04	3.39
p_F ^{12}C	0.00	0.13	0.01	0.04
2p2h ^{12}C	0.00	5.38	0.76	1.72
E_B ^{12}C	0.00	0.03	0.01	0.00
p_F ^{16}O	0.00	0.02	0.00	0.00
2p2h ^{16}O	0.00	0.52	0.00	0.15
E_B ^{16}O	0.00	0.00	0.00	0.00
2p2h Other	0.00	0.00	0.00	0.00
C_A^5 (RES)	1.01	2.03	1.58	1.43
Isospin $= \frac{1}{2}$ Background	0.71	1.64	1.07	1.06
ν_e/ν_μ	0.20	2.62	0.07	0.86
$\bar{\nu}_e/\bar{\nu}_\mu$	0.00	0.00	0.01	0.00
CC Coherent ^{12}C	0.14	0.00	2.23	0.59
CC Coherent ^{16}O	0.00	0.00	0.00	0.00
CC Other Shape	4.18	3.95	4.19	4.12
NC Coherent	0.00	0.00	0.00	0.00
NC Other	11.76	0.00	3.30	6.42
FSI Total	2.79	6.04	2.83	3.08
Total Uncertainty	6.31	5.81	1.80	10.76

Table 4.7: The effect of the cross section systematic uncertainties on the background event yields, separated by different topologies. The total systematic uncertainties are also shown taking into account each sample's relative contribution to the total background.

current ν_e event that isn't signal; and all other background, to contain any event that isn't included in the first two categories.

The fractional systematic uncertainties on background event yield topologies are shown in table 4.7. Each systematic uncertainty has been normalised to the relevant background topology sample size, as shown in table 4.5. Photon background systematic uncertainties are dominated by NC other, which is expected given the large contribution of neutral current interactions (figure 4.19a). The quasi-elastic axial mass term, M_A^{QE}, is the dominating systematic in ν_e charged current background. This is also significantly larger than the two other topology samples, but correlates with the relative CCQE contributions to each sample (figure 4.19b). The

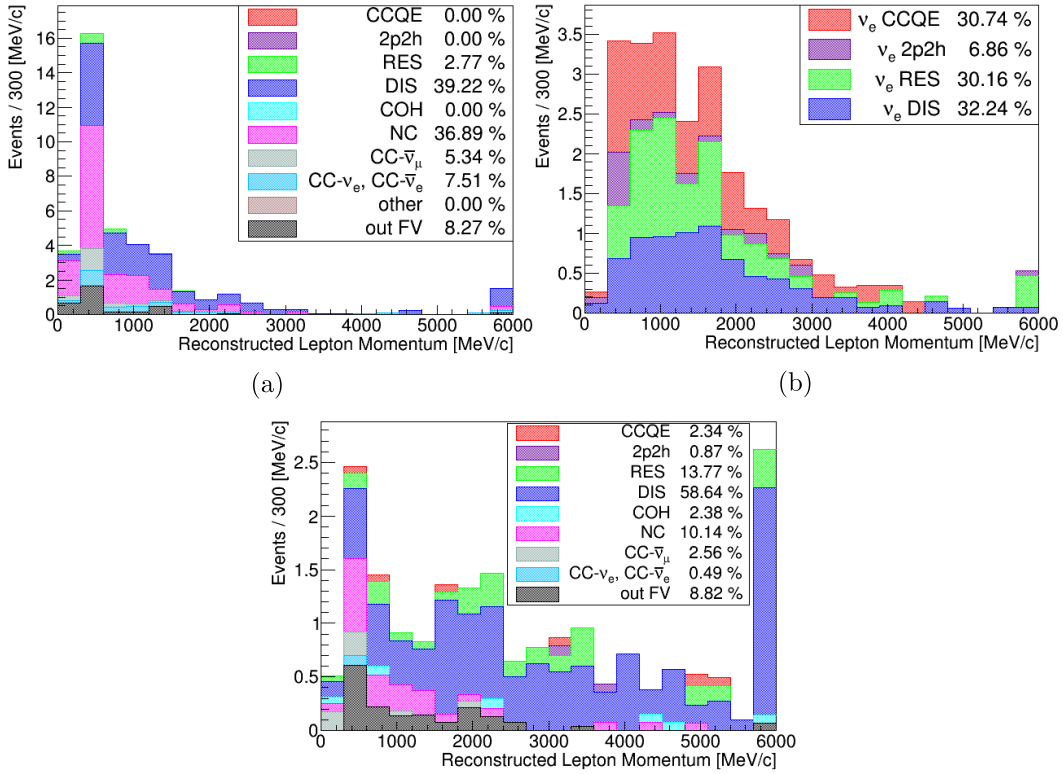

(a) (b) (c)

Figure 4.19: Number of events as a function of reconstructed lepton momenta, split into reaction types, for the three background topology samples: (a) Photon background, (b) ν_e CC background, and (c) All other background.

largest signal systematic in the ν_e inclusive analysis is M_A^{QE} at 8.52%. Given the ν_e background topology is closely related to the ν_e inclusive signal, except with lower statistics, the systematic values for M_A^{QE} in this analysis makes sense. A systematic of 5.38% is seen for 2p2h interactions on carbon in the ν_e CC background. This largely comes from uncertainties in meson exchange current parameters, and is most prominent in the ν_e CC background sample. Other large systematic contributions across all three topologies come from M_A^{RES}, CC other shape, and FSI. The relative resonance interaction contributions to all samples topologies can be seen in figure 4.19. As expected the size of the M_A^{RES} systematic correlates with the fraction of resonance interactions in the sample size. The relative large contribution to resonance interactions in the ν_e CC background originates from charged current ν_e π^0 production. The CC other shape systematic is dominated by the energy

Systematic	Fractional Error (%)	
	No Phase Space Cuts	Phase Space Limited
M_A^{QE}	0.37	0.13
M_A^{RES}	0.89	0.39
p_F ^{12}C	0.00	0.00
2p2h ^{12}C	0.03	0.02
E_B ^{12}C	0.00	0.00
p_F ^{16}O	0.00	0.00
2p2h ^{16}O	0.00	0.00
E_B ^{16}O	0.00	0.00
2p2h Other	0.00	0.00
C_A^5 (RES)	0.96	0.30
Isospin = $\frac{1}{2}$ Background	0.45	0.70
ν_e/ν_μ	0.00	0.00
$\bar{\nu}_e/\bar{\nu}_\mu$	0.00	0.00
CC Coherent ^{12}C	1.94	1.39
CC Coherent ^{16}O	0.13	0.09
CC Other Shape	0.73	0.99
NC Coherent	0.00	0.00
NC Other	0.00	0.00
FSI Total	1.33	1.70
Total	2.85	2.56

Table 4.8: The effect of cross section systematic uncertainties on the signal selection efficiency. Fractional errors are quoted before and after phase space constraints are applied.

shape dependence of DIS multi-pion interactions. Each systematic uncertainty has been qualitatively compared to the values quoted in the ν_e inclusive analysis in order to test their validity. The largest uncertainty contributions come from photon and ν_e CC background at 6.3% and 5.8% respectively, compared to 1.8% for other backgrounds. The full effect of cross section systematic uncertainties on the total background event yield is 10.76%; with the largest sources of systematic uncertainty coming from NC other and M_A^{QE}.

The systematic uncertainties on signal selection efficiency is shown in table 4.8. The different interaction type contributions to signal events are shown in figure 4.15a. A 4% presence of coherent events is large enough to influence the largest cross section systematic uncertainty on signal efficiency. This is likely due to the 100% error on the prior value in NEUT. There are also relatively large contributions from FSI, C_A^5 (RES), M_A^{RES}, and CC other shape which arise from the large presence of both resonance and DIS interactions in the signal sample. The total cross-section models systematic uncertainty on signal efficiency, as a fractional error, is calculated to be 2.85%. With the phase space constraints (defined in section 4.9.1) applied, the systematic uncertainty on signal efficiency is 2.56%.

4.8.3 Flux Systematic Uncertainties

A major uncertainty to any ND280 cross-section analysis is the modelling of the electron neutrino flux. The secondary beamline is simulated in order to estimate, in the absence of neutrino oscillations, the nominal neutrino flux at ND280. The FLUKA package [110, 111] is used to model primary beam proton interactions and the subsequent hadrons produced in the graphite target. Particles exiting the target are tracked using GEANT3 [112] simulation as they propagate through the magnetic horns and decay volume. GCALOR [113, 114] is used to model any hadron decays. These simulated predictions are bolstered by a significant flux monitoring program in which each beam pulse is measured in the primary neutrino beamline using the suite of detectors described in section 3.1.2. The beam position and width are measured by INGRID (section 3.3.1). Furthermore, data from the NA61/SHINE experiment [115], along with other experiments, taken at 31 GeV is used to improve the modelling of the kinematic distributions of meson from the proton-graphite collisions.

The uncertainties in neutrino flux predictions arise from a number of sources including but not limited to: the hadron production model, the proton beam profile, and the currents and alignments of the horns. The underlying parameters of each source of uncertainty are varied to evaluated their affect on neutrino flux binned in both neutrino energy and flavour. Flux tuning files, produced by the T2K beam group, are used to create event weights in Highland2 and propagate these flux systematic uncertainties through the analysis.

In this section two systematic errors associated with the flux will be discussed. The first is the error in the total predicted electron neutrino flux at ND280. The

	γ Bkg (%)	ν_e CC Bkg (%)	All Other Bkg (%)	Signal Efficiency (%)
Systematic Uncertainty	4.08	2.43	2.17	0.23

Table 4.9: The flux systematic uncertainty on different background topology event yields. Each background uncertainty is calculated relative to the topologies fractional contribution to the total background yield. The flux uncertainty effect on signal efficiency is also shown for a predefined limited phase space.

second is affect of flux uncertainties on event yield background topologies and signal efficiencies specific to this analysis.

Calculation of Total ν_e Flux at ND280

The total electron neutrino flux at ND280 is calculated using the flux tuning file and covariance matrix used in T2K oscillation analyses [116]. Correlated weights for each flux systematic source are generated using a covariance matrix provided by the T2K flux group. The weights are then applied to the tuned electron neutrino flux, and integrated to calculate the total flux. This procedure is repeated for 10,000 pseudo-experiments. Each pseudo-experiment represents the total flux for a given configuration of flux uncertainties. The mean of the distribution of calculated total fluxes is then used to evaluate the mean total flux and the RMS used to estimate the systematic uncertainty. Evaluating these parameters gives a total electron neutrino flux of $\Phi_{\nu_e} = (2.23 \pm 0.14)$ neutrinos/cm^2/10^{21} POT with an average electron neutrino energy of $< E_{\nu_e} > = 1.31$ GeV.

Effect of flux systematic uncertainties on event yields and signal efficiency

The flux systematic uncertainties are evaluated using the same covariance matrix used in the total flux calculation. The effects of flux systematic uncertainties on background event yields and signal efficiencies over 250 toys are shown in table 4.9. Combining the background topologies, the effect of flux systematic uncertainties on the total background event yield is 8.53%. The total flux systematic uncertainty on signal efficiency as a fractional error is before phase space constraints are applied is 1.11%. In the limited phase space defined in section 4.9.1, the flux systematic uncertainty on signal efficiency is 0.23%. Comparisons can be made to the flux systematic uncertainties calculated for the ν_e inclusive analysis: Here, the flux systematic uncertainties on background event yields and signal efficiencies were calculated to be 5.62% and 0.71% respectively [86].

4.9 Cross-Section Measurement

A cross-section measurement of the ν_e CC π^+ interaction on a carbon target, over one bin in kinematic space, has been made. This section will outline the choice of binning, phase-space constraints and the calculation made, before discussing the results in the context of nominal interaction model predictions.

4.9.1 Phase-Space Constraints

Constraints are applied to the analysis at this stage to define a region of kinematic phase-space in which the cross-section can be best measured. The signal was defined as ν_e CC π^+ events that pass all of the following constraints:

$$\begin{aligned} \cos\theta_\pi &> 0.5 \\ \cos\theta_e &> 0.707 \\ p_\pi &> 100 \text{ MeV/c} \\ p_e &> 300 \text{ MeV/c} \end{aligned}$$

The principal factors in choosing regions of phase-space to apply constraints are the selection efficiency and overall number of signal events in any particular bin. Kinematic constraints are applied to both the true lepton and most energetic pion tracks at the truth level. Constraints are applied to high angle events, $\theta > 45°$ for electrons and $\theta > 60°$ for pions, since the acceptance due to detector effects is essentially zero. Significant drops in signal efficiency and event yields are seen within these regions, and are shown in figure 4.20. The true lepton angular constraint is taken from the ν_e inclusive analysis and rejects events in the region $cos\theta < 0.707$. The pion angular constraints are defined by figures 4.20c and 4.20d. Events are rejected in the region of $\cos\theta < 0.5$ due to the significant decrease in both signal

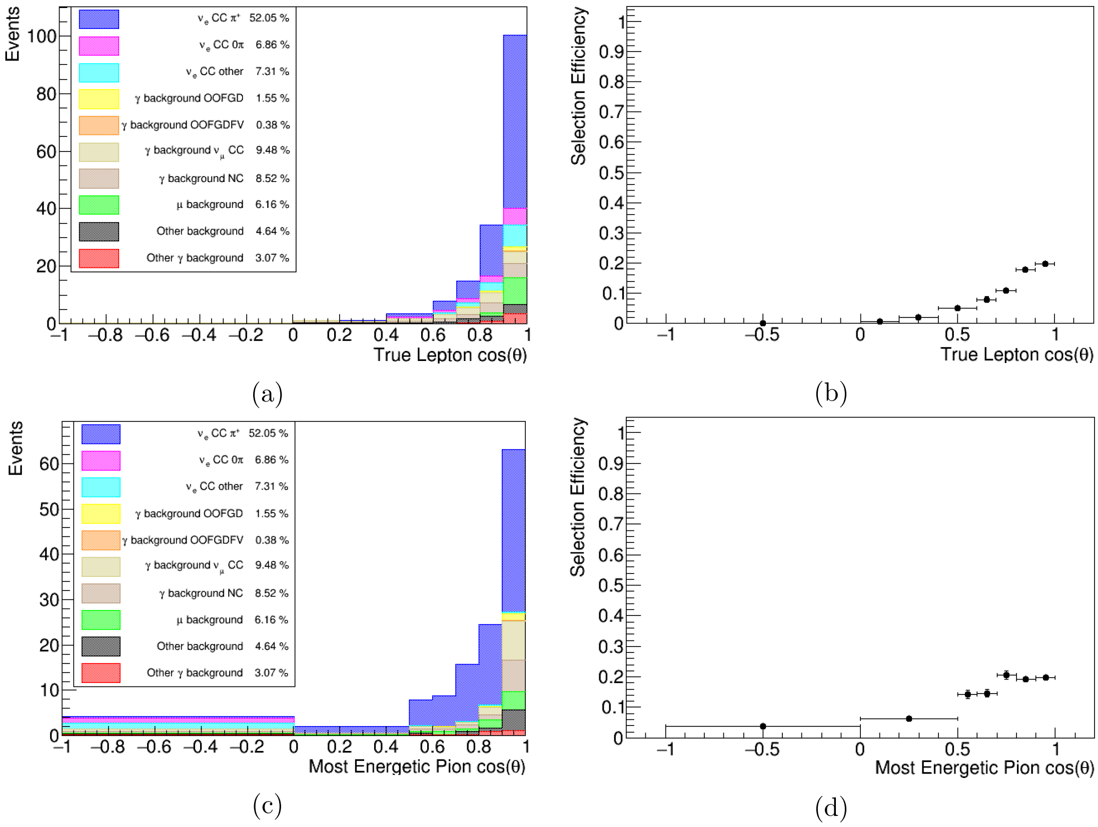

Figure 4.20: The angular kinematic phase-spaces for both the true lepton (top) and most energetic pion (bottom) tracks. The event yields are shown in (a) and (c), and the selection efficiencies are shown in (b) and (d). MC events are normalised to data POT.

event yield and efficiency. Backwards going most energetic pion tracks can occur when the pion candidate track selected at the reconstructed level, is not the most energetic pion in the event. This region has a negligible amount of signal events present, and is removed within the constraint.

Signal event yields in the background enriched low momenta bins are significantly smaller than across the rest of momenta space. Constraints are therefore applied to these regions also. Once again the post selection signal efficiencies and event yields, for both the true lepton and most energetic pion tracks, can be seen in figure 4.21. The signal contribution and selection efficiency at low lepton momenta is tiny, and thus a constraint is placed at $p > 300$ MeV/c. Moreover, a constraint of $p > 100$ MeV/c is used is placed on the most energetic pion track.

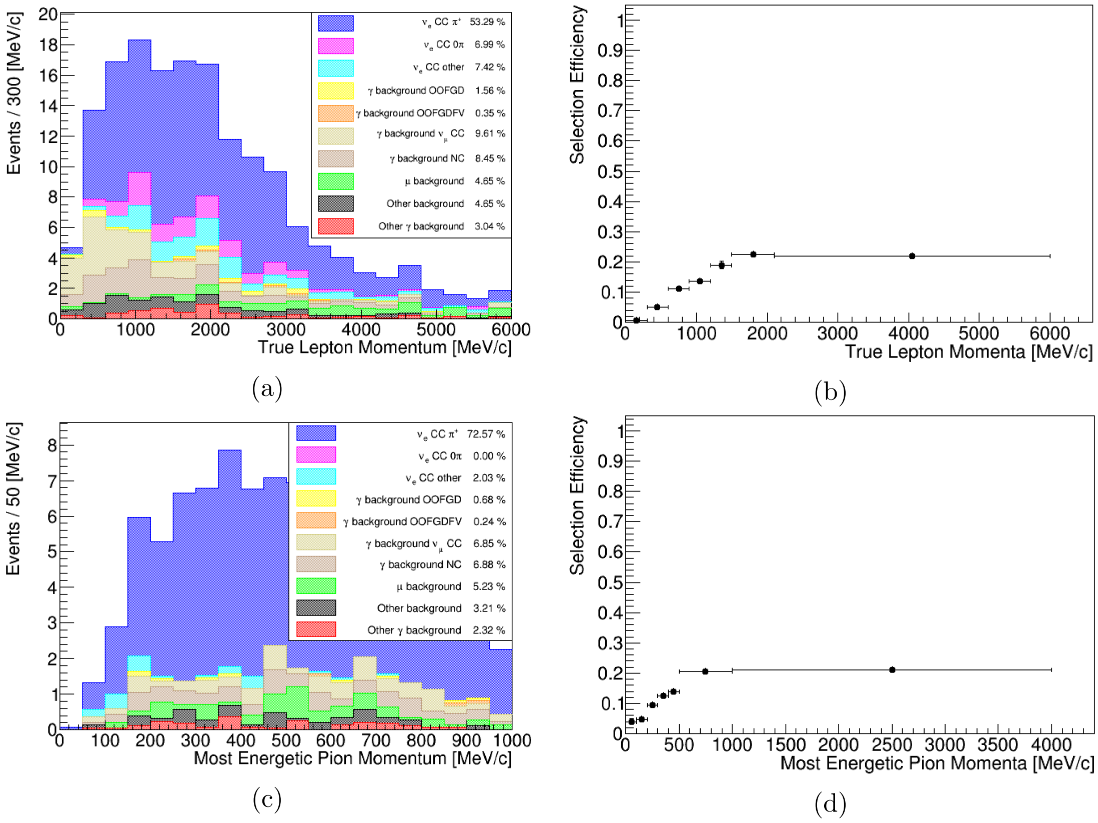

Figure 4.21: The momentum space for both true lepton (top), and most energetic pion (bottom) tracks. The event yields are shown in (a) and (c), and the signal efficiencies post selection are shown in (b) and (d). MC events are normalised to data POT.

4.9.2 Nominal NEUT Prediction and Validation

The MC used for this analysis is generated using NEUT D 5.4.0 (described further section 4.4). Cross-section predictions can be made independent of the analysis framework to contextualise and compare measured values with nominal MC. The predictions can also be used to validate the cross-section calculation methods to be used.

To obtain a prediction, the total number of predicted events must first be calculated. One million events were generated using NEUT version 5.4.0, and were uniformly randomly distributed between 50 MeV and 30 GeV. The simulated events modelled were all electron neutrino interactions on hydrocarbon targets. The highest momenta electron and most energetic positive pion are selected from the interaction.

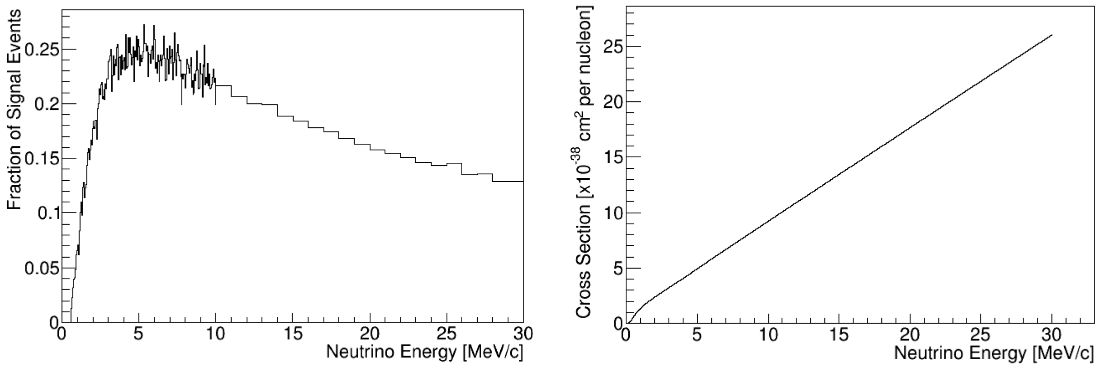

(a) (b)

Figure 4.22: (a) The fraction of ν_e CC π^+ events in the NEUT generated sample, and (b) the NEUT ν_e cross-section, both as a function of true incoming neutrino energy.

If no post final state interaction electrons or pions are present, the event is defined as background. For the event to be classed as signal, the selected electron and pion must pass further cuts, predefined by the phase-space constraints outlined in section 4.9.1. Events that do not pass the momentum and angular space cuts are put into the background category. The fraction of signal events, and interaction cross-section, both as a function of true neutrino energy are shown in figure 4.22. When multiplied together these plots yield the cross-section of signal events as a function of true neutrino energy. The binning for figure 4.22a is chosen by the fine binned flux MC predictions (shown in figure 4.23) provided by the T2K beam group [116]. A fine binning of 50 MeV is used up to 10 GeV, and then a courser binning of 1 GeV is used from then on. The same flux MC file, "tuned13av7", is used as in the total flux calculation in section 4.8.3. The predicted electron neutrino flux at ND280 as a function of neutrino energy is shown in figure 4.23. The cross section of signal events as a function of neutrino energy is combined with the simulated ν_e flux at ND280, to give a predicted number of signal events. A ratio of the integrated number of signal events against the total ν_e flux, as seen in equation 4.13, provides the predicted flux averaged cross section of signal events over one global bin in neutrino energy space.

$$\sigma = \frac{\int \sigma(E)\Phi(E)\,\mathrm{dE}}{\int \Phi(E)\,\mathrm{dE}} \tag{4.13}$$

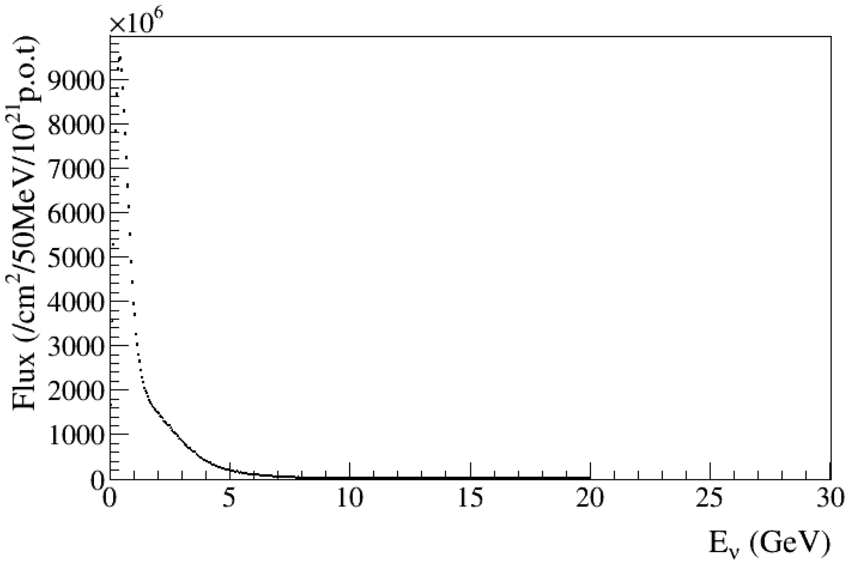

Figure 4.23: The predicted electron neutrino flux at ND280 as a function of neutrino energy.

Where σ is the flux averaged cross section prediction for some model, $\sigma(E)$ is the signal cross-section as a function neutrino energy, and $\Phi(E)$ is the electron neutrino flux as a function of neutrino energy. Applying equation 4.13 when using NEUT gives a predicted flux averaged cross section of $\sigma_{\text{NEUT}} = 2.22 \times 10^{-39}$ cm^2 per nucleon.

The same NEUT configuration used to calculate a flux averaged cross section prediction is also used to generate production 6T MC simulations. By parsing nominal NEUT ND280 MC in place of data through the calculation framework described in section 4.9.3, cross checks can be performed to validate both the calculation and the NEUT prediction, as the two methods should result in the same answer. ND280 MC when processed as data yields a cross section of $\sigma_{\text{ND280}} = (2.18 \pm 0.05) \times 10^{-39}$ cm^2 per nucleon. The error is taken from the 2.1% statistical uncertainty in ND280 MC events passing the phase-space constraints. The ratio of ND280 MC and NEUT prediction values suggest a difference of approximately 1.8%, and therefore agree within statistical error cross-validating each method.

Parameter	Source of Systematic Uncertainty				Total (%)
	Detector (%)	Cross Section Model (%)	Flux (%)	Other (%)	
S	6.08	10.76	8.53	-	15.02
ϵ	4.13	2.56	0.23	2.43	5.43
Φ_{ν_e}	-	-	6.08	-	6.08
T	-	-	-	0.72	0.72
σ	7.35	11.06	10.47	2.53	17.11

Table 4.10: A summary of each type of systematic uncertainty and its contribution to each parameter in the cross-section calculation (equation 4.14). Other systematic uncertainties originate in the calculation of the relevant parameter and are explained further in the text. All uncertainties are quoted as the fractional error.

4.9.3 Cross-Section Calculation

A total flux averaged cross-section measurement over one global bin in reconstructed neutrino energy space is calculated using equation 4.14.

$$\sigma = \frac{S}{\epsilon} \times \frac{1}{T\Phi_{\nu_e}} \tag{4.14}$$

Where S is number of signal events, ϵ is the signal efficiency, Φ_{ν_e} is the electron neutrino flux, and T is the number of target nucleons. The signal is calculated using $S = N - B_{MC}$, whereby N is the total number of data events and B_{MC} is the number of background events predicted by MC. The electron neutrino flux at ND280 is calculated to be $\Phi_{\nu_e} = (2.23 \pm 0.14)$ neutrinos/cm^2/10^{21} POT in section 4.8.3, with an average neutrino energy of $<E> =$ 1.31 GeV. The signal efficiency is taken as the post-selection signal efficiency after phase-space constraints are applied, and is calculated to be $(25.35 \pm 0.61)\%$, whereby the uncertainty is taken as the binomial error. The number of target nucleons, T, is calculated from the FGD1 fiducial mass of 919.5 kg, which corresponds to $(5.54 \pm 0.04) \times 10^{29}$ nucleons [88]. A full breakdown of the systematic uncertainty sources and their contributions to the parameters in the cross-section calculation is shown in table 4.10.

The calculation is performed using the 'xsCalculation' package in Highland2, purposely written in C++ for this analysis. The full production 6T FHC dataset outlined in section 4.4 is used, and the MC normalisation to data is performed on a

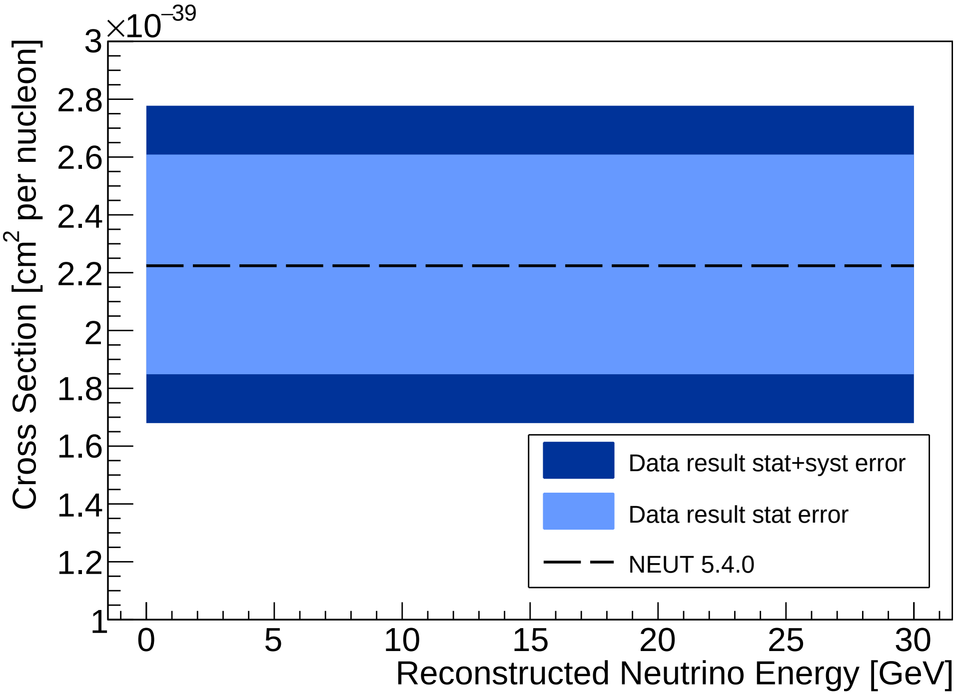

Figure 4.24: The flux integrated cross section prediction for nominal NEUT 5.4.0, compared to the data cross-section measurement in the context of systematic and statistical errors.

run-by-run basis. All systematic uncertainties calculated in section 4.8 are added in quadrature, and the statistical error in data is taken as $\sqrt{N}/S$. Statistical errors in MC are deemed to be negligible given the significantly large sample size. The total systematic and statistical errors are calculated to be approximately 17.11% and 17.70% respectively. The same phase space constraints introduced in section 4.9.1 are applied to the cross-section calculation. Through equation 4.14, the total ν_e CC π^+ cross-section, over an a reconstructed neutrino energy space of 0 GeV $\rightarrow$ 30 GeV, is calculated to be $\sigma = (2.23 \pm 0.39(\text{stat.}) \pm 0.38(\text{syst.})) \times 10^{-39}$ cm^2 per nucleon. This result provides the first preliminary ν_e CC π^+ cross-section measurement on a carbon target.

A comparison of the ν_e CC π^+ cross-section calculated from ND280 data to the NEUT 5.4.0 nominal prediction, provided in section 4.9.2, is displayed graphically in figure 4.24, and numerically in table 4.11. It can be seen that the nominal MC cross-section prediction lies within both ranges defined by the systematic and

Measured σ [10^{-39}cm^2 per nucleon]	Nominal Predicted σ [10^{-39}cm^2 per nucleon]	$<E>$ [GeV]
2.23 ± 0.39(stat.) $\pm\, 0.38$(syst.)	2.22	1.31

Table 4.11: A comparison of the measured ν_e CC π^+ cross section to the nominal prediction from section 4.9.2 using NEUT 5.4.0. The mean neutrino energy $<E>$ is also shown.

statistical uncertainties on the data measurement. Nevertheless, comparisons against different models including GENIE [117] and NuWro [118], as well as models with more sophisticated resonant pion production treatments, are needed before more complete conclusions on model performances can be made.

4.10 Super-Kamiokande Comparisons

Section 4.1 introduced an electron neutrino appearance study anomaly in the T2K oscillation analysis. A far detector excess is seen in the $\nu_e\pi^+$ FHC 1 decay electron sample. The probability of observing the 15 events seen in T2K's data samples, assuming maximal CP-violation, relative to a prediction of 7 events, is 6.9% for the best fit oscillation parameters. The analysis in this thesis provides the beginning of a direct constraint on this process using the near detector. A preliminary study of data-MC comparisons in a region of energy phase-space complimentary to the far detector studies, gives initial insights in any potential excess seen in the near detector. Two bins in reconstructed neutrino energy space have been defined. The low energy bin from $0 \rightarrow 1.25$ GeV replicates the region of energy space the Super-K $\nu_e\pi^+$ 1 decay electron sample is sensitive to. The high energy bin contains the remaining phase space ($1.25 \rightarrow 30$ GeV) used in the cross-section measurement above. Figure 4.25 shows the number of events for data and MC as a function of reconstructed neutrino energy for the low and high energy bins. The data-MC ratios are also provided in table 4.12. The Super-K analogous low energy bin shows the data and MC agree within data statistical error. This provides preliminary hints that the Super-K excess in this channel is a result of statistical fluctuation rather than a systematic excess

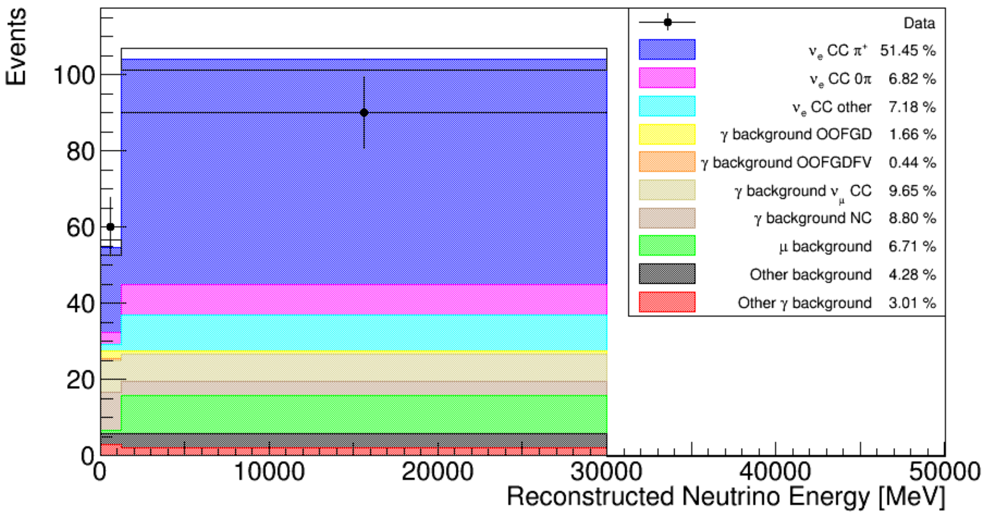

Figure 4.25: A data-MC comparison of the number of events split into two regions of reconstructed neutrino energy space. A threshold of 1.25 GeV is chosen to isolate a region of phase space that is comparable to SK. Detector systematic errors are displayed for the ND280 MC.

Energy Bin	Data	MC	Data-MC Ratio
$0.00 \rightarrow 1.25$ GeV	60 ± 8	54.6 ± 2.0	1.10 ± 0.15
$1.25 \rightarrow 30.0$ GeV	90 ± 10	104.1 ± 2.4	0.86 ± 0.10

Table 4.12: The number of data and MC events in the low and high bins of reconstructed neutrino energy space, the data-MC ratio is also shown. Error estimates on the data-MC ratios have been provided using the statistical error in data, and the detector systematic uncertainties in MC.

The far detector 1 decay electron sample was designed to add an additional ν_e CC $1\pi^+$ channel, increasing the number of signal events in ν_e appearance studies for the oscillation analysis. The selection takes one electron-like ring fully contained in the detector fiducial volume with a visible energy above 100 MeV. Further cuts dictate there must be exactly one decay electron, and the reconstructed neutrino energy, calculated using the same CCΔ picture used in the near detector sample, must be less that 1.25 GeV. The final selection cut is used to reject neutral pions.

When building a near detector constraint, comparative similarities and differences between the near and far detector samples should be discussed. An investigation into the number of π^0 particles present in the ND280 signal sample can be seen in the appendix figure A.3. The far detector has the ability to veto π^0 interactions through unique signals. Therefore the likeness of the ND280 signal to the far detector sample, in the region of momenta space comparable to SK, can be tested through the amount of π^0 present. Studies show approximately 85% of signal events are absent of neutral pions; consequently at least one π^0 exists in roughly 15% of events and are topologically different to the 1 decay electron sample in the far detector. Moreover, the far detector sample has 4π angular coverage, whereas the near detector sample is more constrained to the forward going regions of angular phase space.

This study provides only only a preliminary insight into potential data-MC discrepancies, effects such as event migration across bin thresholds have not yet been considered. A more complete analysis, with further investigations into topology likeness, is needed to constrain any Super-K results using ND280 data.

Chapter 5

Hyper-Kamiokande

Hyper-Kamiokande (HK) [119] is a next generation water Cherenkov neutrino detector that follows on from Kamiokande and Super-Kamiokande. Significantly larger than it's predecessors, Hyper-Kamiokande will be the largest neutrino detector in the world. HK will serve as the far detector in the long baseline neutrino experiment that will eventually supersede T2K. Unless otherwise stated, it may be assumed that the main reference for this chapter is the Hyper-Kamiokande Design Report (2018) [119].

5.1 Physics Goals

The physics goals of Hyper-Kamiokande are split into three main areas:

- Neutrino oscillations
- Nucleon decay searches
- Astrophysical observations

Neutrino oscillations can then further be divided into measuring the magnitude of CP-violation in neutrino oscillations, the determination of normal or inverted mass hierarchy, and precision measurements of known oscillation parameters. Hyper-K aims to measure neutrino oscillation parameters through two neutrino sources. Observing both atmospheric neutrinos and long baseline neutrinos provides complementary information. Assuming a total of 2.7×10^{22} POT with a beam power of 30 GeV, Hyper-K is expected to be able to determine the leptonic CP violating phase, δ_{CP}, to better than 23 degrees for all possible values of δ_{CP}. Furthermore CP-violation could be established with a statistical significance of more than 3σ (5σ) for 76% (57%) of δ_{CP} parameter space. Currently there has not been an extensive study on the ability for measurements on the sign of Δm^2_{32} or Δm^2_{32} for mass hierarchy determination. It is predicted at the time Hyper-K becomes operational, the mass hierarchy could be determined to up to $\sim 4\sigma$ thanks to a combination of data from T2K and NOvA; and future reactor experiments such as RENO-50 [120], JUNO [121], ICAL [122], PINGU [123], and ORCA [124].

The decay of protons and bound nucleons are direct observable consequences of the violation of baryon number; a process believed to have an important role during the formation of the early universe. Furthermore baryon number violation is predicted in many Grand Unified Theories (GUTs) which allow transitions from quarks to leptons and vice versa. These GUTs predict the lifetime of the proton to be greater than 10^{30} years, so new experiments must be sensitive to this vast lifetime. Figure 5.1 demonstrates the future capabilities of Hyper-K in the 90% CL lifetime limits, in comparison with a number of GUTs. After 10 years of operation Hyper-K is sensitive to lifetimes that are predicted by a number of GUTs, through both $p \rightarrow e^+ \pi^0$ as well as channels involving kaons.

Hyper-K has the ability to set the energy threshold for detection to as low as several MeV; this enables event-by-event detection and reconstruction of astrophysical neutrinos from sources such as the sun, and supernovae. Using solar neutrinos and higher precision terrestrial matter effect [125, 126] measurements, Hyper-K aims to better understand neutrino oscillation behaviour in the presence of matter. Terrestrial matter effects hint at the use of atmospheric and long baseline neutrino experiments to measure CP-violation and mass hierarchy, as both of these parameters affect neutrino oscillation probabilities. Moreover, Hyper-K could feasibly help to resolve a current $\sim 2\sigma$ tension between the best fit values of Δm^2_{21} in solar and reactor neutrino experiments; current predictions suggest that the discrepancy is due to solar neutrino interactions on matter.

An important astrophysical source of neutrinos is core collapse supernovae.

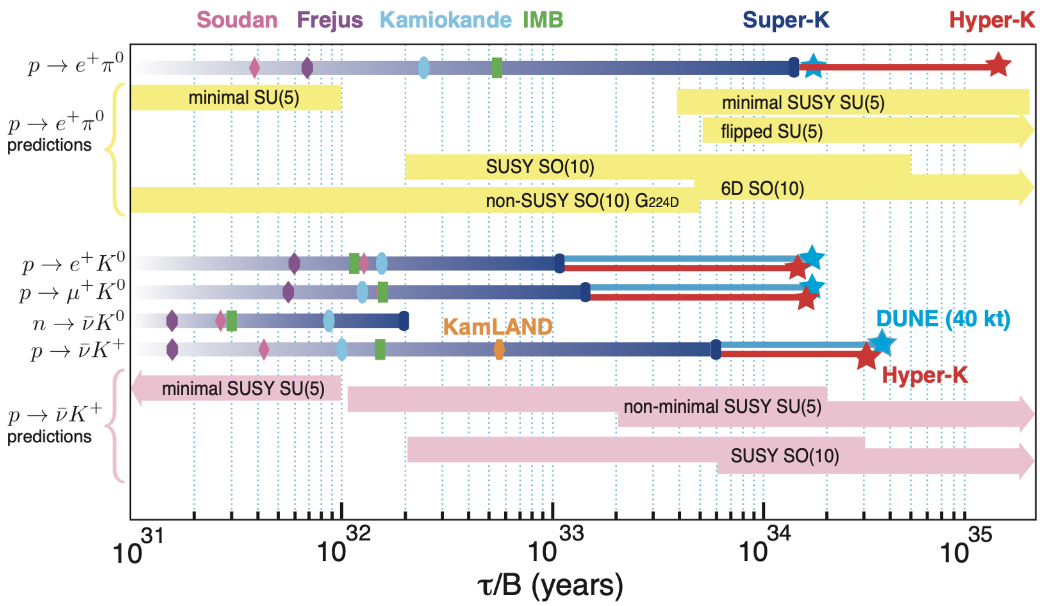

Figure 5.1: A comparison of the theoretically predicted rate of nucleon decay for a number of key modes, and the historical limitations for various experiments. The projected limits fo Hyper-K and DUNE are based on 10 years of running. Figure taken from [119].

It is anticipated that if a supernova took place near the centre of our galaxy, Hyper-K would observe $O(10^4)$ neutrinos in a time frame of approximately 1 second (a calculation described in detail in [119]). Furthermore, the large volume of Hyper-K increases its sensitivity to distant supernova $O(\text{Mpc})$ away. Hyper-K also has the ability to precisely determine the arrival time of such neutrinos. Analyses from core collapse supernova neutrinos can provide information not only about supernova mechanics, but comparisons of ν_e and $\bar{\nu}_e$ flux during the neutronization burst can yield information on neutrino mass hierarchy. Hyper-K can also study other astrophysical processes, including dark matter and the detection of neutrinos through solar flares [119].

5.2 Beam

The neutrino beam to be supplied to Hyper-Kamiokande will be an upgraded version of J-PARCs beam [127], currently being used for T2K (see section 3.1.2). As

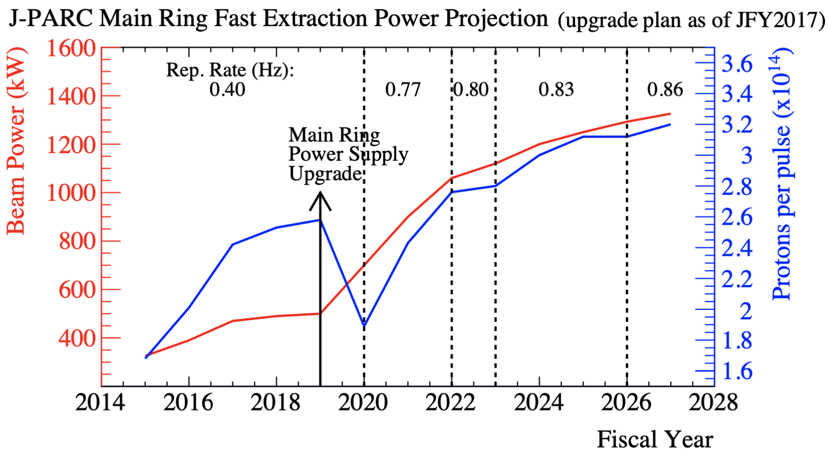

Figure 5.2: The projected main ring performance in fast extraction mode up to the year 2028. The protons-per-pulse, beam power and repetition rate are shown. Figure taken from [119].

of 2018 a beam intensity of 2.45×10^{14} protons-per-pulse (ppp), corresponding to $\sim$ 485 kW of beam power, has been achieved in the main ring fast extraction mode operation [119]. A number of short term [128], and longer term [129, 130], upgrades are planned for J-PARCs accelerator chain; starting within the next couple of years and continuing throughout HKs construction and data-taking periods. The projected beam performance up to 2028 is shown in figure 5.2. High intensity studies of current accelerator performance suggest a beam power of 1-1.3 MW can be achieved post beam upgrades. Conceptual design studies are also in progress for operation at beam powers greater than 2 MW [131]. The approaches being considered include enlarging the main ring (MR) aperture, raising the rapid cycling synchrotron (RCS) top energy, or the insertion of an emittance-damping ring between the MR and RCS.

5.3 Near Detector Complex

Like T2K, Hyper-K will require a suite of near detectors to measure signal and background processes relevant for neutrino oscillations. Event rates at Hyper-K will be predicted through extrapolations from measured event rates at the near detector. Maximising systematic cancellations when extrapolating is desirable so use of the same target nuclei as used in the far detector, and enhanced angular acceptance is

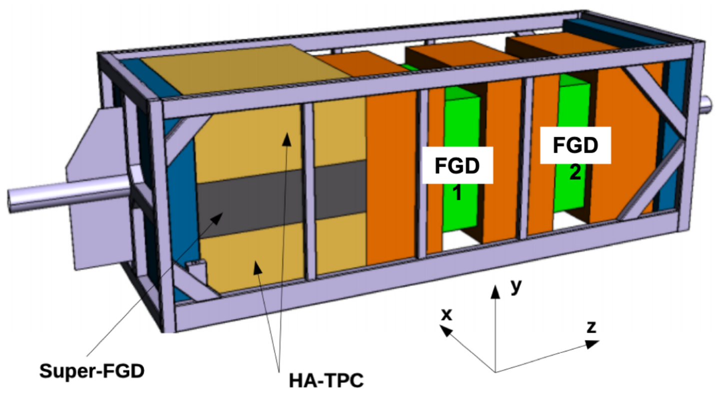

Figure 5.3: CAD model of the proposed ND280 detector post-upgrades. The upstream segment of the detector now consists of two High-Angle TPCs (brown) with a scintillator detector Super-FGD (grey) intersecting them. The beam and magnetic field are orientated approximately parallel to the z and x axis respectively. The two FGD sub detectors present in the current status of ND280 are also labelled for context. Figure edited from [132].

required.

5.3.1 ND280 Upgrade

Hyper-K will use an upgraded version of T2Ks ND280 detector complex previously described in section 3.3. An official T2K project since 2017, the ND280 hardware upgrade [57] has a goal of reducing the total systematic uncertainties on neutrino event rate extrapolation to the far detector to better than 4%. The design aims to improve the acceptance of high angle or backwards-going particles. This is achieved through the addition of a new scintillator target detector rotated parallel to the neutrino beam direction. Sandwiching the target detector with two horizontal High-Angle TPCs (HA-TPC) achieves almost full 4π angular acceptance. These three sub-detectors will be situated upstream of the tracker, replacing the current pi-zero detector. A schematic diagram of ND280 post-upgrade is shown in figure 5.3.

The ND280 upgrade keeps the current tracker and surrounding ECal modules. The P0D detector, seen in figure 3.6, is to be replaced but the upstream and P0D ECals will be kept to veto entering muons and photos from interactions in the

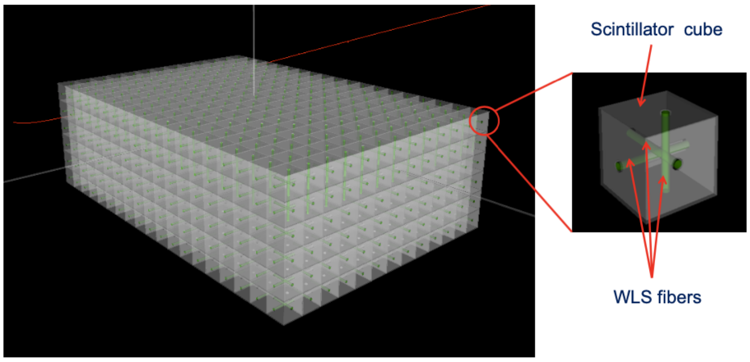

Figure 5.4: A schematic concept of the design of Super-FGD, demonstrating the composition of each scintillator cube and WLS fibres. Taken from [132].

sand around the detector. The 2 m long horizontal High-Angle Time Projection Chambers (HA-TPC) aim to replicate the high performance of the existing TPCs inside ND280. This requirement ensures key features such as: 3D reconstruction, particle identification, charge and momentum measurements are retained. Between the HA-TPCs, Super-FGD will provide a new high resolution 3D scintillator detector. Conceptual aims of Super-FGD were to provide a sufficiently large target mass, the acceptance of high-angles charged leptons, and the ability to identify and reconstruct short tracks of low energy hadrons near the interaction vertex. Super-FGD is composed of mall plastic scintillator cubes read out by three orthogonal wavelength shifting (WLS) fibres. A concept diagram of Super-FGD can be seen in figure 5.4. The size of each cube is $1 \times 1 \times 1$ cm^3. The total number of cubes in the baseline design is 2,064,384 arranged in a $192 \times 192 \times 56$ fashion, and 58,368 channels respectively. Every WLS fibre terminates at a Multi-Pixel Photon Counter (MPPC) to readout channels for each plane.

In addition, surrounding the new horizontal tracker will be six thin Time-of-Flight (TOF) scintillator layers. The goal with the new TOF system is to improve reconstruction of backward-going tracks. Studies are currently undergoing to understand the impact of TOF on particle identification.

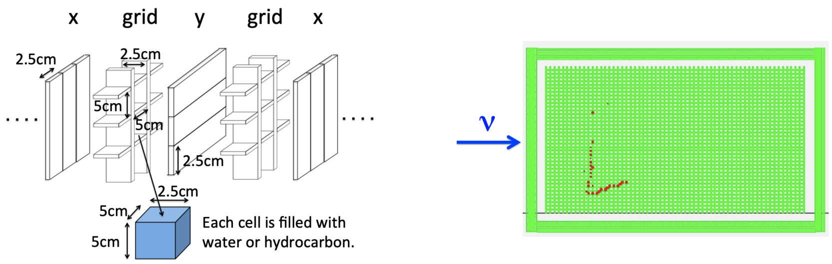

Figure 5.5: Left: A schematic representation of the plastic scintillator bars arrangement inside of WAGASCI. Right: A monte-carlo event display of a charged current neutrino interaction in WAGASCI. Figures taken from [119].

5.3.2 WAGASCI

Another detector being considered for the ND280 upgrade is WAGASCI (Water Grid And SCIntillator detector). The concept of WAGASCI is to develop a target detector, filled primarily with water, to measure neutrino interactions with high precision and large angular acceptance. Particles can be tracked across the full 4π solid angle using scintillator bars are arranged into a 3D grid like structure. The remaining voids created are defined as cells that can be filled with either water or hydrocarbon, changing the neutrino target medium. Figure 5.5 demonstrates both the conceptual design, and tracking of charged current interactions through simulation. WAGASCI modules are first being installed and tested at the J-PARC near detector hall, surrounded by muon detectors [133]. The test experiment will aim to measure the cross sections on both water and hydrocarbon targets, and has been approved by J-PARC PAC as test experiment T59 [134]. The INGRID detector has previously established the technique of comparing the interaction rates on the two targets to measure an inclusive water to hydrocarbon charged current cross section ratio [135]. WAGASCI, as experiment T59, aims to measure the ratio to a precision of 3% or better.

The proposed target mass of ND280 is expected to roughly double after the upgrades. Since the neutrino event rate is proportional to the target mass, it is also expected that the event rate will approximately double post-upgrade. A simplified MC study, without full event reconstruction, has been used to predict the number of neutrino events pre and post ND280 upgrade. The results of this study can be seen

		Number of Selected Events		
Detector Configuration	Target Mass (ton)	CC-ν_μ (ν) beam	CC-$\bar{\nu}_\mu$ ($\bar{\nu}$ beam)	CC-ν_μ ($\bar{\nu}$ beam)
Current ND280	2.2	95,860	27,433	14,862
ND280 Upgrade	4.3	199,775	54,249	28,370

Table 5.1: A comparison of the predicted number of neutrino events for the current ND280 and ND280 upgrade target mass respectively. The predictions correspond to 1×10^{21} POT. Table adapted from [119]
.

in table 5.1.

5.3.3 High Pressure Time Projection Chamber

Longer term ND280 upgrades could have the potential of introducing high pressure gas time projection chambers (HPTPC). Advantages of using HPTPC detectors are that they provide detailed vertex resolution, good particle identification, full angular coverage, and sensitivity to low momenta protons. The HPTPCs are proposed to replace the current TPCs. ND280 would be able to contain HPTPCs of size 8 m^3 under 10 bar of pressure. HPTPCs, using a gas target, have the strength that the target medium is interchangeable; a wide of successful gas mixtures having already been used in ND280 to test different nuclear model components. Furthermore, a gas HPTPC would yield a relatively pure ν_e sample. This is because of the reduction in photon background prominent in current ND280 ν_e-CC analyses, analogous to that described in chapter 4.

5.4 Intermediate Water Cherenkov Detector

To better constrain systematic uncertainties, Hyper-K will also house a new intermediate water Cherenkov detector (IWCD) [136]. The physics motivation for the detector is to constrain the cross section on water directly, with the same solid angle acceptance as Hyper-K thereby eradicating the need for a subtraction analysis. Water Cherenkov detectors also have the capability of detecting pure ν_μ-CC, ν_e-CC and NCπ^0 samples due to their excellent particle identification capabilities. Moreover, background rates in nucleon decay searches such as CCπ^0 and kaon production from

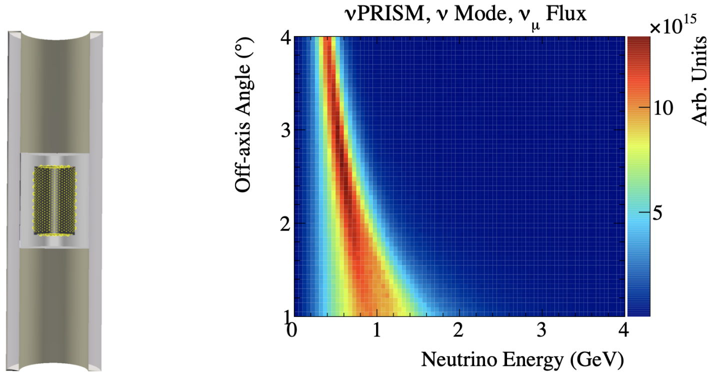

Figure 5.6: (Left) A diagram demonstrating the conceptual design for NuPRISM. (Right) The ν_μ flux energy dependence shown as a function of off-axis angle between 1° - 4°. Figure taken from [119]

.

neutrino interactions can be measured [119]. The IWCD's measurements, in tandem with ND280's magnetised tracking abilities, are essential to lowering the systematic uncertainties needed to achieved Hyper-K's physics goals. To contain enough muons up to the momentum region of interest to the far detector, the IWCD must be large enough in size. Furthermore the IWCD must be far enough from the neutrino production point to minimise pile-up of interactions in the same timing bunch. These parameters constrain the detector to be of kilotons in size, and approximately 1-2 km from neutrino beam production point at J-PARC [136].

Following on from the conceptual design of NuPRISM [137], one design for IWCD consists of a detector orientated with it's cylindrical polar axis in the vertical direction. A feature being considered for IWCD is to span over a range of off-axis angles to measure the final state leptonic response over numerous neutrino spectra peaked at different energies. NuPRISM design featured a 10 m tall inner-detector located 1 km downstream from J-PARC. A crane system enables the detector to be moved vertically inside of a 50 m pit to yield an off-axis angular range between 1° - 4° which the detector can traverse. NuPRISM's inner-detector design holds 3215 8 inch inward facing PMTs giving a photo-coverage of approximately 40%. A conceptual drawing of the NuPRISM detector alongside the ν_μ flux dependence on off-axis angle is shown in figure 5.6. There are three primary reasons why the IWCD would want to probe a range of off-axis angles. The first is to eliminate model dependent uncertainties in the near to far extrapolations which arise from differing flux at near and far detectors due to oscillations, and poorly understood nuclear effects in final state lepton kinematics as a function of neutrino energy [137]. Secondly, the fraction of intrinsic electron (anti)neutrinos increases as a function of off-axis angle. With an increase in purity at high off-axis angles, measurements of electron (anti)neutrino cross sections relative to muon (anti)neutrino cross sections can be achieved with higher precision. Measurements of $\sigma_{\nu_e}/\sigma_{\nu_\mu}$ have the potential to be made with 3% precision. This level will decrease for their anti particle counterparts given the larger NC background in the $\bar{\nu}_e$ sample and more prominent wrong-sign background for both $\bar{\nu}_e$-CC and $\bar{\nu}_\mu$-CC interactions. Thirdly, at 1 km baseline the neutrino spectrum peak varies from 1.1 km/GeV to 2.5 km/GeV between 1° - 4° respectively. Within this region it is possible to search from sterile neutrino induced oscillations consistent with the LSND [21, 138] and MiniBooNE [139, 140] ν_e and $\bar{\nu}_e$ appearance anomalies described in section 2.1.2. The IWCD can search for the oscillation pattern not only through reconstructed energy but also via reconstructed off-axis angle given the neutrino spectrum has a dependence on it. Preliminary studies hint that much of the LSND allowed region can be excluded at 5σ [137, 141].

Further design concepts for the IWCD includes the possibility of using gadolinium (Gd) doping [142] to exploit neutron tagging. Gd doping in water Cherenkov detectors is one way of enhancing neutrino and antineutrino separation sensitivity through the detections of neutrons in the final state, or protons in the case of using Water-based Liquid Scintillator (WbLS) compounds [143]. Combined with IWCD 4π detector coverage, statistical separation of primary interaction nodes becomes possible [144]. Neutron tagging allows final state interaction effects within different interaction models to be probed in more detail. Moreover, it provides charge separation information through the enhanced presence of final state neutrons for $\bar{\nu}$-CC interactions. This provides a constraint on wrong-sign backgrounds and allows comparisons of neutrino and antineutrino cross-section measurements on water. These factors reduce critical systematic uncertainties on atmospheric neutrino oscillation and beam δ_{CP} analyses. Simulations of neutron tagging have been performed

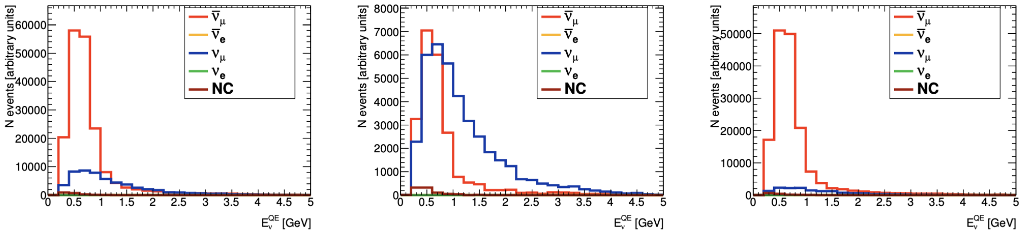

Figure 5.7: The composition of the one muon-like ring sample for the TITUS detector during antineutrino mode running. The effect of different neutron selections is shown. From left to right, before neutron tagging, no tagged neutron, at least one tagged neutron. Figure taken from [145].

using the TITUS concept detector. TITUS [145] was originally proposed to be an intermediate detector for Hyper-K with neutron tagging capabilities. Simulations demonstrated in figure 5.7 suggested the selection purity of $\bar{\nu}$CCQE interactions increases significantly when selection at least one neutron.

In principal, it is possible to combine the two techniques described above using Gd loading inside an off-axis spanning detector. Nevertheless, it should be noted that a Gd loaded detector must be sufficiently far from the neutrino beam origin to limit the beam induced entering neutron background. However, the further downstream, the larger the excavated volume needed for an off-axis spanning detector. Preliminary studies suggest the entering neutron rate is low enough for the off-axis spanning detector located 1km downstream from the neutrino production point [119].

The IWCD can also be used as a supernova alarm, independent of the far detector. Additionally with Gd doping capabilities, neutrino type discrimination would be possible in the event of a supernova in the local galaxy.

5.5 Far Detector

The Hyper-Kamiokande far detector is the next generation water Cherenkov detector following Super-Kamiokande. The candidate site for Hyper-K is located 8 km south of Super-K, in the Tochibora mine near Kamioka town, Japan. Lying 650 m underground, the detector will be situated under the peak of Nijuugo-yama, corresponding to approximately 1,750 m.w.e. The cavern has been designed to view the same 2.5°

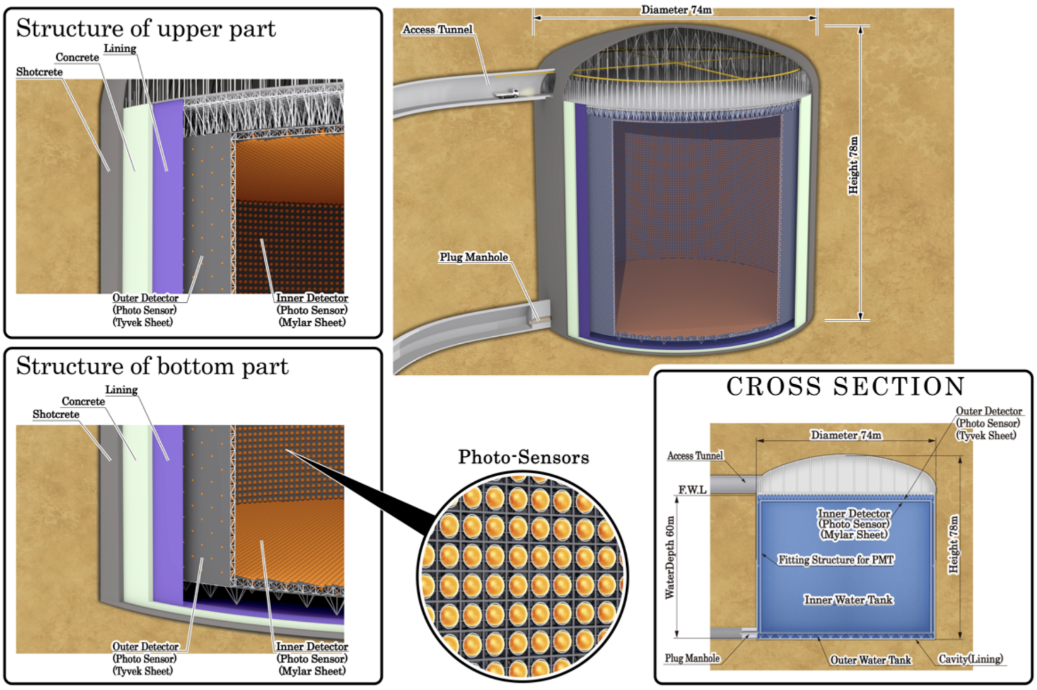

Figure 5.8: Schematic view demonstrating the 1TankHD design for the Hyper-K far detector. The multiple diagrams demonstrate different sections of the detector. Taken from [119].

off-axis angle that Super-K currently has with J-PARC.

The Hyper-K far detector design is a one vertical cylindrical water tank with 40% photo-coverage. In accordance with the latest Hyper-K design report [119], this tank design will be referred to as 1TankHD throughout this thesis. A schematic view of the detector is shown in figure 5.8. The tank design is 60 m in height with a 74 m diameter, giving it a fiducial volume eight times larger than Super-K. This would also make Hyper-K the largest water Cherenkov experiment to have ever existed. A summary of the key parameters of the 1TankHD design relative to it's predecessors, Super-K and KAM, is shown in table 5.2. The measurement technique of Hyper-K is analogous to Super-K, employing ring-imaging water Cherenkov techniques to measure neurtino interactions, and possible nucleon decays. To determine CP-violation within a few % accuracy, it is estimated that $O(10^3)$ electron neutrino signal events are needed to be accumulated from the J-PARC beam [119]. This equates to a fiducial mass of $O(10^2)$ kton. Furthermore, with $O(10^{35})$ nucleons contained in

	KAM	Super-K	Hyper-K
Depth	1,000 m	1,000 m	650 m
Tank Diameter	15.6 m ϕ	39 m ϕ	74 m ϕ
Tank Height	16 m	42 m	60 m
Total Volume	4.5 kton	50 kton	258 kton
Fiducial Volume	0.68 kton	22.5 kton	187 kton
Inner Detector (ID) PMTs	948 (50 cm ϕ)	11,129 (50 cm ϕ)	40,000 (50 cm ϕ)
Outer Detector (OD) PMTs	123 (50 cm ϕ)	1,885 (20 cm ϕ)	6,700 (20 cm ϕ)
Photo-sensor Coverage	20%	40%	40%
OD Thickness	$\sim$ 1.5 m	$\sim$ 2 m	1 $\sim$ 2 m
Single-photon Detection Efficiency (ID)	unknown	12%	24 %
Single-photon Timing Resolution (ID)	$\sim$ 2 nsec	2-3 nsec	1 nsec

Table 5.2: A summary table demonstrating the key parameters of the Hyper-K 1TankHD design with a comparison to it's predecessors. Figures for the past KAM [146, 147] and present Super-K [148, 149] experiments have been taken for KAM-II and SK-IV respectively. The single photon detection efficiency is taken as a product of the quantum-efficiency peak at 400 nm, photo-electron efficiency, and threshold efficiency. Table has been adapted from [119].

this mass of water a sensitivity to nucleon lifetime of 10^{35} years is possible.

The neutrino target medium for tank will be highly transparent ultra-purified water. Hyper-K will adopt the current Super-K water system designs, ensuring the attenuation length for 400 nm-500 nm photons is above 100 m, and a radon concentration level below 1 mBq/m^3. For Hyper-K this requires water to be processed at a rate of 310 tons/hour, and 50 Nm^3 of radon free air to be generated every hour. Depending on the success of the recent addition of gadolinium sulfate to Super-K, the option to Gd-load Hyper-K is available. Therefore, the design criterion for Hyper-K must be adaptable for this possibility (an important note for chapter 6).

Part of the design specification for Hyper-K is the need for single photon sensitivity. This enables reconstruction of the spatial and timing distributions of the Cherenkov photons which are emitted through neutrino interactions and nucleon decay. Hyper-K will use newly developed ultrasensitive PMTs (Hamamatsu R12860), with higher-efficiency and higher-resolution than those currently used in Super-K (Hamamatsu R3600). This upgrade will amplify faint signatures, enhancing the sensitivity to clean proton decay searches via $p \rightarrow e^+ + \pi^0$ and $p \rightarrow \bar{\nu} + K^+$ decay modes. Increased sensitivity to neutron signatures will also benefit the observation of electron anti-neutrinos from supernovae. As seen in table 5.2, the diameter of Hyper-Ks inner-detector and outer-detector are 50 cm and 20 cm respectively; the photo-coverage for the inner-detector and outer detector photomultipliers will be 40%.

As well as the 1TankHD design, the possibility of and additional second tank (2TankHK-staged) is also being considered. The second detector would be stationed downstream of the first. A possible location being considered is around Mount Hakamagoshi, lying at a baseline of 335 km and an off-axis angle of 2.4$\circ$. Due to the magnitude of Mount Hakamagoshi's elevation (1,159 m), the second detector have greater sensitivity to low energy neutrinos such as those from supernovae and the sun.

As of February 2020, the Hyper-Kamiokande project has been officially approved [150]. Construction is due to begin in April 2020, and operations will proceed from 2027.

Chapter 6

Optical Calibration

A new generation of neutrino detectors is fast approaching. Water Cherenkov detectors, such as the large scale Hyper-Kamiokande detector with over 40,000 photo-sensors, need to include optical calibration systems to monitor the properties of the water, and operation of the photosensors. The Hyper-Kamiokande physics goals dictate that the detector must be understood to the level of a few percent which can only be achieved through careful calibration.

This chapter will outline the proposed optical calibration system for the Hyper-Kamiokande experiment with a primary focus on the light injection system developed in the UK. In particular, the research and development of optical diffuser based technologies will be discussed in detail. Diffuser results are shown both in the context of laboratory experiments at the University of Warwick, as well as deployments inside the Super-Kamiokande detector. Later, a discussion of the future of optical diffuser research and development is provided, following the information gained from previous deployments.

6.1 Proposed Hyper-Kamiokande Optical Calibration System

The Hyper-Kamiokande detector, described in section 5.5, will be the largest water Cherenkov neutrino detector in the world. The technical design of Hyper-K features an inner and outer detector, containing 40,000 50 cm and 6,700 20 cm diameter

PMTs respectively. Both inner and outer detectors need optical calibration systems. The calibration system will be an extension of the successful Super-K system, using several calibration techniques established over two decades of operation. This section will outline the proposed optical calibration systems for the Hyper-K detector, with a focus on the light injection system under development by the Hyper-K UK collaboration.

6.1.1 Light Injection System

For water Cherenkov detectors such as Super-K and Hyper-K, it's important to understand the response of the photo-sensors used. The light injection system aims to measure timing, gain and multi-photon responses of the inner detector PMTs. In addition, of particular importance to large scale detectors such as Hyper-K, is to understand properties of the medium, such as absorption lengths and photon scattering probabilities as a function of depth. These are the primary measurements the light injection system aims to cover.

As in Super-K, the optical calibration system consists of multiple light injection points around the detector. Pulses of light will be controlled electronically at the top of the tank and fed through optical fibres to the injection points. Two different sources of light pulses are currently being considered. The first is a fibre coupled commercial laser; the second uses short (approximately 1 ns) pulses produced from either LEDs, laser diodes, or solid state optical devices. In order to preserve the fast light pulses, needed for PMT timing calibrations over the dimensions of Hyper-K, graded index fibres will be used. The alternate step-index fibres suffer from modal dispersion reducing the ability to separate pulses over larger distances, and thus inhibiting timing calibration over sub nanosecond pulses. The monitoring of light injection into the detector is essential for some calibrations to be made. A fraction of the light produced will be redirected towards optical sensors, most likely monitor PMTs. This would allow for comparisons to be made on a pulse-by-pulse basis. The light is injected into the tank using two different devices: the narrow-beam collimator and wide-beam diffuser each with their own set of objectives outlined below.

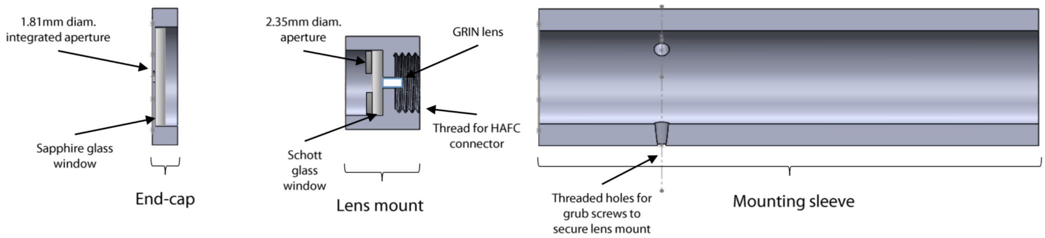

Figure 6.1: A schematic diagram of the collimator design used in the Super-K deployment. Taken from [151].

Narrow-Beam Collimator

In order to measure the optical properties of the water, a narrow beam of collimated light is needed. The collimator is designed to illuminate a small subset of PMTs. During the Super-K deployments, an opening angle of $3.5°$ was used to illuminate a 5×5 array of PMTs, however this value for Hyper-K is still to be determined. Illuminating a smaller array of PMTs is ideal for measuring the attenuating and scattering properties of light in water, which will be performed over multiple wavelengths ranging from 320 nm to 500 nm. Water attenuation is measured by observing light levels on given PMTs inside the illuminated array from the narrow beam. The scattering length is measured by monitoring the light detected by PMTs outside the collimated beam as a function of time and photon path length.

At present the final design for the collimator is still in development at the University of Warwick. The design tested and validated during the Super-K deployments (described in section 6.5) is shown in figure 6.1. The collimation is generated by a gradient-index (GRIN) lens, followed by a series of apertures. The GRIN lens has a pitch of $\frac{1}{4}$ with means it has a length equal to one quarter of a sine wave, a thus collimates to a point source at the surface of the lens. The optical fibre was secured in place to ensure correct alignment and the optics were mounted in a waterproof stainless steel assembly. Other potential designs for collimation, including the use of an achromatic doublet lens, are currently being considered.

Wide-Beam Diffuser

The motivation of using diffuser technology is to create a wide-angle beam of diffuse light to illuminate as many PMTs as possible. Provided this is done a well-understand beam which is, ideally, uniform in spatial intensity and timing, calibrations of the PMT gain and timing responses can be performed. Measurements of inter-PMT energies can give an indication of "hot" or "cold" PMTs which can then be calibrated. The performance criterion for Hyper-K require the diffuser to produce a well understood light cone over a $\pm 40^{\circ}$ angular range; this illuminates approximately 1000 PMTs on the far side of the inner detector. The calibration of PMT timing requires a short pulse with known origin and time. The diffuser must therefore also ensure there is no time dependence as a function of angle. Each PMT will be illuminated by at least two diffusers to allow for temporal cross calibration of the fibres.

The design of the diffuser is discussed in detail within sections 6.3 and 6.4. The diffuser performance through both laboratory measurements (section 6.2) and deployments in Super-K (section 6.5) are also discussed in the context of optical and temporal measurements.

Inner and Outer Detector Differences

The inner detector (ID) will include injector points on the barrel, directed horizontally into the tank, and the end caps, directed vertically. To measure the difference in optical properties as a function of depth, the proposed system will have seven horizontal injection points at 90° intervals distributed evenly at different depths. Eight vertical line injectors will be deployed, four at the bottom and four at the top of the tank. Each injector point will consist of one diffuser and one collimator system.

The geometric nature of the OD requires significantly more injection points to achieve full photo-sensor coverage. Nevertheless, the precision diffusers designed for the ID are not required to achieve the key objectives of the OD. Therefore a simpler diffuser system[1] has been proposed, different to those described in section 6.3.

[1] The exact design for the simpler diffuser is not yet known, likely candidates include using bare

Extrapolations from Super-K geometries predict that approximately 80 injection points will be needed to cover the full OD PMTs. In addition to these injection points, 12 collimators will be installed in the OD, helping to characterise the region further. Placing collimators in parallel to the PMT wall yields longer travel distances to increase the impact of absorption and scattering effects.

6.2 Laboratory Experiments

An in-house experimental setup at the University of Warwick is used for testing the performance of diffusers during research and development phases. The experimental set up is used to monitor the optical output and temporal signals through the diffusers as a function of angle. This section will describe the experimental setup used in the development of diffusers for the Super-K deployments.

6.2.1 Experimental Setup

The key motivation behind the experimental setup is to provide the light intensity and timing profiles of each test diffuser over a distribution of angles. The setup consists of a system which injects light through a 200 μm core step-index optical fibre into the diffuser being tested. The diffuser is mounted on a 360° rotation stage, and the signal is collected downstream by a photo-sensor. The whole system is enclosed inside an interlocked dark box. A schematic of the experimental setup is shown in figure 6.2, and a photograph in figure 6.3.

The light injection system is provided by a single pulsed semiconductor laser, which can be set to emit a wavelength of 450 nm (blue) or 520 nm (green). The laser diode is pulsed at 10 kHz, using the leading edge of a signal generator to trigger an analogue pulser circuit. The light pulse is injected into a 200 μm core 0.5 NA step-index fibre, approximately 1 m in length. The fibre optic cable terminates at a ceramic ferrule which is placed inside the diffuser. Experiments have shown the fibre position within the diffuser can cause differences to the amplitude of the optical output from the diffuser. The magnitude of this effect has a dependence on the

fibres, or diffuse reflectors.

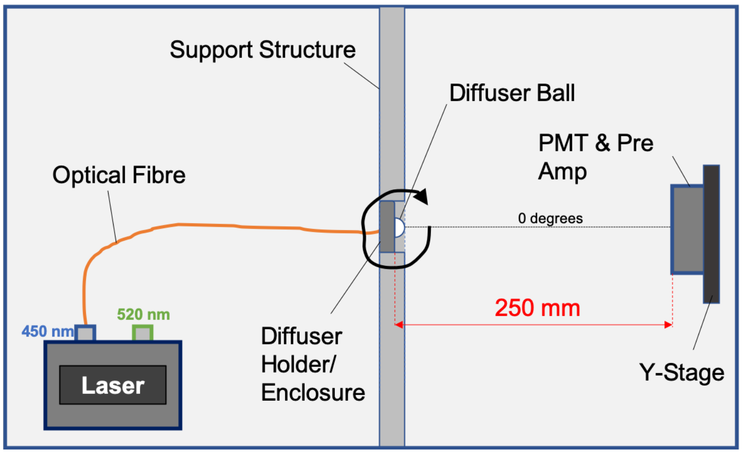

Figure 6.2: A schematic diagram demonstrating the experimental set up from a birds-eye view. *Maybe add coordinates?*.

diffuser shape. For this reason the fibre is consistently placed touching the back of the hemispherical diffuser dome, and secured in place with a 3D printed clamp.

The diffuser is positioned on a rotation stage which is placed on a 'bridge-like' support structure. The rotation stage is accurate to ±0.6 arcmin, and uses a stepping motor which can be accessed remotely via an Arduino-based control system [152, 153]. The stepping motor is calibrated so that 1000 steps equates to a movement of 1 degree. A metallic tube connected to a ring is attached vertically from the rotation stage and acts as a grip for either the diffuser, or diffuser enclosure. 3D printed alignment jigs ensure the diffuser is located at the centre of the grip, and is held in place using six screws triangulated over three different positions. This set up has the advantage of the diffuser being effectively suspended, allowing the full 360° horizontal plane to be scanned. A photo demonstrating the full assembly is provided in figure 6.3.

Downstream from the diffuser a Hamamatsu 6780-02 PMT is used to collect optical and temporal information for analysis. The PMT provides signal amplification that is tunable between 0 V → 0.9 V. The level of amplification follows a logarithmic relationship with respect to voltage input. Nevertheless, the PMT alone cannot provide enough signal amplification. Therefore to achieve a signal with an amplitude of greater than 1 V, a preamplifier is added inline after the PMT providing baseline amplification. The Ortec VT120 fast timing preamp is used as it can provide a

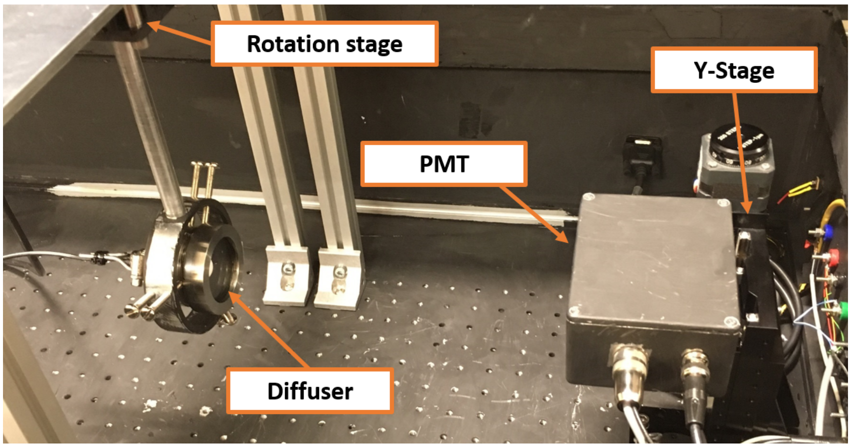

Figure 6.3: A photo showing the assembled experimental set up of the diffuser system (enclosure + diffuser ball) suspended in the grip, as well as the PMT box. Taken from [154].

sub-nanosecond rise time. The preamp and PMT are housed inside a box aptly named ”PMT box”, which is situated 250 mm downstream of the diffuser’s centre of rotation. The PMT box is secured to a Y-stage which can be used for alignment, as well as providing an additional dimension in which diffusers can be scanned. At this moment in time, the Y-stage has only been used for alignment purposes, however additional two-dimensional scans are planned for the future. A photo of the PMT box and Y-stage can be seen in figure 6.3.

It is important to note that the absolute power of the pulsed laser diode system, and environmental factors such as temperature, are not directly measured. The power was not monitored due to the available meters incompatibility with a pulsed light source; Given this, environmental factors were also not directly measured; instead it was decided to only make comparisons against relative spectra. As a result, quantitative conclusions of absolute light intensity measurements are not best to use. Instead, relative intensity measurements, normalised to the intensity measured at zero degree rotation, are used for comparative conclusions between different scans. Measurements of laser stability in bare diffuser measurements as a function of time have been made, and can be seen in figure 6.4. It can be seen that the laser stabilises at approximately the hour mark; therefore a total of 70 minutes is given between each scan to allow the laser power output to stabilise.

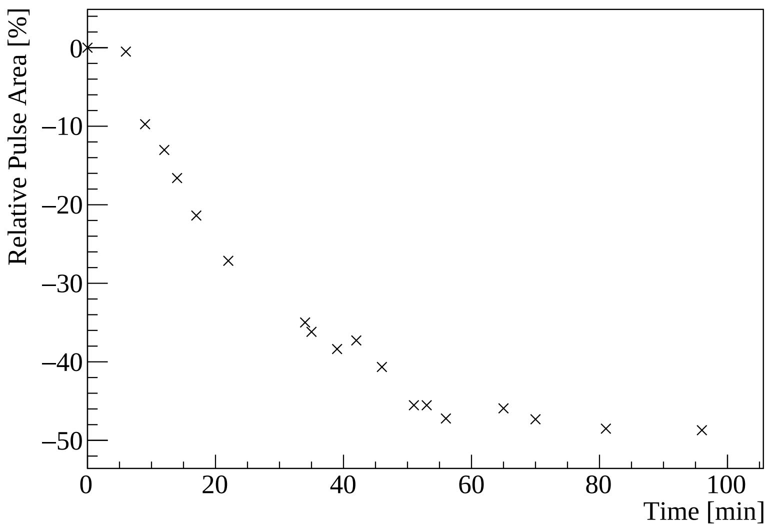

Figure 6.4: The laser power output stabilising as a function of time. The pulse area for a bare diffuser is measured in a zero degree on axis formation. Pulse areas are normalised to an initial time, $T = 0$, defined by the time the laser is switched on.

6.2.2 DAQ and Analysis Methods

Control of the experiment and DAQ systems are managed by LabView [155]. Scans are characterized a by series of angular sweeps defined by start and end angular positions, as well as step intervals. For example, one sweep may be defined from -60° to 60° at intervals of 2° steps; a scan can consist of multiple sweeps, typically taking a mean and RMS value over multiple sweeps for each angular position. Amplified signals from the PMT are fed through to an oscilloscope, where measurements can be taken. Two distinct methods of measurement are made: The calculated values taken by the scope itself, and the averaged waveform are both recoded. Both techniques take the average over 1000 pulses. At each position along a scan, the oscilloscope is reset and a delay of 10 seconds is applied to allow the scope to settle. This was done as it was found the sampling speed of the scope was low enough that, without delay, measurements from the previous position were included in the average for the current. An example pulse from a bare diffuser ball can be seen in figure 6.5. Relative light intensity distribution comparisons are taken using the height and area of the pulse. Timing information can be collected by measuring the pulse full-width half-maximum, and by measuring the pulse delay - the time between the laser trigger

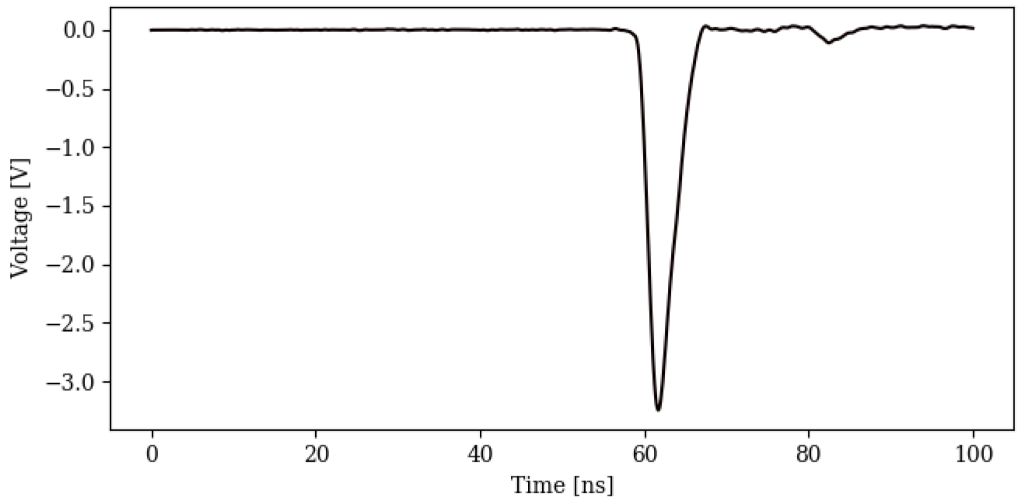

Figure 6.5: An example pulse from a scan of a bare PMMA diffuser.

and the rising edge of the pulse, defined by 10% of the peak voltage of the pulse.

Diffuser analysis is performed using a python analysis package developed in-house. The package has the versatility in analysing light intensity and temporal measurements as a function of angle and time. The majority of results seen within this chapter, unless otherwise stated, were created using this package.

6.3 Diffusers

The optical calibration work presented in this thesis will focus primarily on diffuser based technology. The primary aim of the optical diffusers is to provide a means of obtaining energy and timing information for calibrating photo-sensors in large scale projects such as Hyper-Kamiokande. This section and the next will discuss the research and development of optical diffuser technology and outline the diffuser calibration systems developed at the University of Warwick.

As outlined in section 6.1 the goals for the wide-beam diffuser are to create a well understood, preferably uniform, distribution over an angular range of $\pm 40°$, as well as having a uniform timing profile as a function of angle. In addition the development objectives include practical implications. The diffuser must be waterproof, passing soak tests, as to not affect either the diffusing optical properties, or the water it's situated in. Moreover, the diffuser must remain stable in gadolinium doped water. The diffuser must be able to withstand pressures of up to 10 Bar, as well as have a longevity on the order of multiple decades. Furthermore, the diffusing properties must not be affected, as a function of time, by any of the previously described criteria.

6.3.1 Diffusing Material

In 2017, studies were undertaken to find a diffusing material that could achieve 1% uniform light intensity over a $\pm 45^{\circ}$ light cone [2] [156]. The light injection system requires such a material to have good transmission (near 100%) over a range of ultraviolet to visible wavelengths, in particular 350 nm to 550 nm.

Generation one diffusers were made out of 50 μm glass beads suspended in a polyester resin. As light enters the resin photons can scatter multiple times off the glass beads due to their relatively small size. By the time photons exit the resin, they are emitted in a diffuse distribution. The light output over the required range was found to be uniform to 4%. However, spectroscopy measurements found that polyester resin absorbs light below 400 nm. Moreover, it was found the addition of glass beads reduced relative intensity by approximately 20% between 500 nm and 600 nm wavelengths.

For generation two a number of candidate materials where considered. Polystyrene and poly(methyl methacrylate), PMMA, were two of the options investigated for their optical transmission properties. The relative transmission are between 90% - 100% above 400 nm, with a gradual drop to approximately 75% (20%) and 55% (0%) at 350 nm (300 nm) for PMMA (polystyrene) respectively. This is shown in figure 6.6. Additionally the 48 μm particle size of PMMA ensures it has good diffusion properties, eliminating the need to add glass beads. For this reason PMMA was chosen as the diffusing material for the Super-K deployed optical calibration system.

Soak tests were performed on PMMA samples using both ultra pure water currently used in Super-K, and gadolinium loaded water to ensure future compatibility with the SK-Gd and Hyper-K projects. Traces of PMMA impurities were found to

[2] Note that the diffusing criteria have since changed

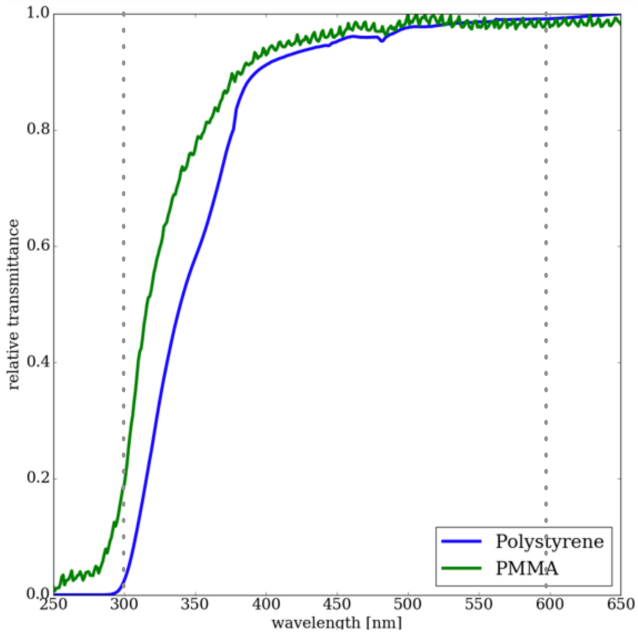

Figure 6.6: Relative transmission properties of PMMA and polystyrene. Taken from [156].

have leached into the water, and optical properties of the diffuser ball were adversely affected [156]. Figure 6.7 shows UV-VIS spectrum analysis of the different water samples exposed to PMMA. An idea material which does not affect water properties would follow the absorption and transmittance spectra of the control samples, indicating an absence of contamination. It can be seen that below 300 nm, the water absorption and transmittance properties rapidly degrade due to contamination from the suspended PMMA particles. To mitigate this, a water-tight enclosure was designed, and is outlined in detail in section 6.4.

6.3.2 Diffuser Shape

Alongside material, research and development of the diffuser shape was undertaken. The work primarily focussed on two designs, spherical and hemispherical. In theory with a perfect diffusing material, the spherical shape would emit a uniform distribution over 4π sr, whereas the hemispherical shape has geometrical limitations. However in practice, the hemispherical design is simpler to manufacture.

Light intensity distributions for PMMA spherical and hemispherical diffusers

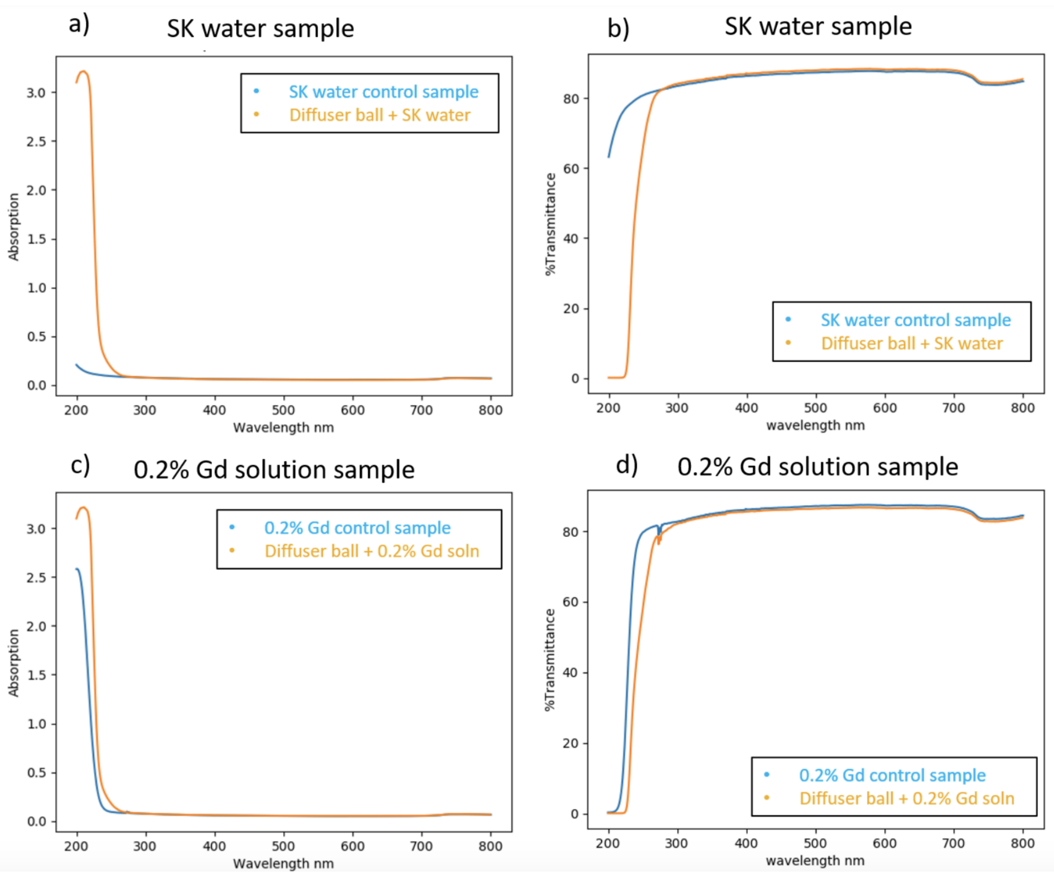

Figure 6.7: Soak test results for the optical absorption(left) and transmission (right) properties of the water over the UV-VIS spectrum, for different water samples. A Perkin Elmer Lambda 850 UV/VIS spectrometer was used. Each sample was measured in 10 mm path length disposable cuvettes and referenced against clean water.

measured over a range of $\pm 90^\circ$ is shown in figure 6.8a. A significant problem with full spherical diffusers was the amount of backscattered light, which had a strong dependence on fibre position with respect to the centre of the diffuser (figure 6.8b). Therefore, coupled with manufacturing considerations, a hemispherical diffuser design was chosen.

The performance of hemispherical diffusers was measured with respect to its dimensions. Diffusers were manufactured at 5 mm, 10 mm, 15 mm radii. The light output was found to broaden with larger diffusers, and the pulse width increased by 1.5 ns and 0.5 ns between 5 $\rightarrow$ 10 mm and 10 $\rightarrow$ 15 mm respectively. The final design featured a hemispherical PMMA diffuser of radius 20 mm with a 10 mm

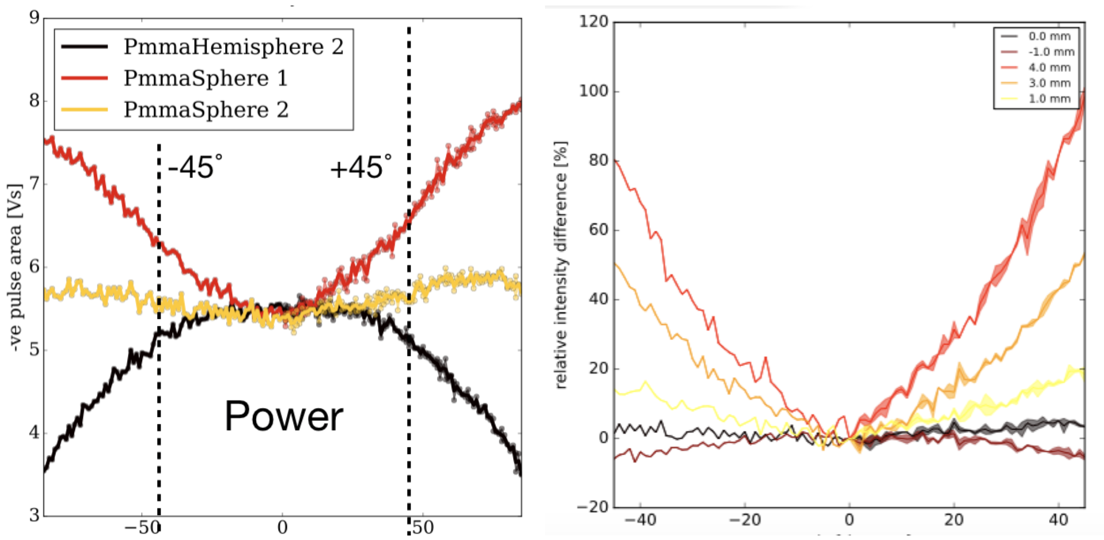

(a) (b)

Figure 6.8: (a) The light intensity distributions as a function of angle for spherical and hemispherical diffusers. (b) A plot demonstrating the relative light intensity for various different distances between the fibre and diffuser centre. Both plots have angle in degrees on the x-axis. Taken from [156].

thick cylindrical back of radius 30 mm for support. The final design can be seen in figure 6.9.

6.3.3 Manufacturing

The manufacturing process of PMMA hemispherical diffusers has a number of steps that are outlined within this section. PMMA is known to be porous, therefore all tooling machines has to be scrupulously cleaned of all contaminants as to not

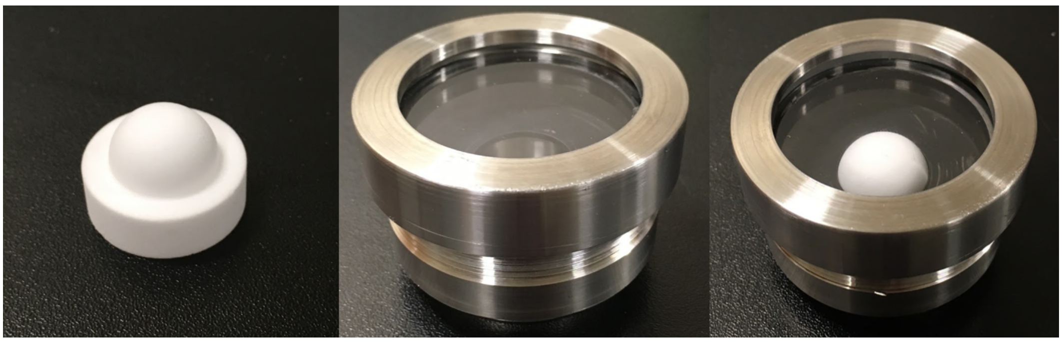

Figure 6.9: Photos showing an example of the diffuser (left), enclosure (middle), and diffuser inside enclosure (right). Taken from [154].

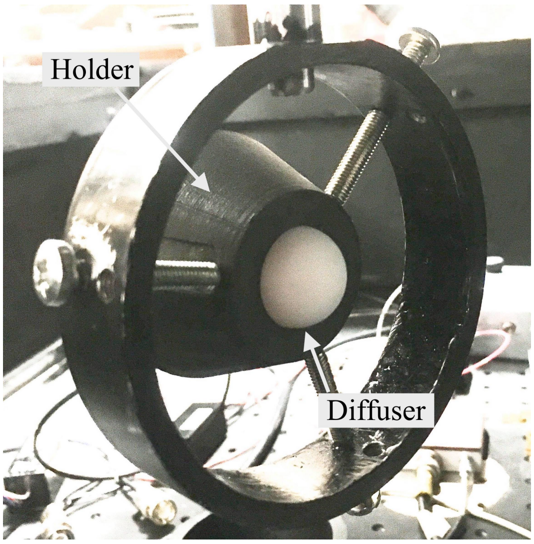

Figure 6.10: A photo of the bare diffuser experimental set up with the diffuser inside the 3D printed holder.

risk affecting optical properties. The PMMA is purchased in the form of a powder. A vibration mill is first used to prepare an amalgam, removing any potential air voids and compacting the powder down. The PMMA is then placed into a die and compressed in a hand operated vice at approximately 2 ton of pressure, monitored using a strain gauge. The die is then put into a sash clamp and heated in an oven at 175°C for 3 hours. A PMMA sintered rod is then extracted from the die, and machined into hemispherical diffusers. Each sintered rod of length 100 mm has the capability of producing two to three diffusers.

6.3.4 Bare Diffuser Performance

To measure the optical and temporal properties of bare diffusers, in the experimental set up described in section 6.2, a holder was designed to allow illuminations only from the hemisphere to reach the PMT. An example of a diffuser inside a 3D printed holder is shown in figure 6.10.

The light profile from the PMMA diffusers was scanned from $-40° \rightarrow 40°$ measuring the area of the light pulse in [Vs] at each step. When comparing the reproducibility over multiple diffuser samples it is more comparable to normalise with respect 0° and plot the relative difference, this is shown in figure 6.11, over

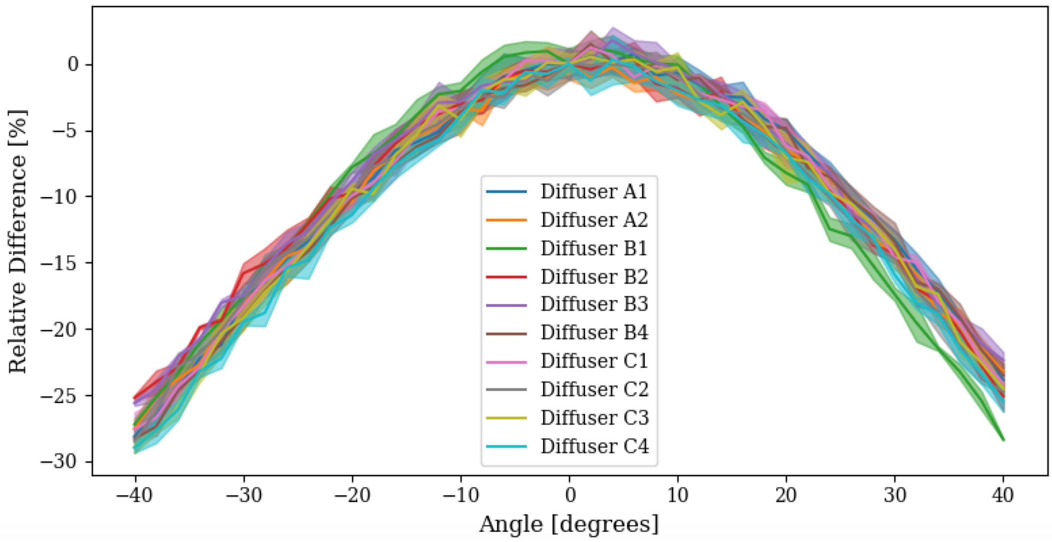

Figure 6.11: The bare diffuser light intensity profile, normalised at 0°, for 10 different diffusers demonstrating a test in reproducibility. The same letter indicates the same diffuser batch. Diffuser pairs 1 & 2 and 3 & 4 are made from the same rod.

a sample of 10 bare PMMA diffusers. It can be seen, with the exception of B1 which is believed to have had a minor alignment anomaly, all of the bare diffusers across the three batches and five rods agree within error. The uncertainty is derived as the RMS over repeat measurements. It is clear from figure 6.11 that the bare PMMA diffusers produce a consistent light intensity distribution over a range of ±40°. The light profile peaks at 0° and falls linearly with angle from approximately ±10° onwards. It can be noted that figure 6.11 appears to be weakly biased towards positive angles, which suggests either asymmetry in the diffuser or misalignment in the set up. Diffuser symmetry was tested by rotating the diffuser through 360° taking scans at regular intervals. From this test the peak intensity did not change with respect to diffuser rotation, which suggests the positive bias is due to a systematic misalignment of approximately 2°.

As the diffuser rotates by an angle θ, the total surface area of the diffuser visible to the PMT changes due to the hemispherical geometry. This can be mathematically described as:

$$2\pi r^2 - 2\theta r^2 \tag{6.1}$$

where r is the radius of the diffuser and θ is an angle of rotation between the limits of $-\frac{\pi}{2}$ and $\frac{\pi}{2}$. The $2\pi r^2$ term represents the surface area of a hemisphere excluding the base, and $2\theta r^2$ represents the surface area of a wedge from a sphere. The total surface area visible, relative to the surface area at $\theta = 0$ can then be written as:

$$\frac{2\pi r^2 - 2\theta r^2}{2\pi r^2} \tag{6.2}$$

which simplifies to

$$1 - \frac{\theta}{\pi} \tag{6.3}$$

thus defining a correction factor for the hemispherical geometry in the context of this experiment. The intensity profile can then be compared to that of a perfect hemispherical diffuser by applying this hemisphere correction factor:

$$x' = \frac{x}{1 - (\theta/\pi)} \tag{6.4}$$

where x is the variable you wish to correct for (usually light intensity), and θ is the absolute angle in radians. This derivation assumes perfect alignment, and that the PMT is at a sufficient distance away as to include the full diffuser inside the field of view. A plot of the relative light intensity corrected for a hemispherical geometry, using equation 6.4, can be seen in figure 6.12. Asymmetry effects through the systematic misalignment are inevitably enhanced through geometry corrections. However, figure 6.12 indicates that forward going light between approximately $\pm 10°$ is suppressed with more scattered light promoted between $\pm 10° \rightarrow \pm 20°$ region. Furthermore, accounting for geometric effects, the bare PMMA diffuser is uniform to 10% over an angular range of $\pm 40°$.

The temporal performance of the bare diffuser is measured primarily in the delay of the signal. The pulse delay is the time between the laser pulse trigger and the rising edge[3] of the pulse arriving at the PMT (figure 6.5). The relative signal delay as a function of angle is shown in figure 6.13. The signal delay is uniform to approximately 1% over an angular range of $\pm 40°$. The absolute time delay ranges from 48.7 ns to 49.3 ns giving a spread of around 1.2% across all manufactured

[3]This is defined by a threshold of 10% of the peak signal voltage

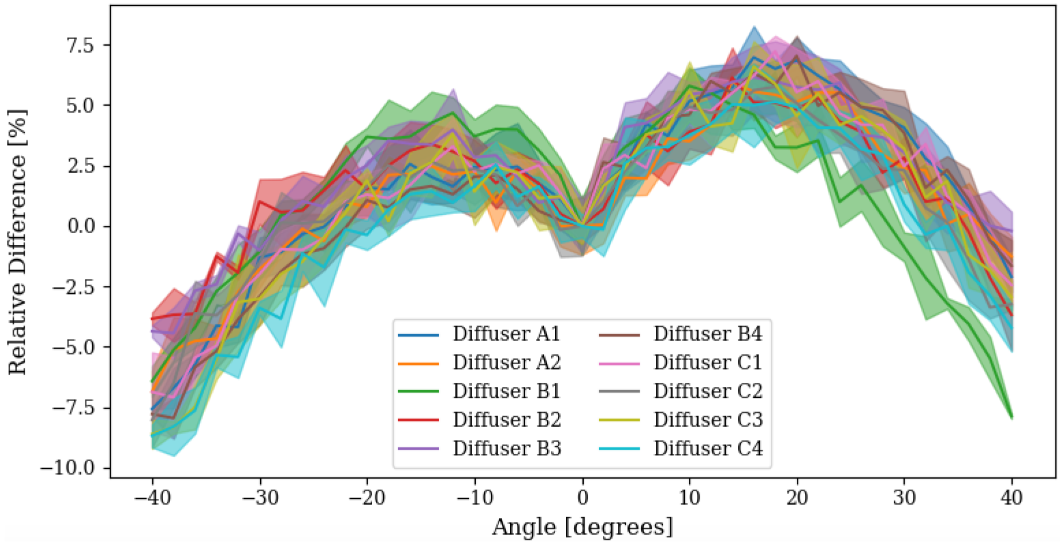

Figure 6.12: The relative light intensity profile of PMMA bare diffusers when corrected for hemispherical geometry effects through equation 6.4.

PMMA diffusers. The pulse width was also measured and is shown in figure B.1. However, a relatively large systematic uncertainty in PMT response means signal delay information provides a more reliable source of diffuser temporal performance.

6.4 Diffuser Enclosures

As discussed in section 6.3, soak tests had proven that PMMA diffusers were not waterproof, and exposure to water changed the light output properties of such diffusers. It was therefore decided to house the diffusers inside enclosures to protect both the diffuser and water environment from contamination. Such an enclosure would need to be watertight to 10 Bar, ideally easy to manufacture, and have no effect, or positive effect, on achieving the diffuser goals outlined in section 6.1. This subsection will discuss the enclosure research and development, and introduce results of the diffuser and enclosure system as a whole.

6.4.1 Base Enclosure Design

A number of key concepts were drawn up and gave rise to what will be referred to within this thesis as a base enclosure design. The concepts included fibre injection,

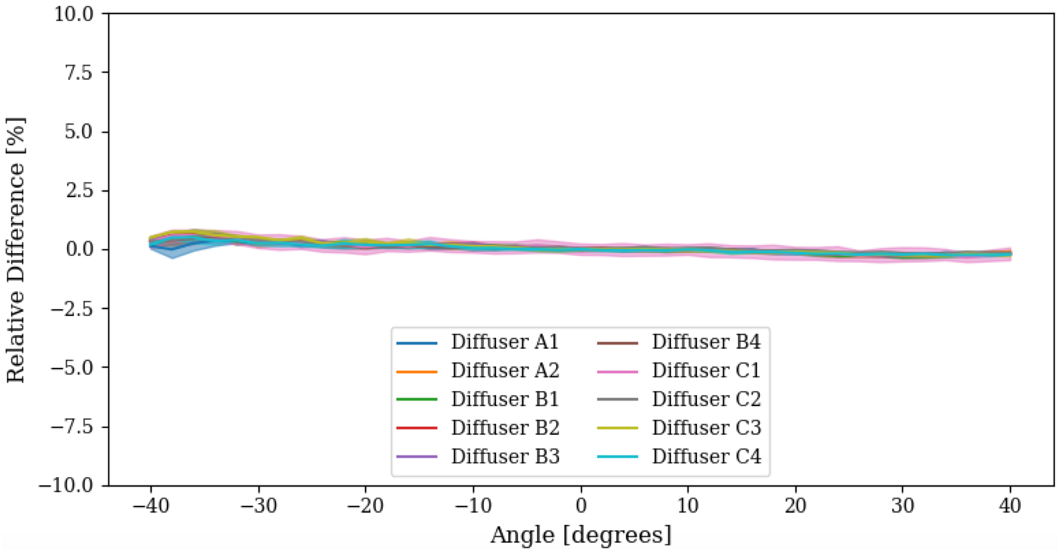

Figure 6.13: The relative signal time delay as a function of angle, normalised to 0°. The same ten PMMA diffusers from figure 6.11 are used.

materials, and water proofing measures. The base design consists of a stainless steel enclosure, with a glass window on the front, and a hole for fibre injection at the back. Water-tightness is achieved through a mixture of o-rings and epoxy resin.

6.4.2 Materials

The main body of the diffuser enclosure during the early stages of development was made out of 304 stainless steel. This was changed to 316 stainless steel for the deployment in Super-Kamiokande (section 6.5) because of its better chemical resistant properties. Two different glass materials, sapphire and Schott, were tested for the window and were found to have little to no difference in optical transmission and profile properties. A 6 mm thick Schott glass with a 50 mm diameter was chosen for the window. Water-tightness was ensured using a combination of Viton o-ring gaskets, as well as a water and chemical resistant epoxy resin. All materials were subject to soak tests in ultra pure and gadolinium loaded water; each material also underwent pressure tests up to 10 bar pressure for at least 12 hours underwater.

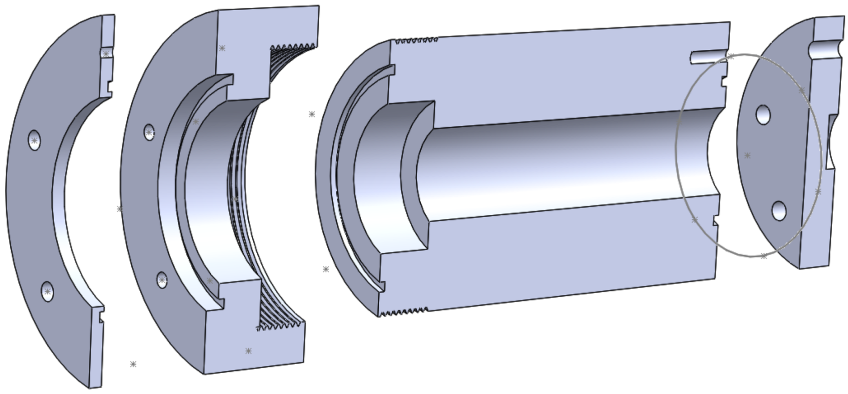

Figure 6.14: A cross-section of the version 1 (V1) diffuser enclosure design.

6.4.3 Enclosure Development

Major developments of the diffuser enclosure revolved around two key base designs, known as version 1 (V1) and version 3 (V3). Intermediate phases between these are referred to as version 2 (V2) designs. However, since these acted only as conceptual stepping stones between V1 and V3, and no measurements were ever taken with these designs, they will not be discussed in detail within this thesis. Schematic CAD drawings of concept V2 designs are provided in the appendix (figure B.2).

V1 Design

A cross section for the initial enclosure design, labelled V1, is shown in figure 6.14. The design consists of a 75 mm long main body, with a 27 mm front screw cap, and 3 mm window cap which holds the window in place whilst screwing onto the main body. A 10 mm thick solid disc with a hole for fibre feed-through makes up the back end piece, known as the base lid, which is attached via 6 threaded screws in hexagonal formation. Moreover, the design also allows the enclosure to be directly attached to a pressure vessel in place of the base lid. Fully assembled, the V1 design measures 100 mm in length, with a 60 mm main body diameter, which rises to 75 mm at the front. The diffuser base sits 30 mm away from the front end of the enclosure. The origin of diffusion, defined by the point at which the light is injected from the fibre into the diffuser, is located 17 mm from the front of the glass window. The diffuser shoulder is also exposed, so to obtain hemispherical diffuser results

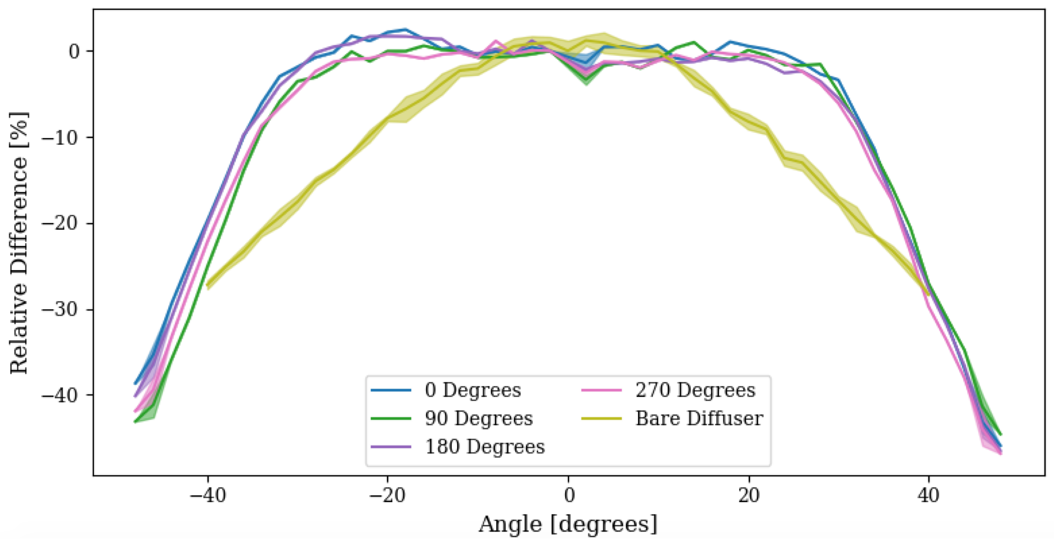

Figure 6.15: The optical profile using the V1 diffuser enclosure system. The full system was rotated through 360° over 90° steps, at one sweep for each scan. An example bare diffuser profile is also shown for comparison.

improvised shielding from black electrical tape was often used. O-ring gaskets at the front and back of the enclosure provide water-tightness. The V1 design was too large and heavy to match any practical considerations for deployments into Super-K or Hyper-K, but did allow for important preliminary enclosure studies to be made.

V1 Optical Performance

The light profile from a 20 mm hemispherical diffuser installed inside enclosure V1 is shown in figure 6.15. The diffuser and enclosure were rotated as a full system through 360° to compare the optical profiles over two different planes. The measurements suggested the V1 enclosure promoted high angle photons, within it's respective field of view, relative to the bare diffuser profile in figure 6.11. The resultant profile is flat within approximately 2% over an angular range of approximately ±25° to ±30°. The light intensity drops linearly as the enclosure gradually eclipses the diffuser towards higher angles. The change in profile is largely because of two factors. The first is that the often shoulder of the diffuser is not covered in V1, meaning more than the intended hemispherical diffuser is visible. The second is because of specular reflections from the enclosure which promotes otherwise lost light at higher angles.

It was standard practice in the early stages of research and development to

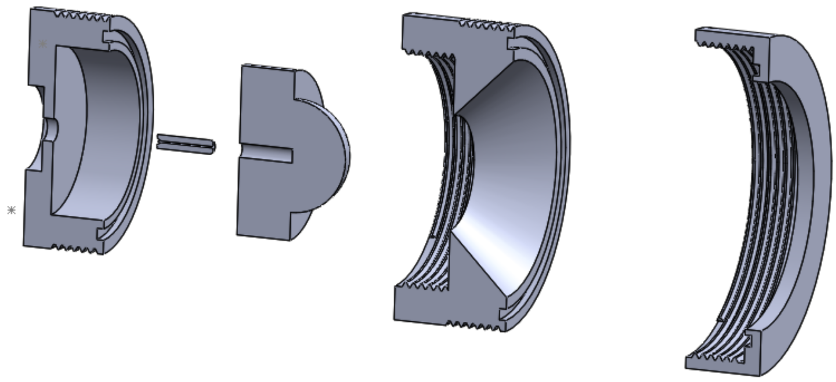

Figure 6.16: A cross-section schematic of the V3 diffuser and enclosure with a torch design.

perform measurements for only one sweep at a time. Combined with an uncertainty in unmonitored laser power between scans, an error in repeated measurements is not able to be taken. Therefore the results shown in figure 6.15, must be taken with a relatively large qualitative uncertainty, and were used as a guide for developmental paths only.

V3 Design

The premise for version 3 was to design an enclosure fit for the Super-Kamiokande deployments outlined in section 6.5. Figure 6.16 shows a schematic drawing of the cross-section of both the diffuser and the enclosure V3. The V3 design consists of three segmented parts which screw together, named the base, main body, and end cap. The base segment, 15 mm long with a diameter of 42 mm, holds the diffuser and includes a hole for fibre injection. The role of the main body is to provide shielding against the diffuser shoulder as well as facilitate light output objectives using internal enclosure reflections. During development phases there were two designs for the main body: The first, shown in figure 6.16, was a "torch" with a 96° field of view designed to promote forward going light using diffuse reflections of high angle photons. The second was a "bucket" design with a flat face to the outer edge and then a perpendicular wall. Both face designs are painted matte black in order to remove specular reflections off the stainless steel surface, encouraging any remaining reflections to be diffuse. The main body is 21 mm long with a diameter of

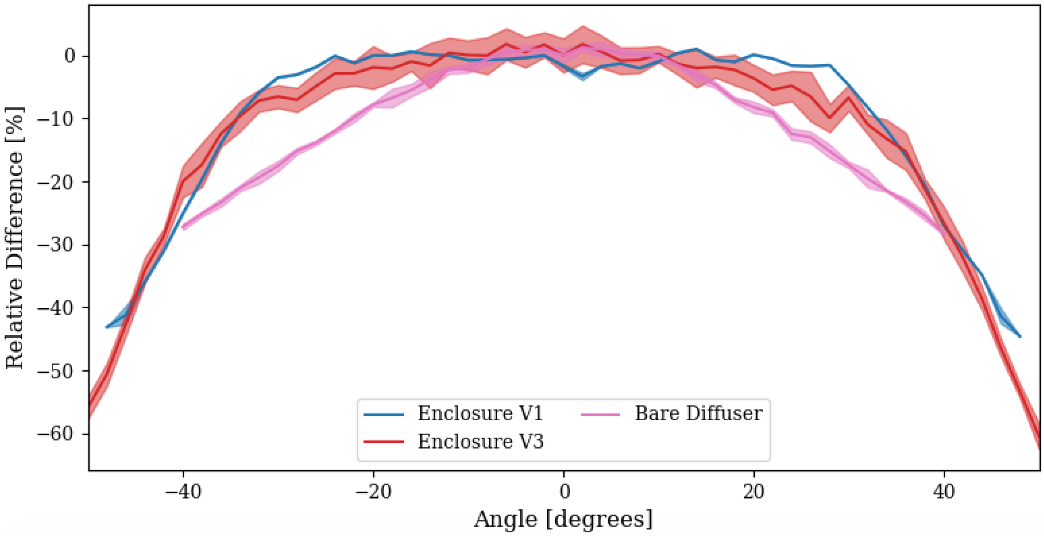

Figure 6.17: The relative optical profile of the V3 enclosure, with comparative profiles for the V1 enclosure and bare diffuser also shown. The optical profiles are normalised to 0°.

54 mm. As with V1, the front end cap holds the glass window; the cap is 14 mm in length and has a diameter of 60 mm. When fully assembled the enclosure is approximately 35 mm in length and is designed to house the "final design" diffusers outlined in section 6.3.2. Pictures of the fully assembled V3 enclosure design are shown in figure 6.9.

V3 Optical Performance

The optical profile for the V3 enclosure, with visual comparisons to the V1 enclosure and bare diffuser, is shown in figure 6.17. The profile is flat to within 10% over an angular range of approximately ±35° to ±40°. Despite the loss of the diffuser shoulder, the diffuser reflections from the matte black torch design promote angle photons in the forward direction to help flatten the distribution. The field of view also increased between V1 and V3 by an estimated $5° - 10°$ thanks to the shallower end cap design. The enclosure V3 designs optical profiles had good reproducibility which was seen for the Super-K deployment in figure 6.27.

Temporal performance of example V1 and V3 enclosures, and the bare diffuser are shown in figure 6.18 and figure 6.19. The pulse signal delay for enclosure V3

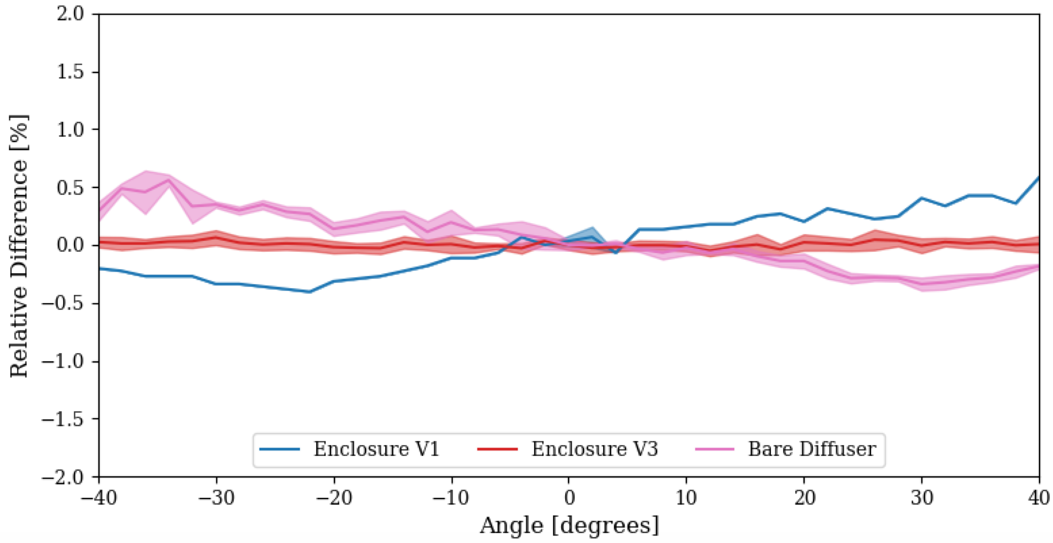

Figure 6.18: The relative signal delay, normalised to 0°, as a function of angle. Measurements for the V1 and V3 enclosures, and the bare diffuser are shown.

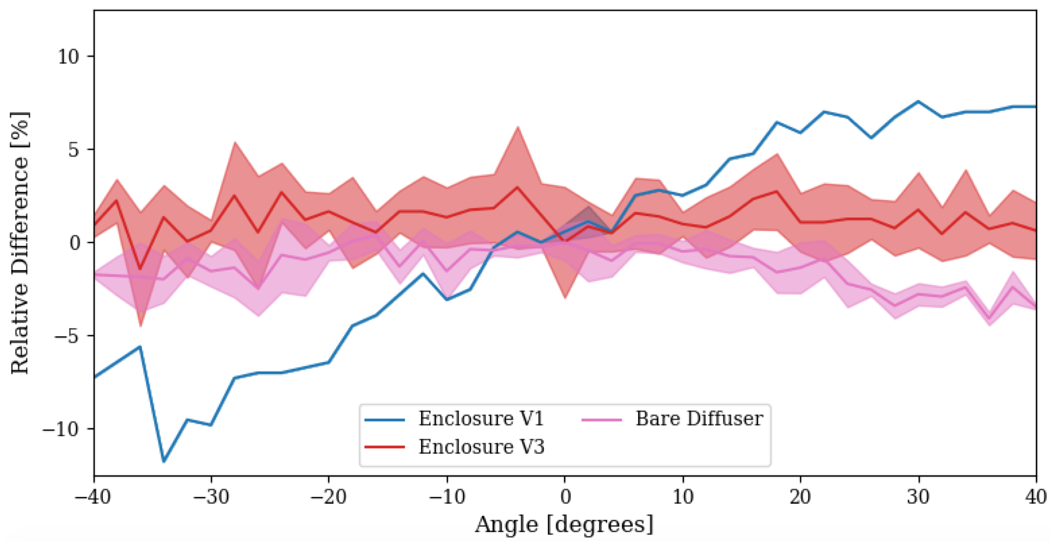

Figure 6.19: The relative pulse width as a function of angle for the V1 and V3 enclosures, as well as the bare diffuser. Each plot is normalised to 0°.

Figure 6.20: Pressure vessel used for diffuser and enclosure pressure tests at the University of Warwick.

is uniform as a function of angle. Moreover there is circumstantial evidence that V3 performs better than V1 or even the bare diffuser, however the likelihood is the sloped features for V1 and the bare diffuser in the signal delay is from minor misalignments in the experimental set up. Absolute measurements indicate pulse delay of 44.5 ns for V1 enclosure, (49.0 ± 0.3) ns for the bare diffuser[4], and 52.5 ns for enclosure V3. The increased delay from bare diffuser to inside the V3 enclosure could be attributed to addition of propagating through a glass window. The shorter delay seen in the V1 enclosure is likely due to changes in the experimental setup between measurements. The pulse width, measured by the full-width half-maximum, also seems to favour the V3 enclosure in terms of uniformity over angular space. The V1 enclosure exhibits unusual behaviour for the pulse width that could be attributed to asymmetries in specular reflections, however this is not known. In summary, the V3 enclosure has good temporal performance, yielding uniform distributions in both signal delay and pulse width over and angular range of $\pm 40°$.

6.4.4 Pressure Testing

Water pressure tests are performed using a vessel shown in figure 6.20. The vessel is made out of stainless steel and consists of a main container with two lids. The front lid contains a glass window from which observations can be made during tests. The back lid contains a feed-through injection point for the fibre optic cable. Sixteen clamps, eight top and eight bottom, are tightened using a torque wrench to squash two large o-rings gaskets and ensure a water-tight seal up to and beyond 5 bar of pressure.

Originally the V1 enclosure main body attached directly to the back plate of the pressure vessel. This had the effect of exposing the inside of the enclosure to external atmospheric pressures through the fibre feed-through. Furthermore, because the main body was directly attached to the vessel, the full V1 enclosure was never pressure tested in its fully assembled state. Nevertheless, V1 enclosure pressure tests provided performance validation in the materials, gaskets, and front assembly mechanisms.

Failures in the ability to test fully assembled V1 enclosures, set about changes in the pressure testing methodology for future enclosures. Instead of being attached directly, the V3 enclosure would instead be fully submersed in the water. This brought with it logistical challenges in sealing the fibre feed-through during pressure tests. The initial solution was to use a silicone gel to plug the gaps between the fibre and vessel, a system which worked with relative success throughout the Super-K deployment phase. More recently, a high-pressure fibre feed-through has been used to couple the fibre into the vessel. The was not, however, implemented until after the Super-K deployments.

The definition of successful and failed pressure tests comes down to a number of factors. Firstly, quantitative measures of the pressure inside the vessel are made as a function of time through the test. Consistent drops in pressure can signify a vessel failure, whereas a small singular drop may indicate an enclosure failure. Secondly, qualitative observations of the enclosure and diffuser are made once they have been removed from the vessel. Evidence of water ingress into the enclosure,

[4] Where the error is taken from repeat measurements in figure 6.13

condensation, and diffuser damage are looked for. Finally the optical profiles are retaken and compared against relevant profiles pre-tests. It is known that water can affect the optical properties of PMMA, and thus changes in the optical profile may indicate water contaminations and thus a failed pressure test.

The V3 enclosure waterproofing consisted of two systems: internal o-rings, and external epoxy resin. The internal gasket system had already been proven to work during V1 enclosure testing, but did not provide any waterproofing through the fibre-enclosure coupling. A chemical resistant epoxy resin was liberally applied both at the fibre injection point at the base of the enclosure, and at the screw connection points between each enclosure segment to allow the epoxy to seal any gaps via capillary action. At this stage a number of enclosures failed pressure tests. The caused was deemed to be poor bonding between the epoxy resin and the fibre furcation tubing [5], which under stress formed minute cracks and gaps which water could penetrate under pressure. Strain relief measures were manufactured and added to the V3 design to counteract stress on the convex fibre-epoxy bond. These included an epoxy filled stainless steel "top-hat" and a lateral support attached to the fibre with polypropylene tie wraps. The strain relief measures can be seen in figure 6.21. Once strain relief measures had been put in place, the V3 enclosure designs successfully passed all pressure testing criteria outlined previously. The optical profiles of an example diffuser enclosure before and after successful pressure tests are shown in figure 6.22. It can be seen that the profiles are unchanged over the pressure tests within the RMS error from repeated measurements.

6.4.5 Condensation Testing

The water inside Super-Kamiokande has an ambient temperature of approximately 13°C. A relatively cold temperature, a potential concern was the build up of condensation inside the diffuser enclosure. To address this concern an assembled diffuser was placed in a cold box at 5°C and then 0°C for three and two consecutive days respectively. No visual condensation was found over the 5 days of testing. The dew

[5] The furcation tubing material was predominantly PVC, however the exact makeup was not disclosed by the manufacturer.

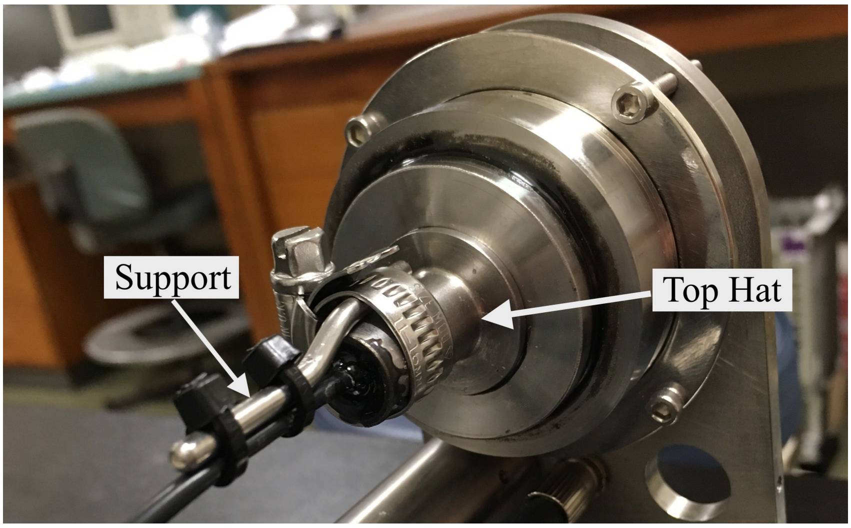

Figure 6.21: A photo demonstrating the strain relief measures used to protect the epoxy resin bonding to fibre furcation tubing in the Super-K deployed V3 enclosures.

point changes as a function of both ambient temperature and humidity. To achieve a dew point of below 10°C, the laboratory temperature and humidity during the diffuser enclosure assembly needed to be considered. Efforts were made to lower the environmental humidity during diffuser enclosure assembly, in an attempt to suppress the internal dew point to below the 10°C threshold.

6.5 Super-Kamiokande Deployment

As the Hyper-Kamiokande experiment is under construction, the proposed optical calibration light injection system was deployed into the sister experiment Super-Kamiokande. The objective was to both test the calibration optics as well as provide direct physics measurements for the Super-K experiment. This section will outline both the temporary winter 2018 test and more permanent summer 2018 deployments, as well as provide a preliminary discussion on the diffuser performance inside Super-K.

6.5.1 Test Deployment

In January 2018 a test deployment was scheduled for the light injection system. The purpose was to trial the proposed light injection system and gain experience in preparation for the summer deployment. The optical calibration devices, consisting of

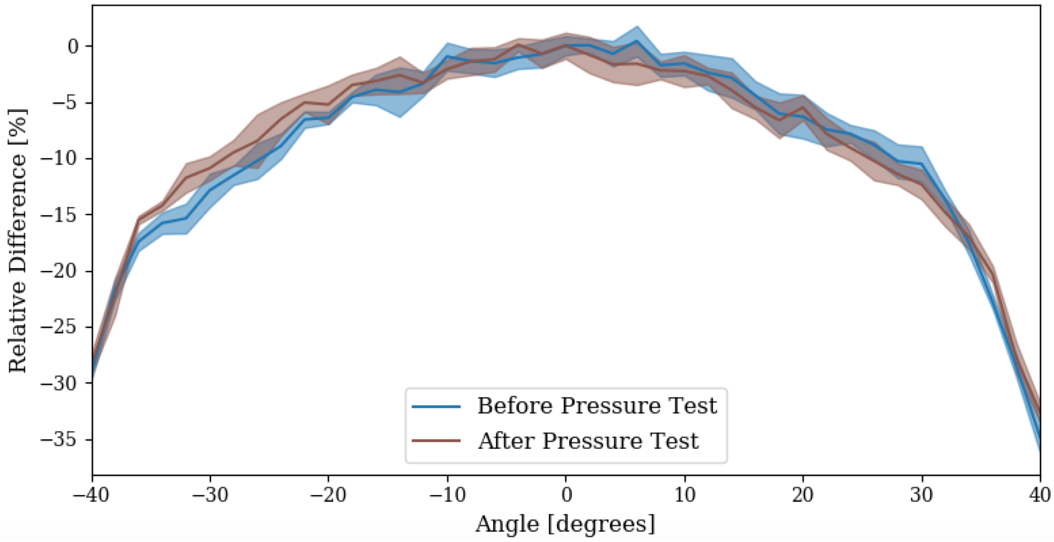

Figure 6.22: The optical profiles of a diffuser inside enclosure D1 before and after pressure tests. Each optical profile is normalised to the pulse area at zero degrees. The solid line shows the mean, the shaded part is the RMS, over repeat measurements.

a diffuser, collimator, and bare fibre, were attached to a mounting plate and lowered into the top of the Super-K tank via a calibration port. A simplified representation of the optical equipment installation methodology during the test deployment is shown in figure 6.23a.

A 20 mm PMMA hemispherical diffuser was used inside a V3 enclosure similar to that shown in figure 6.9. An early design collimator was also attached, and a bare fibre was used as a control. The test deployment used 200 μm core 0.22 NA multimode step-index fibres, notably different to the 0.5 NA fibres used for the summer deployment. Threaded screws held the optical elements in place, and the mounting disc was lowered using a mechanical winch with stainless steel chains attached to three triangulated shackles.

Light injection was provided through a 1 mm core fibre by an electronically pulsed LED system provided by the University of Liverpool. The light from the 1 mm core fibre was then separated into three 200 μm core step-index fibres coupled in a triangular formation. The first injected light into the tank, the second fed through to a monitor PMT, and the last was attached to an oscilloscope for in-house monitoring. Light pulse durations were varied to effectively increase the magnitude of light emitted from the optical devices. The duration of the pulses were not measured

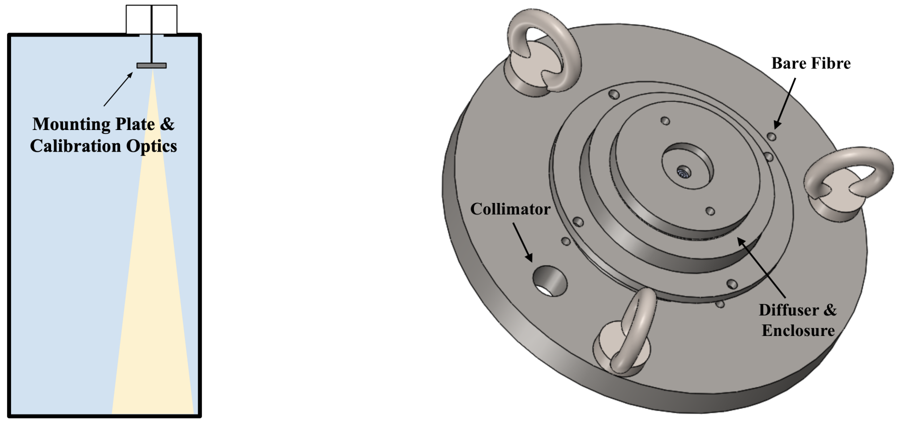

(a) (b)

Figure 6.23: (a) A simplified drawing demonstrating the installation of calibration optics in Super-K during the test deployment. (b) The mounting plate used during the Super-K test deployment, with mounting positions for each optical system labelled.

directly, but intensity values corresponding to the pulse duration were arbitrarily defined through the input register on the FPGA board. The nature of the diffuser devices required higher relative intensity compared to the bare fibre and collimator, which was achieved through longer pulse lengths. A combination of long undefined pulse lengths and step-index fibres meant information regarding potential timing calibration performance was not possible.

The PMT hit response was recorded for the top, bottom, and walls of the tanks to obtain the average number of hits per event over each individual PMT. From this diffuser and bare fibre event displays can be made to visually characterise the diffuser performance, these are shown in figure 6.24. A trigger was taken using a 473 nm laser from the bottom tank injection point. Each run consisted of approximately 100,000 events triggered at a rate of 100 Hz. Temporal cuts over the laser trigger and pulse width were applied to isolate the relevant events. Example event displays for Super-K PMT hit occupancy using the diffuser and bare fibre assemblies are shown in figure 6.24. Drawing quantitative conclusions between the two plots is difficult given the different, also arbitrary, intensities in light injection. Nevertheless qualitative comparisons can be made. Firstly the emitted light from the diffuser assembly can be seen in the Super-K PMTs approximately 40 m away from the top

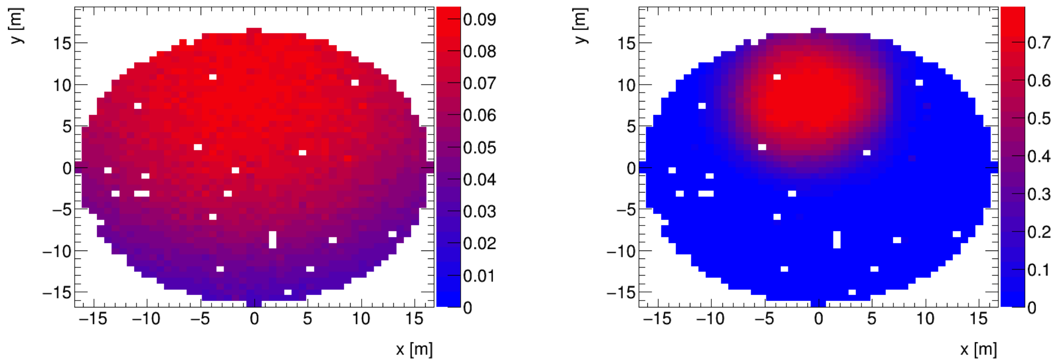

(a) Diffuser (b) Bare Fibre

Figure 6.24: The Super-K PMT hit occupancy over the bottom of the tank for (a) the diffuser and (b) the bare fibre control. The units of hit occupancy are number of hit per event/ns.

to bottom of the tank. The spot size for the diffuser is significantly larger than the bare fibre control, which indicates the diffuser is performing it's intended role in illuminating a wider spread of PMTs. The hit occupancy for each individual illuminated PMT is an order of magnitude lower than the bare diffuser, despite the longer pulse length used for the diffuser. Future development considerations were therefore made to maximising light input into the diffuser and minimising losses through attenuation in the fibre and coupling. In theory this would also allow short enough pulse widths to enable timing calibration.

Zeroth order comparisons can also be made to the experimental laboratory results shown outlined in figure 6.17. The geometric field of view from the top to the bottom of the tank spans approximately $\pm 20°$. It can be seen from the V3 enclosure profiles in figures 6.17 and 6.27, the relative light intensity in air varies no more than around 10% over this field of view. A projection of the x-axis in the diffuser event display (figure 6.24a) at the y-axis injection point can be seen in figure 6.25. Roughly a 20% decrease in intensity is seen over approximately $\pm 20°$, more than the laboratory results. The reason for such a discrepancy can be explain through unaccounted factors such as, the greater refractive index of water, attenuation length, as well as geometric affects such as a $1/r^2$ relation and PMT solid angle. The short time between the test and summer deployments meant that only basic data analysis studies could be performed before production for the summer deployment had to

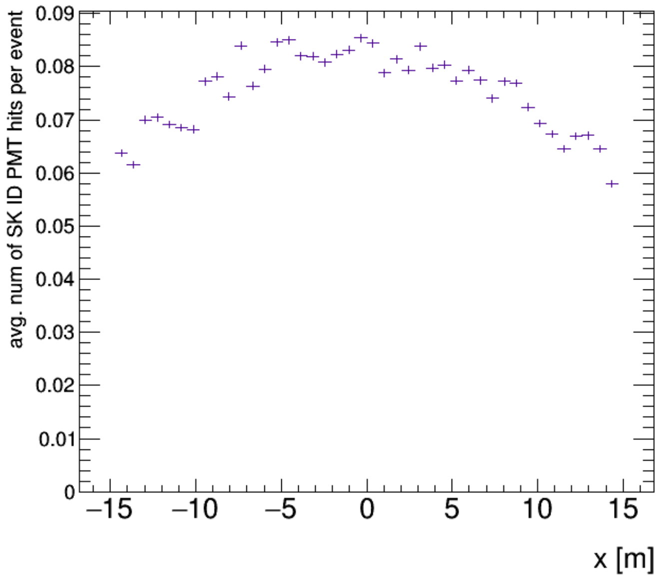

Figure 6.25: A projection of the diffuser light profile in the x-axis, taken at the point of injection in the y-axis.

begin. The optics were left in the tank for approximately six months. Afterwards the optics were taken out with no obvious mechanical failures found in the diffuser assembly.

6.5.2 Summer Deployment

In the summer of 2018, the Super-Kamiokande detector was drained for scheduled maintenance, and an updated optical calibration system from the test deployment was installed. Similar to the proposed Hyper-K inner detector configuration outlined in section 6.1, five injectors were installed at regular vertical intervals (B1 to B5) on the Super-K tank (figure 6.26a). Each light injection system consists of an updated collimator, bare fibre control, and an amended V3 diffuser assembly which included the additional strain-relief waterproofing measures outlined in section 6.4.4. The calibration equipment was mounted on the inner detector PMT frame using the bracket shown in figure 6.26b. Alignment over 3 degrees of freedom was controlled through adjusting triangulated screws at the bottom of the bracket. Additionally an optional laser pointer could be used to illuminate opposing PMTs acting as an alignment aid. Tyvek sheeting surrounded the mounting bracket in an attempt to

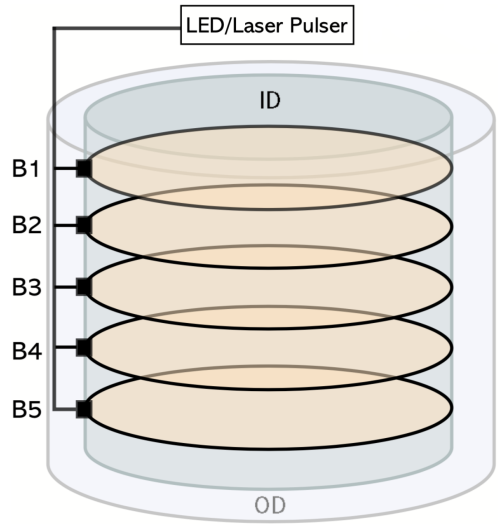

(a)

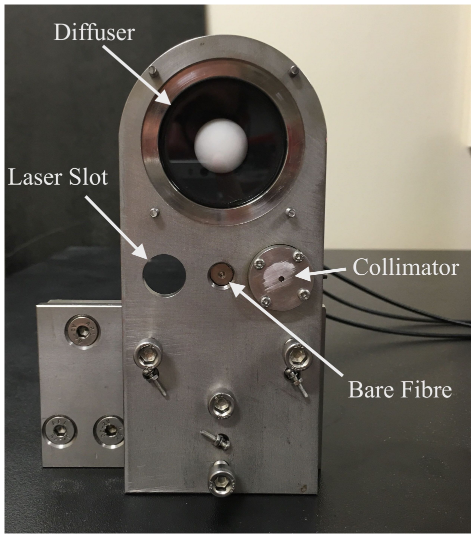

(b)

Figure 6.26: (a) A representation of the five light injection points (black squares) used for the summer deployment, taken from [151]. (b) The redesigned mounting bracket for the summer deployment.

reduce backscattered light from the optical devices entering the inner detector tank. The first light injector was installed on the 29^{th} June 2018; the final injector was installed on the 13^{th} August 2018.

Ten bare diffusers were manufactured for the summer deployment, with each individual light profile shown in figure 6.11. Seven fully assembled diffuser assemblies were made, five originally designed for deployment and two acting as spares. A selection process based on qualitatively selecting the most consistent relative light profiles dictated which bare diffusers would be used in assembly. The relative light profiles for the resulting fully assembled diffuser systems, labelled D1 to D7, are shown in figure 6.27. Table 6.1 outlines which diffuser assembly was installed at each light injection point.

Photon injection into the calibration optics was provided by the same set up used in the test deployment described previously. A pulsed LED provided a light source which is then partitioned into three outputs: A designated monitor PMT, on-site monitoring system for validity checks, and the calibration optics. The light is propagated through a 200 μm core step-index fibre optic cable which changed from 0.22 NA from the test deployment to 0.5 NA to maximise the light yield through the

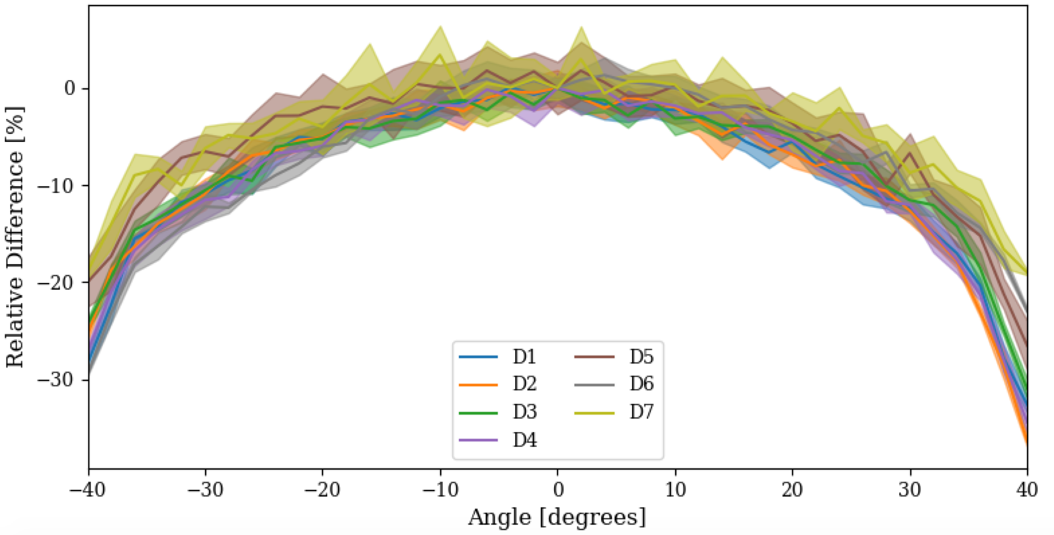

Figure 6.27: The seven full diffuser enclosure assemblies for the Super-K deployment, labelled from D1 to D7 during the assembly phase for clarity during measurements.

Full Diffuser Assembly	Injection Point Installed	Comments
D1	B1	
D2	Spare	Spare at Super-K
D3	B3	
D4	B2	
D5	Spare	Kept at Warwick for testing
D6	B5	
D7	B4	

Table 6.1: A summary of which diffuser assemblies were installed at each of the injection points for the summer deployment.

fibre. Underwater fibre optic connections were used close to the mounting bracket to limit the strain on long fibres during deployment, particularly with injection points near the bottom of the tank. Water-tightness of the connections was ensured by submerging the connections in boxes filled with Mineguard™, a viscous epoxy material developed in the mining industry previously used in waterproofing Super-K PMTs [80]. The optical calibration system was designed with a longevity on the order of approximately 20 years, and is expected to remain in the tank collecting calibration data for the foreseeable future.

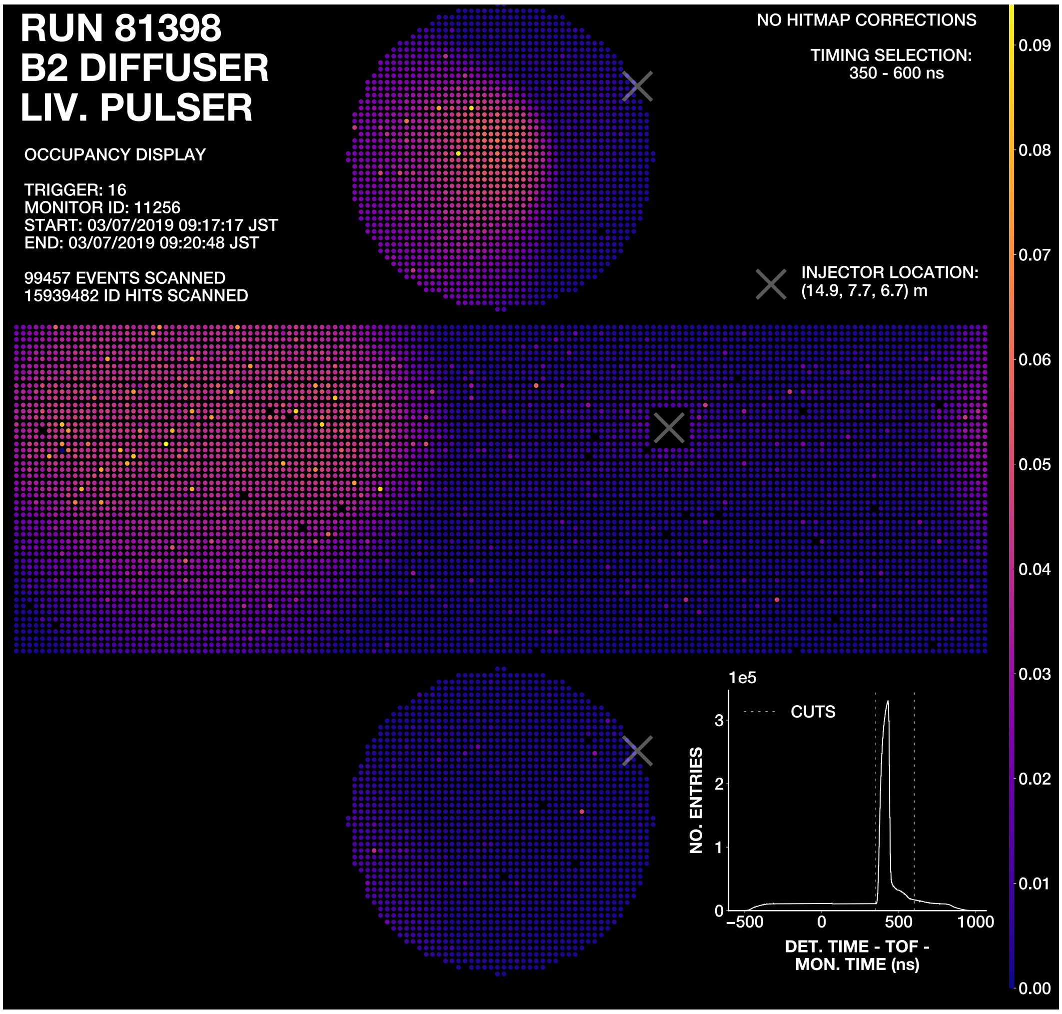

Figure 6.28: An example PMT hit occupancy event display for diffuser installed at the B2 injection point over the full detector. The number of SK PMT hits as a function of time is also shown in the bottom right, from which cuts are applied. Plot modified from [157].

6.5.3 Results

Analogous to the test deployment the PMT hit response for all the calibration optics was measured around the tank; firstly using the pre-existing Korean laser system, secondly using the UK light injection system described above. An example diffuser event display, located at the B2 injection point, is shown in figure 6.28. The same 473 nm laser trigger was used as the test deployment. The number of Super-K PMT hits is recorded as a function of time, a monitor PMT time pedestal is subtracted and a correction is also applied accounting for time-of-flight. Temporal cuts can be applied to the resulting plot, shown in figure 6.28, to isolate the light injection pulse. From the duration of the temporal cut one can estimate the length of a typical light injection event to be on the order of a 200-300 ns. The lower cut threshold is strict to veto any hits before the pulse arrives; the upper threshold can be relaxed (tightened) to include (exclude) internal detector reflections. Super-K event displays for all other installed diffuser systems can be found in the appendix, figures B.3 to B.6. A shadow can be seen in some of the diffuser displays, this is believed to be caused by the collimator assembly protruding too far outwards in the mounting bracket (figure 6.26b). The shadowing effect is most prominent in B4 and B5 whereby the bottom of the tank is illuminated and the collimator blocks the line-of-sight.

Preliminary qualitative conclusions suggest that the diffuser is working as expected. The deployment appears to have been successful and the event displays are promising. A full analysis is in progress which aims to quantify the calibration optics performance, make comparisons with laboratory profiles, and outline the systems potential to perform PMT calibration and water property measurements inside Super-K. The analysis will also be extended to make performance predictions for other water Cherenkov detectors, most notably Hyper-Kamiokande.

6.6 Future Development

Diffuser research and development has continued since the Super-K deployment, with the intention to develop a final system for mass production for the use of Hyper-K, and potentially other large scale water Cherenkov detectors. This section will discuss the recent investigations into PTFE as a new diffusing material as well as enclosure design research and development moving forward.

6.6.1 PTFE

A discussion into diffusing materials is provided in section 6.3.1. Poly(methyl methacrylate), otherwise referred to as PMMA, was chosen as the diffusing material for the Super-K deployments. Whilst PMMA is known to have good diffusing properties and produces well understood optical profiles, the notable disadvantages

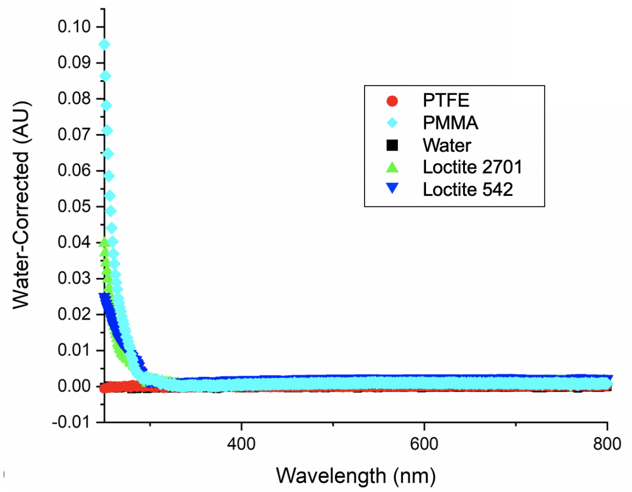

Figure 6.29: Optical transmission measurements as a function of wavelength across the UV-VIS spectrum, for different diffusing and sealant materials.

are in its difficulty in manufacturing and porous nature, which in turn require the use of a water-tight enclosure. There has since been a push to find new potential diffusing materials; one candidate is poly-tetrafluoroethylene, otherwise known as PTFE or Teflon.

Virgin PTFE is renowned for its excellent chemical and water resistant properties [158]. Soak tests in ultra-pure and gadolinium loaded water sample are in progress with preliminary results indicating no visible leeching into the water solutions. If successful, and the transmission properties of water exposed PTFE diffuser are unchanged, the need for a water-tight diffuser enclosure is put into question. Nevertheless, studies have demonstrated the enhancements to optical profiles that enclosures may potentially provide (section 6.6.3). Moreover, a water-tight enclosure may be used to ensure longevity on the scale of multiple decades.

The proposed optical calibration system for Hyper-K requires the diffusing material to have good transmission properties over the UV-VIS spectrum from approximately 300 nm to 500 nm. The optical transmission of PMMA and PTFE using a Shimadzu UV-2600 spectrometer is shown in figure 6.29. Each measurement is corrected to a water control to eliminate any water band features. A value of zero indicates the same transmittance as water, which is ideal for the calibration optics. It can be seen that both PMMA and PTFE perform well at wavelengths across the UV-VIS spectrum. However below approximately 350 nm, PTFE retains its transmittance, whilst PMMA begins to absorb more light, indicating that PTFE performs as good, if not better, than PMMA over the full UV-VIS spectrum.

The manufacturing process of PMMA, as described in section 6.3.3, is not ideal and has proved problematic in scaling up to mass production. PTFE rods can be purchased directly from industrial manufacturers. The only in-house manufacturing needed after this stage is crafting the hemispherical diffusers. Each 1 m PTFE rod can be manufactured into an estimated 30 to 40 diffuser balls, compared to 2 to 3 diffusers from each 100 mm rod of PMMA. This results in a reduction in material costs of 65%, and an even larger saving in labour costs as the sintered rods are no longer manufactured in-house. Furthermore, PMMA is extremely porous and requires machining tools to be scrupulously cleaned of oils, suds, and other containments beforehand. PTFE by nature is more impermeable, meaning less cleaning is needed before machining.

6.6.2 PTFE Optical Performance

In a review process, diffusers made out of PTFE must pass all of the optical and temporal performance tests that their PMMA counterparts had passed previously. Any major issues can then be highlighted, advantages and disadvantages discussed, before any decisions are made.

The optical light profiles of bare PMMA and PTFE diffusers are shown in figure 6.30. It can be seen that the PTFE relative light intensity profile is comparable to PMMA with a marginally narrower distribution. The magnitude of light emitted is larger for the PTFE diffusers with approximately 15% more light emitted in the forward going region (figure B.7). A comparison of the pulse delay, shown in figure B.8, demonstrates PTFE has the same uniform timing profile as PMMA. Together the temporal and light intensity profiles suggest the performance of PTFE as a diffuse calibration device is similar to PMMA. Further investigations into PTFE batch reproducibility and pressure testing are currently in progress before any final decisions are made about the diffusing material moving forward.

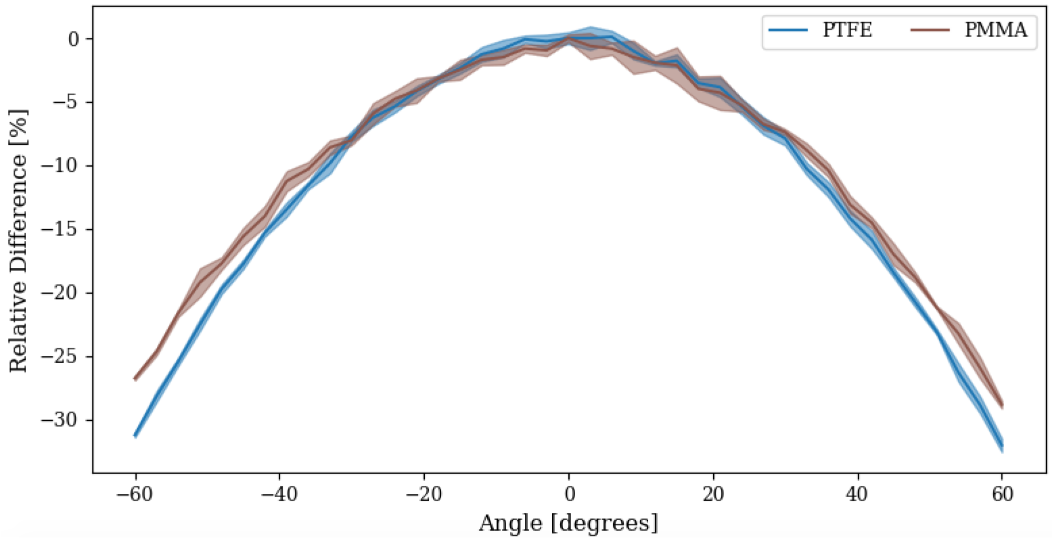

Figure 6.30: A comparison of the relative light intensity profiles, normalised to 0°, for bare PMMA and PTFE diffusers.

6.6.3 Enclosure Development

Post Super-K deployment reviews highlighted particular flaws in the V3 enclosure design. The most significant problem, as section 6.4.4 has already alluded to, is the measures used to waterproof the enclosure. Studies had shown that the Vitron o-ring gaskets had performed well in enclosures V1 and V3. However, sealing the fibre feed-through point in the back of the enclosure was extremely problematic. Epoxy resin did not bond well with the PVC fibre furcation tubing, and had to be applied liberally around the entire enclosure. Application of epoxy resin made assembly of enclosure V3 intricate and not feasible on the large scale mass production needed for Hyper-K. The philosophy was to turn to mechanical waterproofing and create a new enclosure design aimed towards large scale mass production.

V4 Enclosure

A schematic diagram of enclosure V4 is shown in figure 6.31, along with a photograph of the fully assembled front of the enclosure. Similar to the previous designs, enclosure V4 consists of three cylindrical segments. The individually threaded segments used for assembly has been replaced by six long bolts that feed-through the entire design. Three o-ring gaskets, one either side of the window, and one between the main

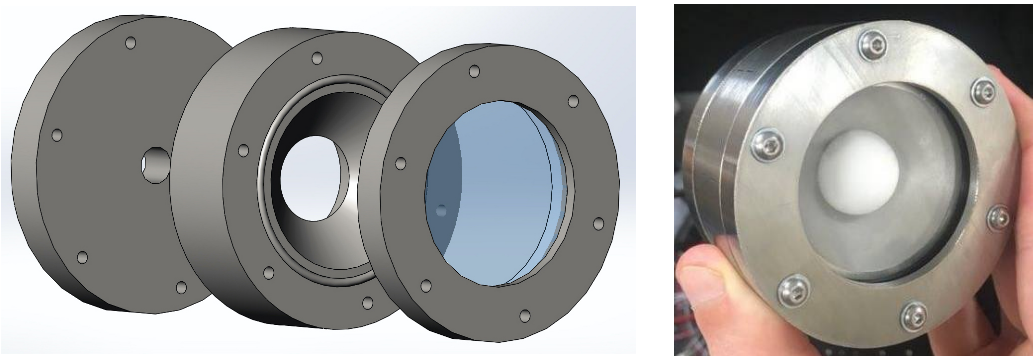

(a) (b)

Figure 6.31: (a) A schematic CAD drawing of the V4 enclosure. (b) A front facing photo of enclosure V4, fully assembled with a sand-blasted stainless steel torch surface.

body and base, are quashed when the bolts are tightened providing mechanical watertight seals. Replacing the epoxy resin, preliminary concepts for fibre feed-through waterproofing use screw in fibre ports with a thread sealant. Studies are in progress to pressure test the enclosure up to 10 bar, with further development expected for future water Cherenkov detector experiments such as Hyper-K.

Surface Treatments

When considering internal enclosure reflections, a distinction should be made between specular and diffuse reflections. Specular reflections are often unwanted as they strongly bias the light output in a particular direction. However, diffuse reflections scatter incident light rays at many different angles during reflection. Different surface treatments to the internal design of the enclosure have been tested to compare the various effects on the outgoing light profile. All tests were performed using a V4 enclosure design, which is shown in figure 6.31. Each enclosure was made out of 304 stainless steel, except for the 3D printed enclosure which was made out of a carbon fibre based composite material. A measurement of untreated stainless steel was used as a control, and then the internal torch base was painted matte black and white. The torch was then sandblasted to finely roughen the surface, the previous treatments were then applied, and measurement retaken. The resultant light profiles using a standard PMMA diffuser are shown in figure 6.32. The results indicate a

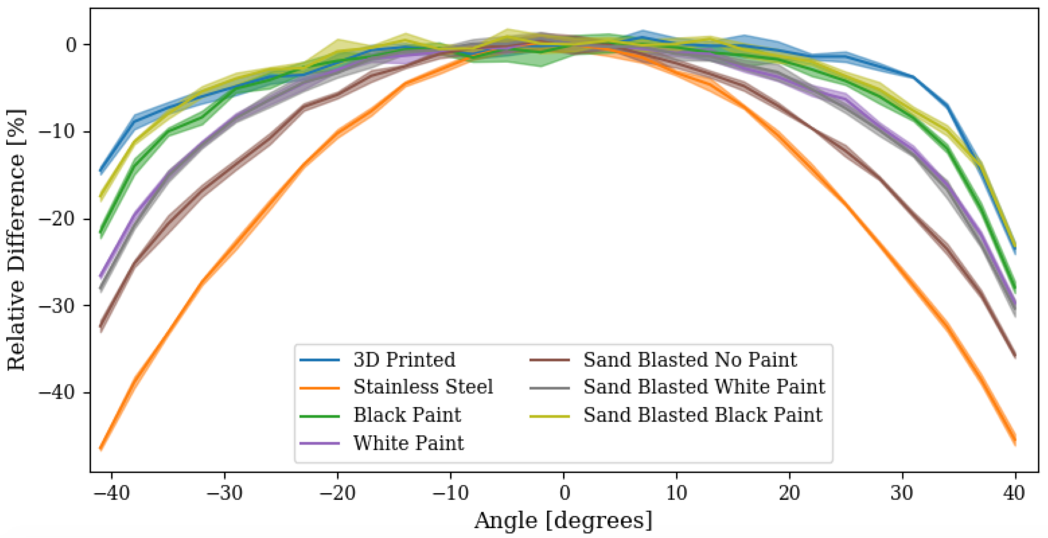

Figure 6.32: The relative light profiles, normalised to 0°, for the PMMA diffuser inside enclosure V4 for different surface treatments of the torch.

correlation between the surface treatments and the uniformity of light profiles within the enclosure field of view. In particular, smoother metallic treatments were found to encourage specular reflections and increase the forward going light output. Sand blasting has the affect of roughening the surface and replacing potential specular reflections with their diffuse counterparts. Painting the surface with a matte black paint effectively removes most reflections. Perhaps interestingly, painting with matte white paint acts as a mid ground between sand blasting and painting black. The absolute intensities are also shown in figure 6.33, here it is more trivial to conclude which surfaces are promoting and inhibiting internal enclosure reflections. Matte black paint is found to reduce the pulse intensity, whilst painting white appears to increase the overall pulse intensity integrated over all angular space.

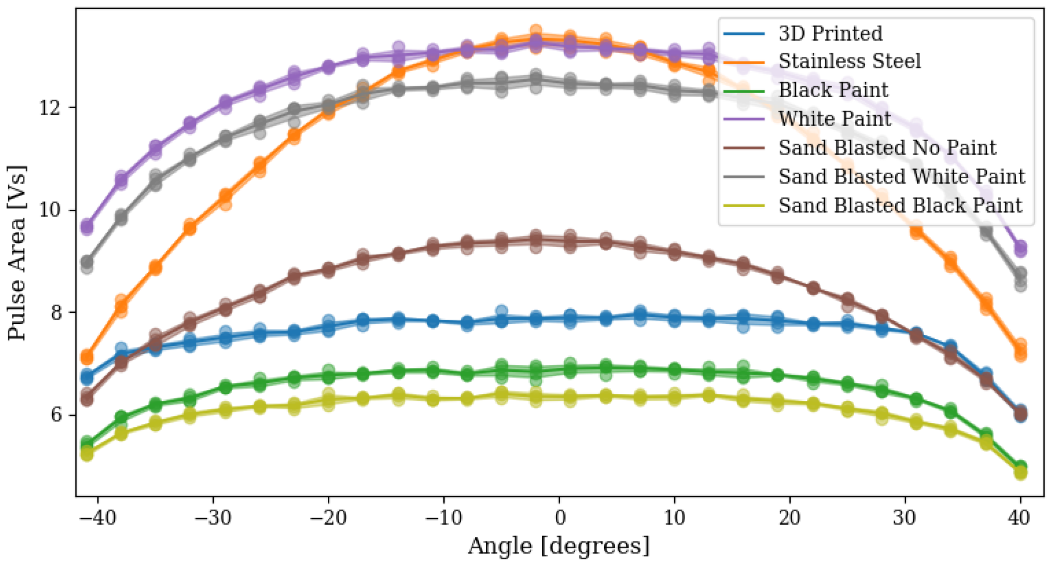

Figure 6.33: The pulse area as a function of angle for the PMMA diffuser inside enclosure V4 for different surface treatments of the torch.

Chapter 7

Summary and Closing Remarks

In this thesis the topic of neutrino physics has been introduced, with an emphasis on neutrino-nucleus interactions, and how cross-section measurements can help with an overarching goal of measuring key neutrino oscillation parameters. A brief history of neutrinos has been explored, from their discovery through to modern day neutrino oscillation experiments. Chapter 3 outlined a detailed description of the T2K experiment, including a discussion of the ND280 near detector which has subsequently been used to measure the ν_e CC π^+ cross-section in chapter 4. Proposals for the Hyper-Kamiokande experiment, the next generation water Cherenkov detector from Super-Kamiokande, were introduced in chapter 5. Finally, the optical calibration system, as well as diffuser research and development for the Hyper-K detector were examined. This closing chapter will summarise both the T2K cross-section analysis, and Hyper-K diffuser calibration studies, reviewing the results, and proposing potential avenues for future research.

7.1 ν_e CC π^+ Cross Section Analysis Summary

A selection has been developed to analyse post-FSI π^+ production from charged current electron neutrino interactions in ND280. The lepton selection inherits from the CC-ν_e inclusive analysis, and includes an additional new π^+ selection. Out of fiducial volume photon background, prevalent in the CC-ν_e inclusive analysis, is significantly reduced through pion selection. Photon backgrounds from ν_μ CC π^0

and neutral current interactions are the predominant source of background in the forward going low lepton momenta regions; backgrounds from muon interactions dominate in higher lepton momentum regions. A signal purity of 51.1% is selected at an efficiency of 25.4% over the full selection with phase space constraints applied. Systematic uncertainties on detector effects, cross-section model parameters, and flux have been calculated for their relative effects on both background event yields and signal efficiencies. The flux integrated cross-section, over one bin in momenta space, was measured to be $(2.23 \pm 0.18 \text{ (stat.)} \pm 0.31 \text{ (syst.)}) \times 10^{-39}$ cm^2 per nucleon. This is the first measurement of the ν_e CC π^+ cross-section on a carbon target ever made. The result agrees with nominal NEUT 5.4.0 MC, within both statistical and systematic errors. Finally, a region of low momenta phase space was defined analogous to the Super-K FHC 1 decay electron sample that observes an excess in π^+ production. Data-MC comparisons within this region give preliminary indications that no excess is seen at the near detector, and is the beginning to providing a constraint on the far detector process.

Whilst achieving preliminary results, further investigations could be made to help understand the interaction process at the near detector. Firstly, time constraints limited model comparisons to nominal NEUT predictions only. A more complete study should compare results to other neutrino event generator predictions, such as GENIE and NuWro. Resonant pion production in NEUT is described, at an invariant mass $W \leq 2$ GeV/c^2, using the Rein-Seghal model [46], with a resonant axial mass set to 0.95 GeV/c^2. Deep inelastic scattering is modelled using the GRV98 parton distribution function [159], including the Bodak and Yang corrections [160], for $W \geq 1.3$ GeV/c^2. GENIE has very similar treatments to NEUT for resonant pion production and DIS processes, but uses a resonant axial mass of 1.12 GeV/c^2 and a slightly different Bodak and Yang correction respectively. Resonances are also switched off in GENIE above $W > 1.7$ GeV/c^2 to avoid double counting with DIS. A comparison against NuWro would be interesting given it's different treatment of resonant pion production; A single Δ-model by Adler-Rarita-Schwinger [161] is used with an axial mass term of 0.94 GeV/c^2 at $W < 1.6$ GeV/c^2. A smooth transition from resonance to DIS processes then takes place from hadronic masses of 1.3 GeV/c^2

to 1.6 GeV/c^2. Comparisons of data against multiple neutrino event generators provides a measure of testing the performance of these different interaction models. These studies were not able to be performed within the thesis time scale, but provide suggestions for the analysis moving forward.

Multiple improvements to the analysis could be made in the future. One suggestion would be to perform a multivariate analysis on the systematic uncertainties to study the interplay and correlations between individual systematics, which is not yet considered. Furthermore, the cross-section measurement was performed using a zeroth-order calculation. A likelihood fit package, such as nueXsLLFitter used in the CC-ν_e inclusive measurement, allows for more sophisticated error propagation and cross-section extraction. Multi-bin measurements of the cross-section over different areas of phase space would be possible with a likelihood fitter. The cross-sections of ν_μ and ν_e should be similar at higher energies, and so it is more interesting to investigate the low Q^2 regions of phase space. The analysis could also be expanded to include RHC data runs, FHC runs 9-10, and FGD2 interactions thereby increasing statistics. Limitations of the analysis include it's preference to forward going events, and criterion for tracks to leave the FGD and enter the TPC. Finally, multiple efforts have seen recent T2K ν_μ analyses attempt to measure over a 4π angular coverage [162], and include isolated FGD pions [163]. One could in theory extend these ideas to ν_e analyses in the future.

7.2 Diffuser Systems For Optical Calibration

Proposals for a light injection system to optically calibrate water Cherenkov detectors such as Hyper-Kamiokande are underway. The proposed system uses two optical calibration devices: A wide beam diffuser for PMT energy and timing calibration, and a narrow beam collimator for monitoring water properties. This thesis focussed on the research and development of diffuser technology. A principle bare diffuser has been designed with a well understood light and uniform timing, profile over a wide angular coverage, from $-60^\circ \rightarrow 60^\circ$. The diffusers are made out of PMMA and are held in a water-tight stainless steel enclosure. Not only have the principal designs have been demonstrated to work under laboratory conditions, but have also twice been successfully deployed in the Super-Kamiokande detector. Preliminary qualitative analyses have indicated that the diffusers are working as expected.

A full quantitative analysis on the Super-K deployment, based on the diffuser performance and the subsequent calibration potential has begun, and will heavily influence future research and development. A post-deployment external review identified potential weaknesses in the diffuser design. Two key areas identified were the waterproofing measures, and scalability for mass production. Bonding between epoxy resin and fibre furcation tubing was poor, with ad-hoc strain relief accessories needed to mitigate against failures under pressure. Furthermore, the liberal application of epoxy resin and intricate assembly of the diffuser enclosures are problematic when scaling towards mass production. Development of diffuser enclosures V4 and above need to ensure systematic water-tightness under pressure; the design philosophy has moved to mechanical seals, which are known to work through previous enclosure body pressure tests. Screw in fibre ports with a thread sealant, will provide a mechanical watertight seal at the fibre feedthrough point. The porous nature of PMMA has also led to a search for alternative diffuser materials; PTFE has been highlighted as a potential candidate due to it's water and chemical resistant properties. Investigations into PTFE as a diffusing material, and it's comparative performance against PMMA, are underway with preliminary results suggesting similar diffusing characteristics. PTFE also provides an easier means to machining, and scaling to mass production. Upgrades are planned for the experimental setup outlined in section 6.2. The light injection system is to be upgraded with a pulsed laser, which will allow for accurate laser power monitoring. The upgraded test system will also allow for 2-dimensional diffuser scans, providing a more complete mapping of the diffuser light profile.

The optical calibration diffuser work presented in this thesis demonstrates a successful diffuse light injection system for PMT energy and timing calibrations. With further research and development planned the diffuser system has been proposed for installation in Hyper-Kamiokande, and has the potential to be adapted for installations in other water Cherenkov detectors.

Appendix A

T2K Analysis Appendix

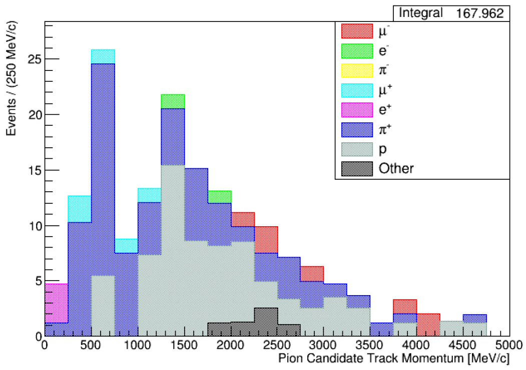

(a)

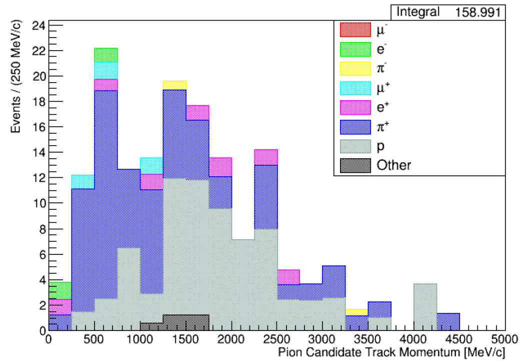

(b)

Figure A.1: A histogram demonstrating the true particle selected for the pion candidate track, as a function of the track's reconstructed momentum. The ν_μ CC photon background topology is isolated on the left, the NC photon background topology on the right.

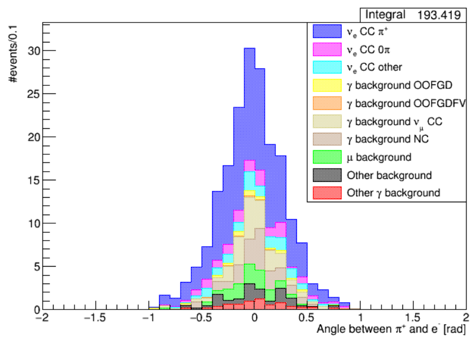

(a)

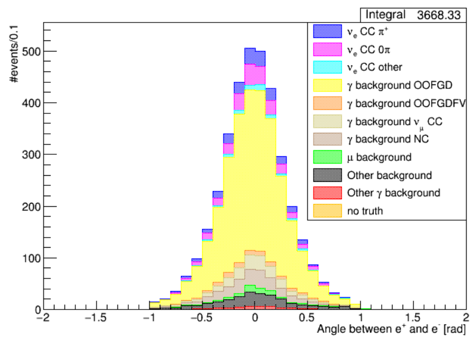

(b)

Figure A.2: The angle between the two selected tracks for (a) e^- and π^+ in the ν_e CC π^+ selection sample, and (b) the e^+e^- pair in the vertexing systematic sample.

Sample	PoT	NSpills	Nbunches	NECal	ECal/bunch (%)
Run 2 - Water Out					
Data	3.59337e+19	423187	3385496	562888	16.6265
MC	1.6794e+21	1.97781e+07	1.58225e+08	1.91209e+07	12.0846
Sand	7.05023e+20	8.30297e+06	6.64237e+07	2.81367e+06	4.23594
Run 2 - Water In					
Data	4.33934e+19	598617	4788936	689265	14.3929
MC	1.20375e+21	1.66058e+07	1.32847e+08	1.38547e+07	10.4291
Sand	7.05023e+20	9.72588e+06	7.7807e+07	2.81367e+06	3.61622
Run 3b - Water Out					
Data	2.17273e+19	260193	2081544	315907	15.1766
MC	3.07766e+21	3.68563e+07	2.9485e+08	3.46192e+07	11.7413
Sand	7.05023e+20	8.44295e+06	6.75436e+07	2.81367e+06	4.16571
Run 3c - Water Out					
Data	1.36447e+20	1480300	11842400	2.14796e+06	18.1378
MC	3.07766e+21	3.33893e+07	2.67114e+08	3.46192e+07	12.9605
Sand	7.05023e+20	7.64874e+06	6.119e+07	2.81367e+06	4.59826
Run 4 - Water Out					
Data	1.78319e+20	1529336	12234688	2.74962e+06	22.4739
MC	3.41282e+21	2.92697e+07	2.34157e+08	3.83982e+07	16.3985
Sand	7.05023e+20	6.04656e+06	4.83725e+07	2.81367e+06	5.81668
Run 4 - Water In					
Data	1.64228e+20	1600804	12806432	2.58112e+06	20.1549
MC	3.61215e+21	3.52091e+07	2.81673e+08	4.10491e+07	14.5733
Sand	7.05023e+20	6.87216e+06	5.49773e+07	2.81367e+06	5.11788
Run 8 - Water Out					
Data	4.15013e+20	1766203	14129624	5.61527e+06	39.7411
MC	3.61002e+21	1.53634e+07	1.22908e+08	3.68835e+07	30.0092
Sand	7.05023e+20	3.00042e+06	2.40034e+07	2.81367e+06	11.722
Run 8 - Water In					
Data	1.58053e+20	778207	6225656	2.18188e+06	35.0465
MC	2.71677e+21	1.33766e+07	1.07013e+08	2.8016e+07	26.18
Sand	7.05023e+20	3.47133e+06	2.77707e+07	2.81367e+06	10.1318

Table A.1: Table showing the numbers used to evaluate the correction and systematic uncertainty for ECal pileup affecting FGD1 target selections.

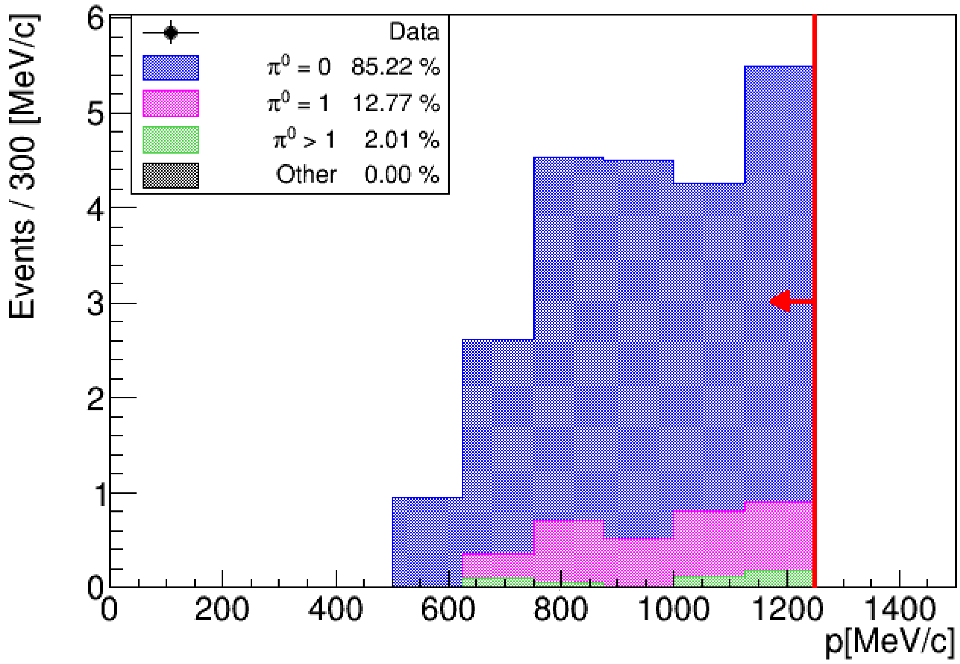

Figure A.3: The number of π^0 particles present in the ν_e CC π^+ signal sample at low momentum regions comparable to Super-K.

Appendix B

Hyper-K Analysis Appendix

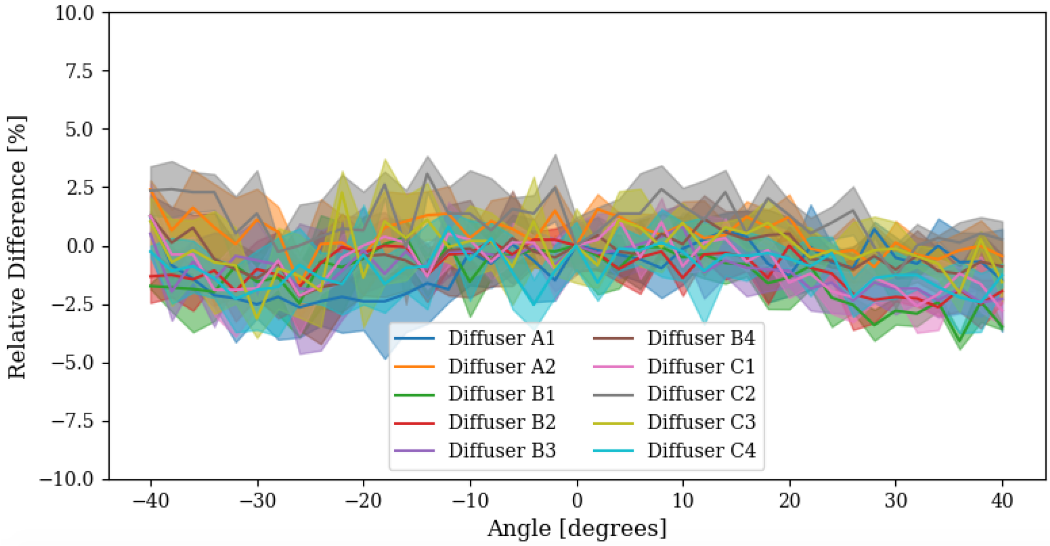

Figure B.1: The relative full width half maximum of the signal pulse, normalised to zero degrees, for PMMA bare diffusers.

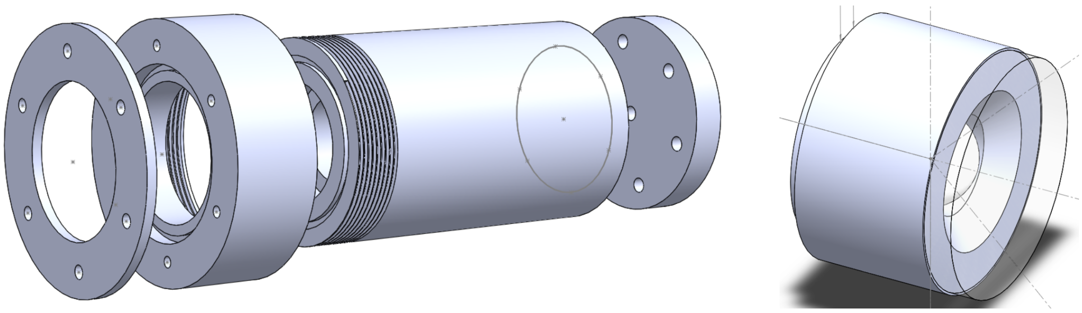

(a) (b)

Figure B.2: The intermediate conceptual enclosure designs between V1 and V3. (a) V2 consisted the long main body that was prominent in V1 in combination with the threaded screw design seen in V3. (b) V2a was a singular enclosure design smaller than previous, with a torch-like design at the front. Neither V2 or V2a made it to production.

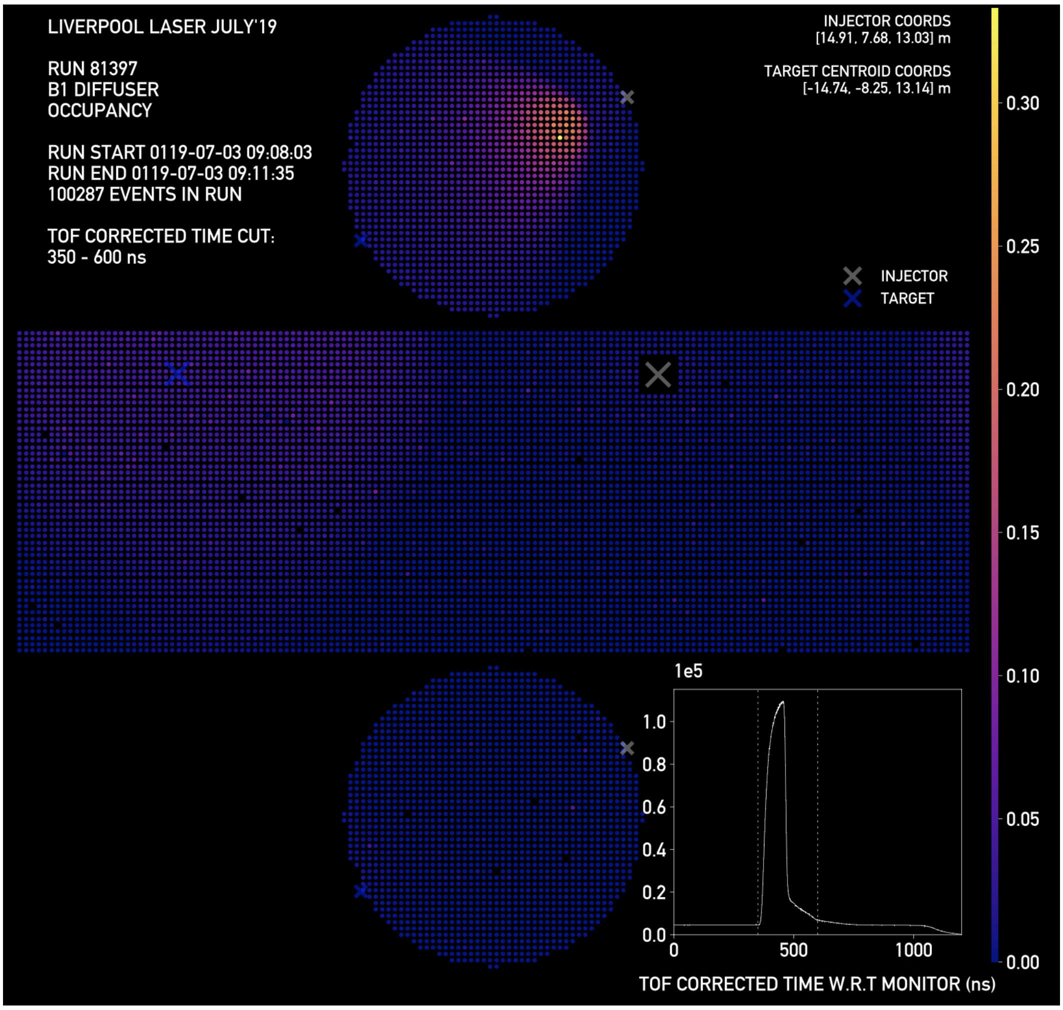

Figure B.3: An example PMT hit occupancy event display for diffuser installed at the B1 injection point over the full detector. The time of flight corrected hits as a function of time is shown on bottom right. Plot modified from [157].

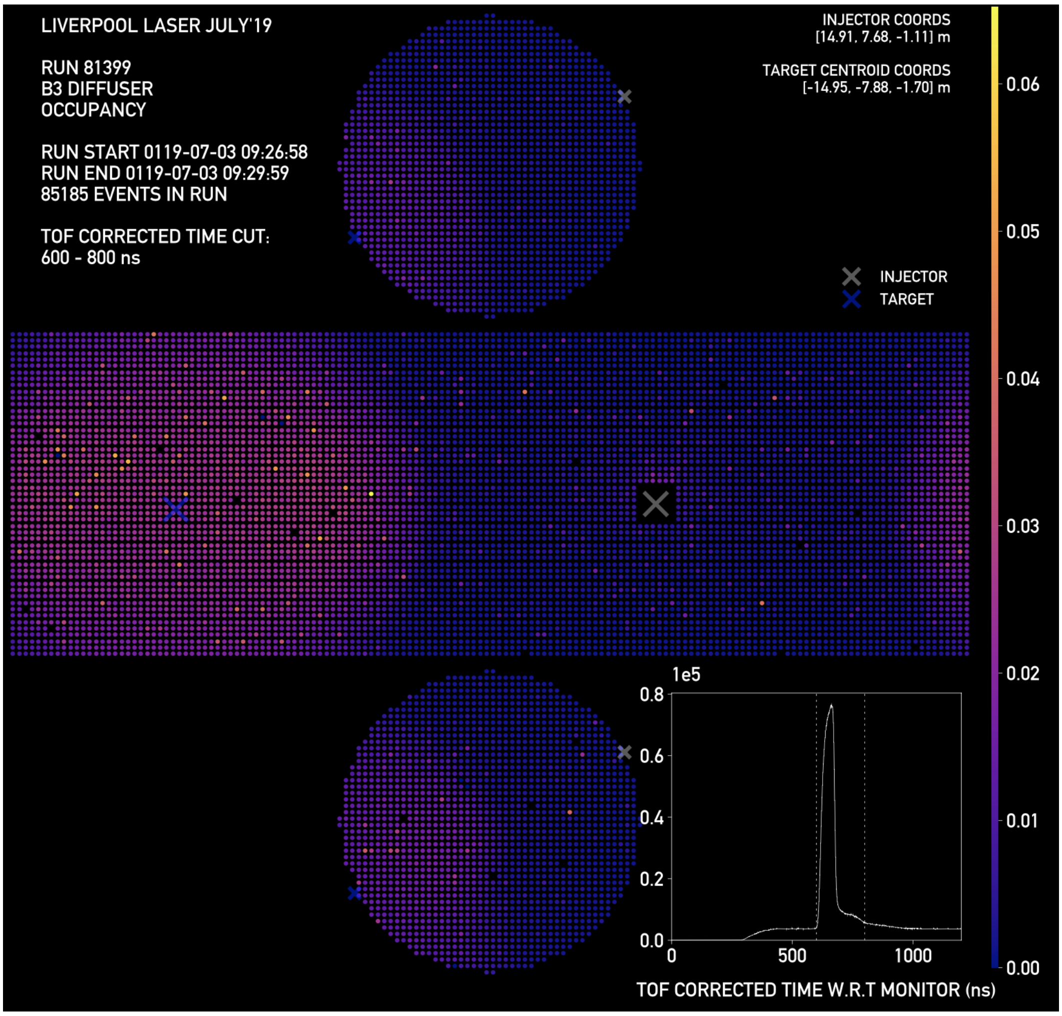

Figure B.4: An example PMT hit occupancy event display for diffuser installed at the B3 injection point over the full detector. The time of flight corrected hits as a function of time is shown on bottom right. Plot modified from [157].

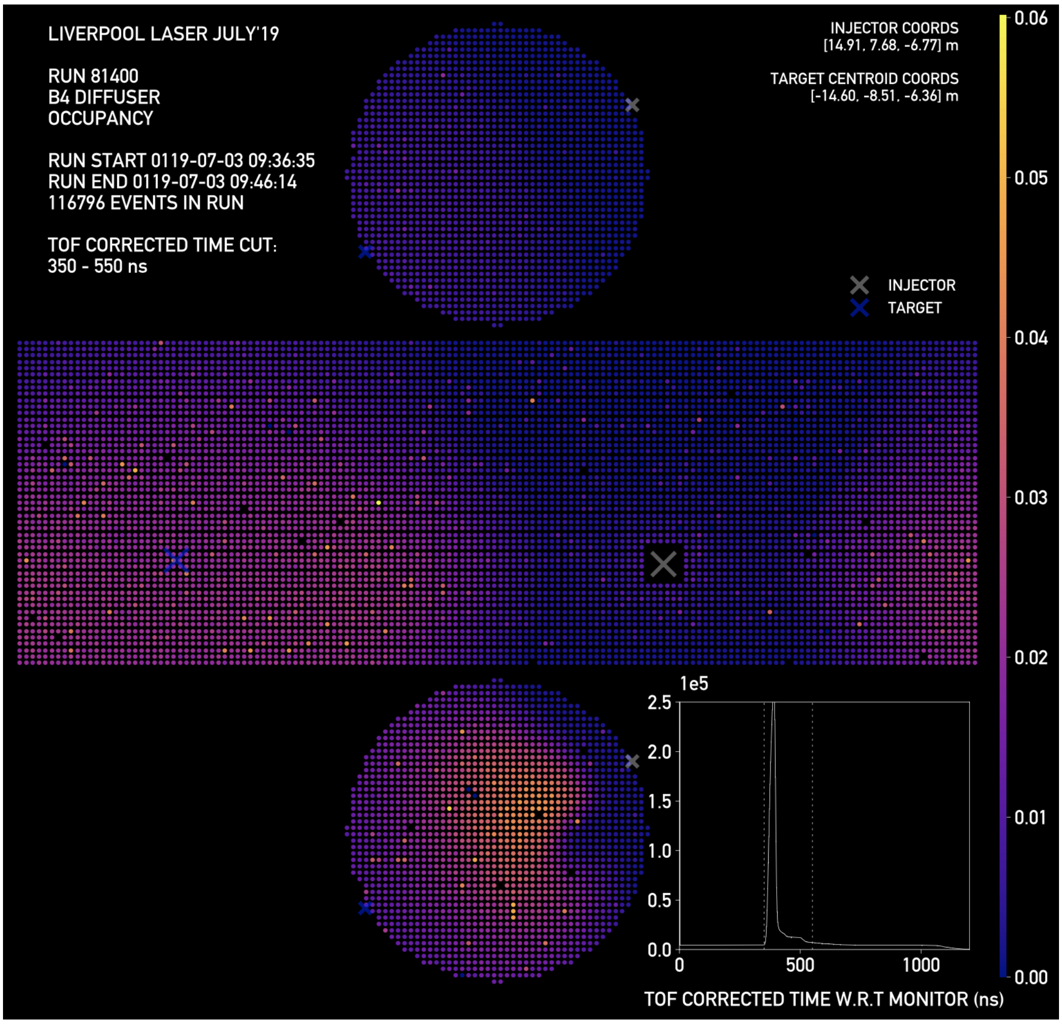

Figure B.5: An example PMT hit occupancy event display for diffuser installed at the B4 injection point over the full detector. The time of flight corrected hits as a function of time is shown on bottom right. Plot modified from [157].

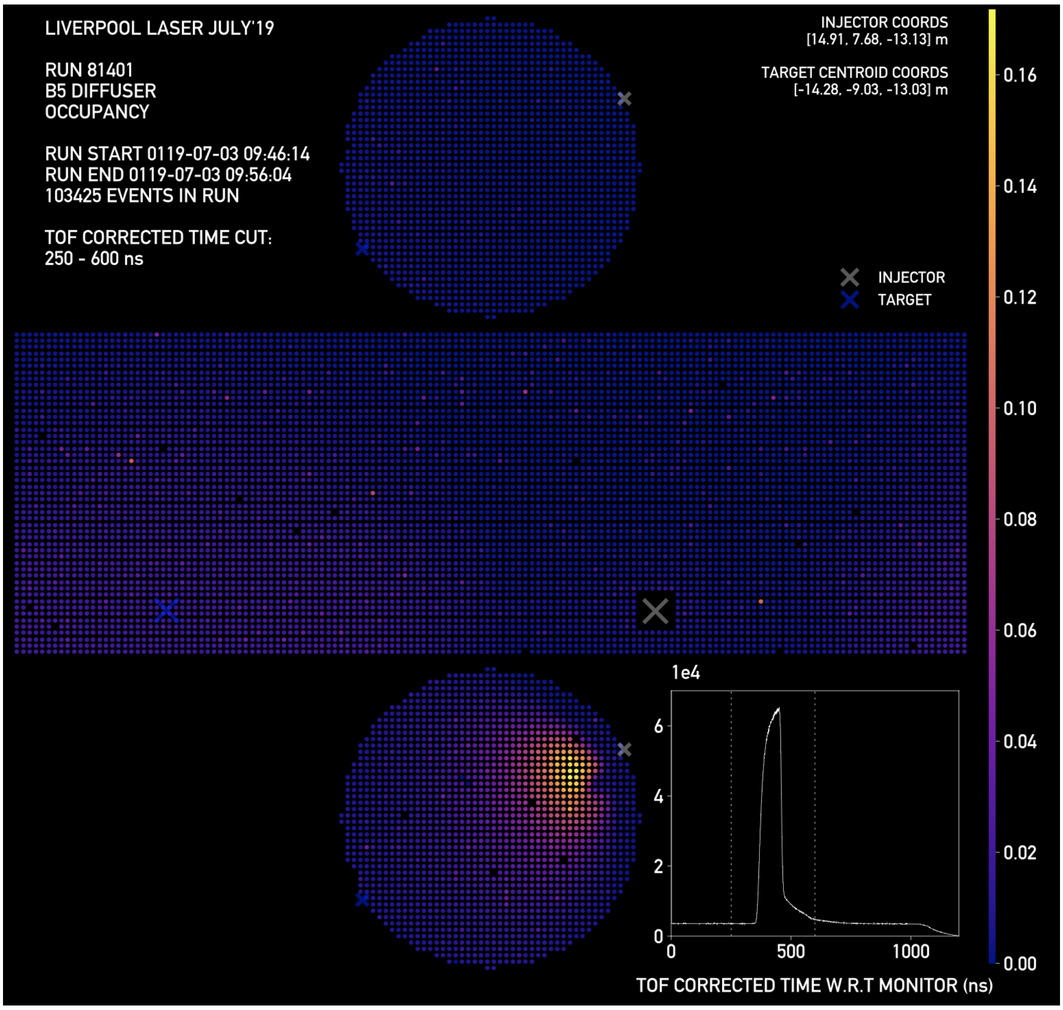

Figure B.6: An example PMT hit occupancy event display for diffuser installed at the B5 injection point over the full detector. The time of flight corrected hits as a function of time is shown on bottom right. Plot modified from [157].

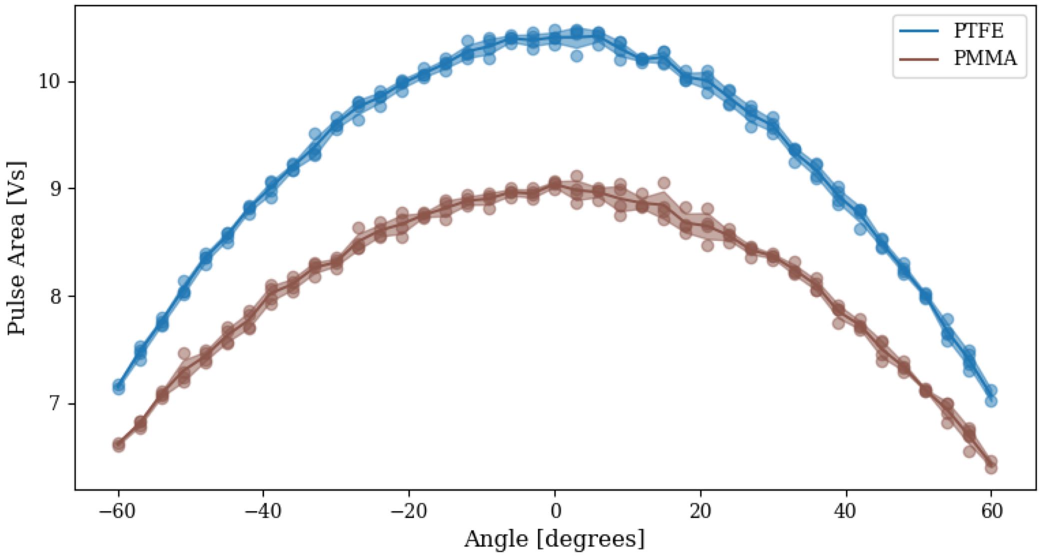

Figure B.7: A comparison of the pulse area as a function of angle for bare PMMA and PTFE diffusers.

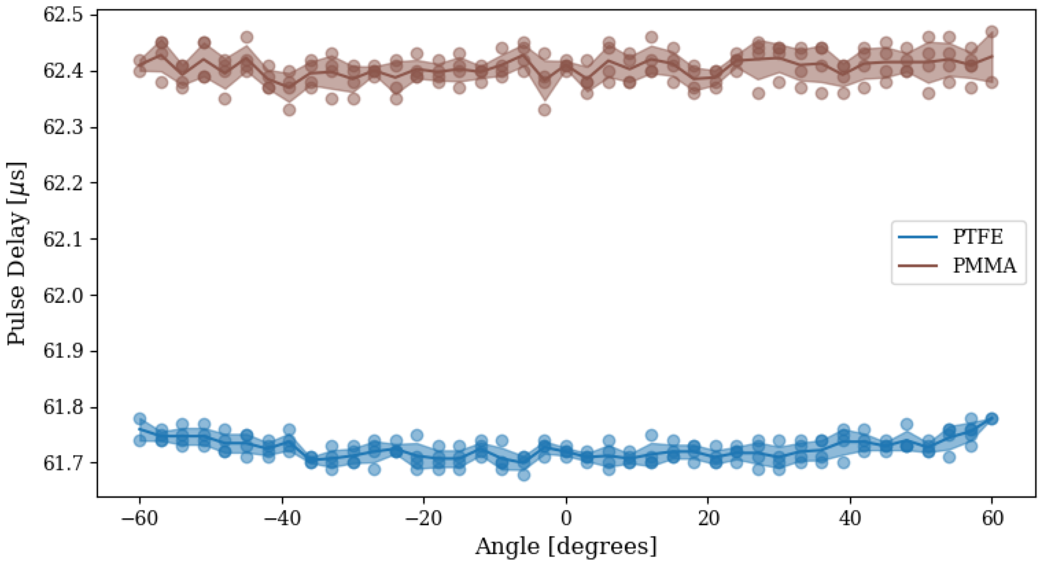

Figure B.8: A comparison of the pulse delay as a function of angle for bare PMMA and PTFE diffusers.

Bibliography

[1] M. Tanabashi, K. Hagiwara, K. Hikasa, K. Nakamura, Y. Sumino, F. Takahashi, J. Tanaka, K. Agashe, G. Aielli, C. Amsler, *et al.*, "Review of particle physics," *Physical Review D*, vol. 98, no. 3, p. 030001, 2018.

[2] I. Esteban, "Nufit webpage." `http://www.nu-fit.org`, June 2017. Accessed: March 2020.

[3] I. Esteban, M. Gonzalez-Garcia, A. Hernandez-Cabezudo, M. Maltoni, and T. Schwetz, "Global analysis of three-flavour neutrino oscillations: Synergies and tensions in the determination of θ 23, δ cp, and the mass ordering," *Journal of High Energy Physics*, vol. 2019, no. 1, pp. 1–35, 2019.

[4] K. Abe, C. Bronner, Y. Haga, Y. Hayato, M. Ikeda, K. Iyogi, J. Kameda, Y. Kato, Y. Kishimoto, L. Marti, *et al.*, "Atmospheric neutrino oscillation analysis with external constraints in super-kamiokande i-iv," *Physical Review D*, vol. 97, no. 7, p. 072001, 2018.

[5] K. Eguchi, S. Enomoto, K. Furuno, J. Goldman, H. Hanada, H. Ikeda, K. Ikeda, K. Inoue, K. Ishihara, W. Itoh, *et al.*, "First results from kamland: evidence for reactor antineutrino disappearance," *Physical Review Letters*, vol. 90, no. 2, p. 021802, 2003.

[6] G. W. Rodeback and J. S. Allen, "Neutrino recoils following the capture of orbital electrons in a 37," *Physical Review*, vol. 86, no. 4, p. 446, 1952.

[7] F. Reines and C. Cowan Jr, "Detection of the free neutrino," *Physical Review*, vol. 92, no. 3, p. 830, 1953.

[8] C. Cowan, F. Reines, H. Kruse, and A. McGuire, “Detection of the free neutrino: Confirmation,” 1956.

[9] G. Danby, J. Gaillard, K. Goulianos, L. Lederman, N. Mistry, M. Schwartz, and J. Steinberger, “Observation of high-energy neutrino reactions and the existence of two kinds of neutrinos,” *Physical Review Letters*, vol. 9, no. 1, p. 36, 1962.

[10] D. Decamp, B. Deschizeaux, J.-P. Lees, M.-N. Minard, J. Crespo, M. Delfino, E. Fernandez, M. Martinez, R. Miquel, M. Mir, *et al.*, “Determination of the number of light neutrino species,” *Physics Letters B*, vol. 231, no. 4, pp. 519–529, 1989.

[11] K. Kodama, N. Ushida, C. Andreopoulos, N. Saoulidou, G. Tzanakos, P. Yager, B. Baller, D. Boehnlein, W. Freeman, B. Lundberg, *et al.*, “Observation of tau neutrino interactions,” *Physics Letters B*, vol. 504, no. 3, pp. 218–224, 2001.

[12] F. Close, *Neutrino*. Oxford University Press, 2012.

[13] R. Davis, “A review of the homestake solar neutrino experiment,” *Progress in Particle and Nuclear Physics*, vol. 32, pp. 13–32, 1994.

[14] R. Stoenner, O. Schaeffer, and S. Katcoff, “Half-lives of argon-37, argon-39, and argon-42,” *Science*, vol. 148, no. 3675, pp. 1325–1328, 1965.

[15] W. Hampel, J. Handt, G. Heusser, J. Kiko, T. Kirsten, M. Laubenstein, E. Pernicka, W. Rau, M. Wojcik, Y. Zakharov, *et al.*, “Gallex solar neutrino observations: Results for gallex iv,” *Physics Letters B*, vol. 447, no. 1-2, pp. 127–133, 1999.

[16] J. Abdurashitov, E. Faizov, V. Gavrin, A. Gusev, A. Kalikhov, T. Knodel, I. Knyshenko, V. Kornoukhov, I. Mirmov, A. Pshukov, *et al.*, “Results from sage (the russian-american gallium solar neutrino experiment),” *Physics Letters B*, vol. 328, no. 1-2, pp. 234–248, 1994.

[17] A. Bellerive, J. Klein, A. McDonald, A. Noble, A. Poon, S. Collaboration, *et al.*, "The sudbury neutrino observatory," *Nuclear Physics B*, vol. 908, pp. 30–51, 2016.

[18] Y. Fukuda, T. Hayakawa, E. Ichihara, K. Inoue, K. Ishihara, H. Ishino, Y. Itow, T. Kajita, J. Kameda, S. Kasuga, *et al.*, "Measurement of the flux and zenith-angle distribution of upward throughgoing muons by super-kamiokande," *Physical Review Letters*, vol. 82, no. 13, p. 2644, 1999.

[19] Q. R. Ahmad, R. Allen, T. Andersen, J. Anglin, J. Barton, E. Beier, M. Bercovitch, J. Bigu, S. Biller, R. Black, *et al.*, "Direct evidence for neutrino flavor transformation from neutral-current interactions in the sudbury neutrino observatory," *Physical review letters*, vol. 89, no. 1, p. 011301, 2002.

[20] S. collaboration *et al.*, "Direct evidence for neutrino flavor transformation from neutral-current interactions in the sudbury neutrino observatory," *arXiv preprint nucl-ex/0204008*, 2002.

[21] C. Athanassopoulos, L. Auerbach, R. Burman, I. Cohen, D. Caldwell, B. Dieterle, J. Donahue, A. Eisner, A. Fazely, F. Federspiel, *et al.*, "Evidence for ν $\mu\rightarrow$ ν e oscillations from the lsnd experiment at the los alamos meson physics facility," *Physical Review Letters*, vol. 77, no. 15, p. 3082, 1996.

[22] C. Athanassopoulos, L. Auerbach, R. Burman, D. Caldwell, E. Church, I. Cohen, J. Donahue, A. Fazely, F. Federspiel, G. Garvey, *et al.*, "Results on ν $\mu\rightarrow$ ν e neutrino oscillations from the lsnd experiment," *Physical Review Letters*, vol. 81, no. 9, p. 1774, 1998.

[23] M. Acciarri, O. Adriani, M. Aguilar-Benitez, S. Ahlen, J. Alcaraz, G. Alemanni, J. Allaby, A. Aloisio, M. Alviggi, G. Ambrosi, *et al.*, "Determination of the number of light neutrino species from single photon production at lep," *Physics Letters B*, vol. 431, no. 1-2, pp. 199–208, 1998.

[24] A. Aguilar-Arevalo, A. Bazarko, S. Brice, B. Brown, L. Bugel, J. Cao, L. Coney, J. Conrad, D. Cox, A. Curioni, *et al.*, "Search for electron neutrino appearance

at the δ m 2 1 ev 2 scale," *Physical review letters*, vol. 98, no. 23, p. 231801, 2007.

[25] A. Aguilar-Arevalo, C. Anderson, A. Bazarko, S. Brice, B. Brown, L. Bugel, J. Cao, L. Coney, J. Conrad, D. Cox, *et al.*, "Unexplained excess of electronlike events from a 1-gev neutrino beam," *Physical review letters*, vol. 102, no. 10, p. 101802, 2009.

[26] A. Aguilar-Arevalo, C. Anderson, S. Brice, B. Brown, L. Bugel, J. Conrad, Z. Djurcic, B. Fleming, R. Ford, F. Garcia, *et al.*, "Search for electron antineutrino appearance at the δ m 2 1 ev 2 scale," *Physical review letters*, vol. 103, no. 11, p. 111801, 2009.

[27] T. Gershon, "Overview of the cabibbo–kobayashi–maskawa matrix," *Pramana*, vol. 79, no. 5, pp. 1091–1108, 2012.

[28] F. J. Gilman and M. B. Wise, "Strong interaction corrections to k0-k0 mixing in the six quark model," *Physics Letters B*, vol. 93, no. 1-2, pp. 129–133, 1980.

[29] K. Zuber, *Neutrino physics*. CRC press, 2011.

[30] B. Kayser, "On the quantum mechanics of neutrino oscillation," *Physical Review D*, vol. 24, no. 1, p. 110, 1981.

[31] W. Grimus and P. Stockinger, "Real oscillations of virtual neutrinos," *Physical Review D*, vol. 54, no. 5, p. 3414, 1996.

[32] C.-S. Wu, E. Ambler, R. Hayward, D. Hoppes, and R. P. Hudson, "Experimental test of parity conservation in beta decay," *Physical review*, vol. 105, no. 4, p. 1413, 1957.

[33] G. D. Barr, P. Buchholz, R. Carosi, D. Coward, D. Cundy, N. Doble, L. Gatignon, V. Gibson, P. Grafström, R. Hagelberg, *et al.*, "A new measurement of direct cp violation in the neutral kaon system," *Physics Letters B*, vol. 317, no. 1-2, pp. 233–242, 1993.

[34] V. Fanti, A. Lai, D. Marras, L. Musa, A. Bevan, T. Gershon, B. Hay, R. Moore, K. Moore, D. Munday, *et al.*, “A new measurement of direct cp violation in two pion decays of the neutral kaon,” *Physics Letters B*, vol. 465, no. 1-4, pp. 335–348, 1999.

[35] P. de Salas, D. Forero, C. Ternes, M. Tortola, and J. Valle, “Status of neutrino oscillations 2018: 3σ hint for normal mass ordering and improved cp sensitivity,” *Physics Letters B*, vol. 782, pp. 633–640, 2018.

[36] S. K. Agarwalla, S. Prakash, and W. Wang, “High-precision measurement of atmospheric mass-squared splitting with t2k and nova,” *arXiv preprint arXiv:1312.1477*, 2013.

[37] L. Stanco, “The next challenge for neutrinos: the mass ordering,” in *EPJ Web of Conferences*, vol. 164, p. 01031, EDP Sciences, 2017.

[38] D. Casper, “The nuance neutrino physics simulation, and the future,” *Nuclear Physics B-Proceedings Supplements*, vol. 112, no. 1-3, pp. 161–170, 2002.

[39] J. A. Formaggio and G. Zeller, “From ev to eev: Neutrino cross sections across energy scales,” *Reviews of Modern Physics*, vol. 84, no. 3, p. 1307, 2012.

[40] B. Povh, K. Rith, and F. Zetsche, *Particles and nuclei*, vol. 4. Springer, 1995.

[41] W. M. Alberico, A. Molinari, T. W. Donnelly, E. Kronenberg, and J. Van Orden, “Scaling in electron scattering from a relativistic fermi gas,” *Physical Review C*, vol. 38, no. 4, p. 1801, 1988.

[42] O. Benhar, A. Fabrocini, and S. Fantoni, “The nucleon spectral function in nuclear matter,” *Nuclear Physics A*, vol. 505, no. 2, pp. 267–299, 1989.

[43] R. Smith and E. J. Moniz, “Neutrino reactions on nuclear targets,” *Nuclear Physics B*, vol. 43, pp. 605–622, 1972.

[44] C. H. Llewellyn Smith, “Neutrino reactions at accelerator energies,” *Phys. Rept.*, vol. 3, no. SLAC-PUB-0958, pp. 261–379, 1971.

[45] S. Dolan, *Probing nuclear effects in neutrino-nucleus scattering at the T2K off-axis near detector using transverse kinematic imbalances.* PhD thesis, University of Oxford, 2017.

[46] D. Rein and L. M. Sehgal, "Neutrino-excitation of baryon resonances and single pion production," *Annals of Physics*, vol. 133, no. 1, pp. 79–153, 1981.

[47] N. N. Nikolaev and B. Zakharov, "Colour transparency and scaling properties of nuclear shadowing in deep inelastic scattering," in *30 Years Of The Landau Institute—Selected Papers*, pp. 733–744, World Scientific, 1996.

[48] H. Collaboration *et al.*, "Hadron formation in deep-inelastic positron scattering in a nuclear environment," *European Physical Journal C*, vol. 20, pp. 479–486, 2001.

[49] R. A. Bonham and M. Fink, *High energy electron scattering.* Van Nostrand Reinhold, 1974.

[50] S. Boyd, S. Dytman, E. Hernandez, J. Sobczyk, and R. Tacik, "Comparison of models of neutrino-nucleus interactions," in *AIP Conference Proceedings*, vol. 1189, pp. 60–73, AIP, 2009.

[51] P. de Perio, "Neut pion fsi," in *AIP Conference Proceedings*, vol. 1405, pp. 223–228, AIP, 2011.

[52] K. Abe, N. Abgrall, H. Aihara, Y. Ajima, J. Albert, D. Allan, P.-A. Amaudruz, C. Andreopoulos, B. Andrieu, M. Anerella, *et al.*, "The t2k experiment," *Nuclear Instruments and Methods in Physics Research Section A: Accelerators, Spectrometers, Detectors and Associated Equipment*, vol. 659, no. 1, pp. 106–135, 2011.

[53] H. Hotchi, M. Kinsho, K. Hasegawa, N. Hayashi, Y. Hikichi, S. Hiroki, J. Kamiya, K. Kanazawa, M. Kawase, F. Noda, *et al.*, "Beam commissioning of the 3-gev rapid cycling synchrotron of the japan proton accelerator research complex," *Physical Review Special Topics-Accelerators and Beams*, vol. 12, no. 4, p. 040402, 2009.

[54] Y. Ikeda, "J-parc status update," *Nuclear Instruments and Methods in Physics Research Section A: Accelerators, Spectrometers, Detectors and Associated Equipment*, vol. 600, no. 1, pp. 1–4, 2009.

[55] K. Abe *et al.*, "Observation of electron neutrino appearance in a muon neutrino beam," *Phys. Rev. Lett.*, vol. 112, p. 061802, Feb 2014.

[56] K. Abe, R. Akutsu, A. Ali, C. Alt, C. Andreopoulos, L. Anthony, M. Antonova, S. Aoki, A. Ariga, T. Arihara, Y. Asada, Y. Ashida, E. Atkin, *et al.*, "Constraint on the matter–antimatter symmetry-violating phase in neutrino oscillations," *Nature*, vol. 580, no. 7803, pp. 339–344, 2020.

[57] A. Blondel, M. Zito, and M. Yokoyama, "The t2k-nd280 upgrade proposal," tech. rep., 2018.

[58] K. Abe, J. Adam, H. Aihara, T. Akiri, C. Andreopoulos, S. Aoki, A. Ariga, S. Assylbekov, D. Autiero, M. Barbi, *et al.*, "Measurement of the inclusive electron neutrino charged current cross section on carbon with the t2k near detector," *Physical review letters*, vol. 113, no. 24, p. 241803, 2014.

[59] K. Abe, N. Abgrall, H. Aihara, T. Akiri, J. Albert, C. Andreopoulos, S. Aoki, A. Ariga, T. Ariga, S. Assylbekov, *et al.*, "T2k neutrino flux prediction," *Physical Review D*, vol. 87, no. 1, p. 012001, 2013.

[60] K. Matsuoka, A. Ichikawa, H. Kubo, K. Maeda, T. Maruyama, C. Matsumura, A. Murakami, T. Nakaya, K. Nishikawa, T. Ozaki, *et al.*, "Design and performance of the muon monitor for the t2k neutrino oscillation experiment," *Nuclear Instruments and Methods in Physics Research Section A: Accelerators, Spectrometers, Detectors and Associated Equipment*, vol. 624, no. 3, pp. 591–600, 2010.

[61] T2K beam group, "Flux release summary," Tech. Rep. 264, T2K, 2017. `https://www.t2k.org/docs/technotes/264/` (accessed January 2020).

[62] K. Abe, N. Abgrall, Y. Ajima, H. Aihara, J. Albert, C. Andreopoulos, B. Andrieu, M. Anerella, S. Aoki, O. Araoka, *et al.*, "First muon-neutrino disappear-

ance study with an off-axis beam," *Physical Review D*, vol. 85, no. 3, p. 031103, 2012.

[63] K. Abe, N. Abgrall, Y. Ajima, H. Aihara, J. Albert, C. Andreopoulos, B. Andrieu, M. Anerella, S. Aoki, O. Araoka, *et al.*, "Measurements of the t2k neutrino beam properties using the ingrid on-axis near detector," *Nuclear Instruments and Methods in Physics Research Section A: Accelerators, Spectrometers, Detectors and Associated Equipment*, vol. 694, pp. 211–223, 2012.

[64] N. Chikuma, A. Izamaylov, F. Hosomi, *et al.*, "A new water target neutrino detector at on-axis," Tech. Rep. 259, T2K, 2015. `https://www.t2k.org/docs/technotes/259/` (accessed January 2020).

[65] S. Assylbekov, G. Barr, B. Berger, H. Berns, D. Beznosko, A. Bodek, R. Bradford, N. Buchanan, H. Budd, Y. Caffari, *et al.*, "The t2k nd280 off-axis pi–zero detector," *Nuclear Instruments and Methods in Physics Research Section A: Accelerators, Spectrometers, Detectors and Associated Equipment*, vol. 686, pp. 48–63, 2012.

[66] M. Day, S. Manly, K. McFarland, P. Rodrigues, and I. Taylor, "Crosscheck of high-energy nue event rate with the p0d," Tech. Rep. 053, T2K, 2012. `https://www.t2k.org/docs/technotes/053/` (accessed January 2020).

[67] N. Abgrall, B. Andrieu, P. Baron, P. Bene, V. Berardi, J. Beucher, P. Birney, F. Blaszczyk, A. Blondel, C. Bojechko, *et al.*, "Time projection chambers for the t2k near detectors," *Nuclear Instruments and Methods in Physics Research Section A: Accelerators, Spectrometers, Detectors and Associated Equipment*, vol. 637, no. 1, pp. 25–46, 2011.

[68] I. Giomataris, R. De Oliveira, S. Andriamonje, S. Aune, G. Charpak, P. Colas, G. Fanourakis, E. Ferrer, A. Giganon, P. Rebourgeard, *et al.*, "Micromegas in a bulk," *Nuclear Instruments and Methods in Physics Research Section A: Accelerators, Spectrometers, Detectors and Associated Equipment*, vol. 560, no. 2, pp. 405–408, 2006.

[69] Y. Giomataris, P. Rebourgeard, J. P. Robert, and G. Charpak, "Micromegas: a high-granularity position-sensitive gaseous detector for high particle-flux environments," *Nuclear Instruments and Methods in Physics Research Section A: Accelerators, Spectrometers, Detectors and Associated Equipment*, vol. 376, no. 1, pp. 29–35, 1996.

[70] M. Nirkko, "Measurement of the k^+ production cross section from charged current ν_μ interactions in hydrocarbon at the t2k near detector," Tech. Rep. 278, T2K, 2016. `https://www.t2k.org/docs/technotes/278/` (accessed January 2020).

[71] P.-A. Amaudruz, M. Barbi, D. Bishop, N. Braam, D. Brook-Roberge, S. Giffin, S. Gomi, P. Gumplinger, K. Hamano, N. Hastings, *et al.*, "The t2k fine-grained detectors," *Nuclear Instruments and Methods in Physics Research Section A: Accelerators, Spectrometers, Detectors and Associated Equipment*, vol. 696, pp. 1–31, 2012.

[72] A. Vacheret, G. J. Barker, M. Dziewiecki, P. Guzowski, M. D. Haigh, B. Hartfiel, A. Izmaylov, W. Johnston, M. Khabibullin, A. Khotjantsev, *et al.*, "Characterization and simulation of the response of multi-pixel photon counters to low light levels," *Nuclear Instruments and Methods in Physics Research Section A: Accelerators, Spectrometers, Detectors and Associated Equipment*, vol. 656, no. 1, pp. 69–83, 2011.

[73] K. Yamamoto, K. Yamamura, K. Sato, S. Kamakura, T. Ota, H. Suzuki, and S. Ohsuka, "Development of multi-pixel photon counter (mppc)," in *2007 IEEE Nuclear Science Symposium Conference Record*, vol. 2, pp. 1511–1515, IEEE, 2007.

[74] S. Gomi, H. Hano, T. Iijima, S. Itoh, K. Kawagoe, S. Kim, T. Kubota, T. Maeda, T. Matsumura, Y. Mazuka, *et al.*, "Development and study of the multi pixel photon counter," *Nuclear Instruments and Methods in Physics Research Section A: Accelerators, Spectrometers, Detectors and Associated Equipment*, vol. 581, no. 1-2, pp. 427–432, 2007.

[75] D. Allan, C. Andreopoulos, C. Angelsen, G. Barker, G. Barr, S. Bentham, I. Bertram, S. Boyd, K. Briggs, R. Calland, *et al.*, "The electromagnetic calorimeter for the t2k near detector nd280," *Journal of Instrumentation*, vol. 8, no. 10, p. P10019, 2013.

[76] L. H. Whitehead, *A Measurement of the Electron Neutrino Component of the T2K Beam using the Near Detector*. PhD thesis, University of Warwick, 2012.

[77] M. Calvetti, P. Cennini, S. Centro, S. Cittolin, D. DiBitonto, L. Dumps, W. Haynes, W. Jank, G. Jorat, V. Karimaki, *et al.*, "First operation of the cern ua1 central detector," *IEEE Transactions on Nuclear Science*, vol. 30, no. 1, pp. 71–75, 1983.

[78] F. Vannucci, "The nomad experiment at cern," *Advances in High Energy Physics*, vol. 2014, 2014.

[79] S. Aoki, G. Barr, M. Batkiewicz, J. Błocki, J. Brinson, W. Coleman, A. Dabrowska, I. Danko, M. Dziewiecki, B. Ellison, *et al.*, "The t2k side muon range detector (smrd)," *Nuclear Instruments and Methods in Physics Research Section A: Accelerators, Spectrometers, Detectors and Associated Equipment*, vol. 698, pp. 135–146, 2013.

[80] S. Fukuda, Y. Fukuda, T. Hayakawa, E. Ichihara, M. Ishitsuka, Y. Itow, T. Kajita, J. Kameda, K. Kaneyuki, S. Kasuga, *et al.*, "The super-kamiokande detector," *Nuclear Instruments and Methods in Physics Research Section A: Accelerators, Spectrometers, Detectors and Associated Equipment*, vol. 501, no. 2-3, pp. 418–462, 2003.

[81] Y. Itow, T. Kajita, K. Kaneyuki, M. Shiozawa, Y. Totsuka, Y. Hayato, T. Ishida, T. Ishii, T. Kobayashi, T. Maruyama, *et al.*, "The jhf-kamioka neutrino project," *arXiv preprint hep-ex/0106019*, 2001.

[82] X. Li, H. He, G. Xiao, X. Zuo, S. Feng, L. Wang, C. Li, M. Saeed, Z. Cao, X. Sheng, *et al.*, "Novel methods for measuring the optical parameters of the water cherenkov detector," *Nuclear Instruments and Methods in Physics*

Research Section A: Accelerators, Spectrometers, Detectors and Associated Equipment, vol. 919, pp. 73–81, 2019.

[83] S. Choubey and S. Petcov, “Reactor antineutrino oscillations and gadolinium loaded super-kamiokande detector,” *Physics Letters B*, vol. 594, no. 3-4, pp. 333–346, 2004.

[84] S. Ito, “Current status and future prospect of super-kamiokande,” *PoS*, p. 049, 2018.

[85] K. Abe, R. Akutsu, A. Ali, J. Amey, C. Andreopoulos, L. Anthony, M. Antonova, S. Aoki, A. Ariga, Y. Ashida, *et al.*, “Search for c p violation in neutrino and antineutrino oscillations by the t2k experiment with 2.2× 10 21 protons on target,” *Physical review letters*, vol. 121, no. 17, p. 171802, 2018.

[86] G. Christodoulou and S. King, “Measurement of electron (anti-)neutrino cross-sections in the nd280 tracker using (anti-)neutrino beam data up to run 8,” Tech. Rep. 277, T2K, 2020. `https://www.t2k.org/docs/technotes/277/` (accessed March 2020).

[87] G. Christodoulou, B. Jamieson, S. King, P. Lasorak, and N. McCauley, “Measurement of electron (anti-)neutrino cross-sections in the nd280 tracker using (anti-)neutrino beam data up to run 8,” Tech. Rep. 282, T2K, 2016. `https://www.t2k.org/docs/technotes/282/` (accessed March 2020).

[88] K. Abe, R. Akutsu, A. Ali, C. Alt, C. Andreopoulos, L. Anthony, M. Antonova, S. Aoki, A. Ariga, T. Arihara, *et al.*, “Measurement of the charged-current electron (anti-) neutrino inclusive cross-sections at the t2k off-axis near detector nd280,” *arXiv preprint arXiv:2002.11986*, 2020.

[89] A. Izmaylov, “Highland tutorial.” `http://www.t2k.org/nd280/physics/xsec/meetings/2017/workshop/talks/highland/view`, June 2017. Accessed: March 2020.

[90] C. Bojechko *et al.*, “Cc-multiple-pion ν_μ event selections in the nd280 tracker

using run 1+2+3+4 data," Tech. Rep. 152, T2K, 2013. `https://www.t2k.org/docs/technotes/152/` (accessed July 2020).

[91] J. Caravaca, G. Christodoulou, C. Giganti, D. Hadley, E. Larkin, N. McCauley, B. Sgalaberna, D. Smith, P. Stamoulis, and C. Wilkinson, "Measurement of the electron neutrino beam component in the nd280 tracker for 2013 analyses," Tech. Rep. 149, T2K, 2014. `https://www.t2k.org/docs/technotes/149/` (accessed April 2020).

[92] C. Giganti and M. Zito, "Particle identification with the t2k tpc," Tech. Rep. 001, T2K, 2009. `https://www.t2k.org/docs/technotes/001/` (accessed April 2020).

[93] C. Giganti, "The tpc beam test: Pid studies," Tech. Rep. 003, T2K, 2009. `https://www.t2k.org/docs/technotes/003/` (accessed April 2020).

[94] K. Abe, J. Adam, H. Aihara, T. Akiri, C. Andreopoulos, S. Aoki, A. Ariga, S. Assylbekov, D. Autiero, M. Barbi, *et al.*, "Measurement of the ν μ charged-current quasielastic cross section on carbon with the nd280 detector at t2k," *Physical Review D*, vol. 92, no. 11, p. 112003, 2015.

[95] E. Frank, A. Marchionni, and M. Messina, "B-field calibration and systematic errors," Tech. Rep. 081, T2K, 2010. `https://www.t2k.org/docs/technotes/081/` (accessed May 2020).

[96] L. Escudero, C. Bojechko, *et al.*, "Measurement and correction of magnetic field distortions in the time projection chambers," Tech. Rep. 061, T2K, 2011. `https://www.t2k.org/docs/technotes/061/` (accessed May 2020).

[97] D. Brailsford, A. Chappell, P. Denner, D. R. Hadley, P. Martins, G. Christodoulou, S. King, and I. Lamont, "Study of the tracker ecal systematic uncertainties," Tech. Rep. 279, T2K, 2017. `https://www.t2k.org/docs/technotes/279/` (accessed May 2020).

[98] F. Sanchez and J. Medina, "Nd280 global charge identification systematic error,"

Tech. Rep. 229, T2K, 2016. https://www.t2k.org/docs/technotes/229/ (accessed May 2020).

[99] A. Hillairet, T. Lindner, J. Myslik, and P. Stamoulis, "Nd280 tracker tracking efficiency," Tech. Rep. 075, T2K, 2012. https://www.t2k.org/docs/technotes/075/ (accessed May 2020).

[100] K. Mahn, S. Oser, and T. Lindner, "Fgd mass checks," Tech. Rep. 122, T2K, 2012. https://www.t2k.org/docs/technotes/122/ (accessed May 2020).

[101] T. Feusels, A. Fiorentini, E. S. Pinzon Guerra, C. Wilkinson, and M. Yu, "Tuning of the neut cascade model using $\pi^{\pm}$-a scattering external data to improve final state interaction and secondary interaction systematic uncertainties," Tech. Rep. 325, T2K, 2017. https://www.t2k.org/docs/technotes/325/ (accessed May 2020).

[102] S. Agostinelli, J. Allison, K. a. Amako, J. Apostolakis, H. Araujo, P. Arce, M. Asai, D. Axen, S. Banerjee, G. . Barrand, *et al.*, "Geant4—a simulation toolkit," *Nuclear instruments and methods in physics research section A: Accelerators, Spectrometers, Detectors and Associated Equipment*, vol. 506, no. 3, pp. 250–303, 2003.

[103] T. Katori and P. Lasorak, "A detector systematic error for out of fgd1 fiducial volume photons," Tech. Rep. 313, T2K, 2017. https://www.t2k.org/docs/technotes/313/ (accessed July 2020).

[104] M. Rovanel, J. Lagoda, *et al.*, "ν_μ cc event selections in the nd280 tracker using run 2+3+4 data," Tech. Rep. 212, T2K, 2015. https://www.t2k.org/docs/technotes/212/ (accessed May 2020).

[105] T2K NIWG Group, "2018-2019 xsec-niwg inputs." https://www.t2k.org/nd280/physics/xsec/docs/xsec-niwg-doc/xsecniwg2018, July 2019. Accessed: May 2020.

[106] A. Bercellie, , Y. Hayato, K. Ieki, A. Kaboth, K. Mahn, K. McFarland, P. Rodrigues, R. Terri, M. Wascko, and C. Wilkinson, "Cross section parameters

for 2014 oscillation analysis," Tech. Rep. 192, T2K, 2014. https://www.t2k.org/docs/technotes/192/ (accessed May 2020).

[107] E. T. Atkin, S. Bolognesi, S. Dolan, P. Dunne, Y. Hayato, K. McFarland, L. Munteanu, W. Parker, L. Pickering, K. Wood, C. Wret, and M. Yu, "Niwg model and uncertainties for 2019-2020 oscillation analysis," Tech. Rep. 344, T2K, 2019. https://www.t2k.org/docs/technotes/344/ (accessed May 2020).

[108] P. de Perio, M. Hartz, Y. Hayato, K. Mahn, K. McFarland, P. Rodrigues, P. Sinclair, R. Terri, and M. Wascko, "Cross section parameters for 2012 oscillation analysis," Tech. Rep. 108, T2K, 2012. https://www.t2k.org/docs/technotes/108/ (accessed May 2020).

[109] E. P. Guerra, S. Bhadra, S. Berkman, C. Cao, P. de Perio, Y. Hayato, K. Ieki, M. Ikeda, Y. Kanazawa, J. Kim, *et al.*, "Measurement of σ abs and σ cx of $\pi+$ on carbon by the dual use experiment at triumf (duet)," *Physical Review C*, vol. 95, no. 4, p. 045203, 2017.

[110] A. Ferrari, P. R. Sala, A. Fasso, and J. Ranft, "Fluka: A multi-particle transport code (program version 2005)," tech. rep., 2005.

[111] G. Battistoni, F. Cerutti, A. Fasso, A. Ferrari, S. Muraro, J. Ranft, S. Roesler, and P. Sala, "The fluka code: Description and benchmarking," in *AIP Conference proceedings*, vol. 896, pp. 31–49, American Institute of Physics, 2007.

[112] R. Brun, A. McPherson, P. Zanarini, M. Maire, and F. Bruyant, "Geant 3: user's guide geant 3.10, geant 3.11," tech. rep., CERN, 1987.

[113] C. Zeitnitz and T. Gabriel, "The geant-calor interface user's guide," 1996.

[114] J. Myslik, "Selected results from t2k," 2015.

[115] N. Abgrall, A. Aduszkiewicz, B. Andrieu, T. Anticic, N. Antoniou, J. Argyriades, A. Asryan, B. Baatar, A. Blondel, J. Blumer, *et al.*, "Measurements of cross sections and charged pion spectra in proton-carbon interactions at 31 gev/c," *Physical Review C*, vol. 84, no. 3, p. 034604, 2011.

[116] A. Fiorentini, M. Friend, A. Haesler, M. Hartz, A. K. Ichikawa, S. Johnson, A. Korzenev, K. Kowalik, A. Missert, T. Nakadaira, B. Popov, K. Sakashita, K. Suzuki, T. Hiraki, M. Posiadala-Zezula, D. Sgalaberna, M. Tzanov, M. Yu, T. Vladisavljevic, and L. Zambelli, "Flux prediction and uncertainty updates with na61 2009 thin 2 target data and negative focussing mode predictions," Tech. Rep. 217, T2K, 2018. `https://www.t2k.org/docs/technotes/217/` (accessed May 2020).

[117] C. Andreopoulos, A. Bell, D. Bhattacharya, F. Cavanna, J. Dobson, S. Dytman, H. Gallagher, P. Guzowski, R. Hatcher, P. Kehayias, *et al.*, "The genie neutrino monte carlo generator," *Nuclear Instruments and Methods in Physics Research Section A: Accelerators, Spectrometers, Detectors and Associated Equipment*, vol. 614, no. 1, pp. 87–104, 2010.

[118] T. Golan, J. Sobczyk, and J. Żmuda, "Nuwro: the wrocław monte carlo generator of neutrino interactions," *Nuclear Physics B-Proceedings Supplements*, vol. 229, p. 499, 2012.

[119] K. Abe, I. Anghel, S. Playfer, O. Drapier, J. Kameda, S. Kim, M. Barbi, C. Checchia, A. Kaboth, S. Tobayama, *et al.*, "Hyper-kamiokande design report," tech. rep., 2018.

[120] S.-B. Kim, "New results from reno and prospects with reno-50," *arXiv preprint arXiv:1412.2199*, 2014.

[121] F. An, G. An, Q. An, V. Antonelli, E. Baussan, J. Beacom, L. Bezrukov, S. Blyth, R. Brugnera, M. B. Avanzini, *et al.*, "Neutrino physics with juno," *Journal of Physics G: Nuclear and Particle Physics*, vol. 43, no. 3, p. 030401, 2016.

[122] A. Kumar, A. V. Kumar, A. Jash, A. K. Mohanty, A. Chacko, A. Ajmi, A. Ghosal, A. Khatun, A. Raychaudhuri, A. Dighe, *et al.*, "Invited review: Physics potential of the ical detector at the india-based neutrino observatory (ino)," *Pramana*, vol. 88, no. 5, p. 79, 2017.

[123] W. Winter, "Neutrino mass hierarchy determination with icecube-pingu," *Physical Review D*, vol. 88, no. 1, p. 013013, 2013.

[124] M. Ribordy and A. Y. Smirnov, "Improving the neutrino mass hierarchy identification with inelasticity measurement in pingu and orca," *Physical Review D*, vol. 87, no. 11, p. 113007, 2013.

[125] P. Harrison, D. H. Perkins, and W. Scott, "A redetermination of the neutrino mass-squared difference in tri-maximal mixing with terrestrial matter effects," *Physics Letters B*, vol. 458, no. 1, pp. 79–92, 1999.

[126] A. Renshaw, K. Abe, Y. Hayato, K. Iyogi, J. Kameda, Y. Kishimoto, M. Miura, S. Moriyama, M. Nakahata, Y. Nakano, *et al.*, "First indication of terrestrial matter effects on solar neutrino oscillation," *Physical review letters*, vol. 112, no. 9, p. 091805, 2014.

[127] H.-K. Proto-Collaboration, K. Abe, H. Aihara, C. Andreopoulos, I. Anghel, A. Ariga, T. Ariga, R. Asfandiyarov, M. Askins, J. Back, *et al.*, "Physics potential of a long-baseline neutrino oscillation experiment using a j-parc neutrino beam and hyper-kamiokande," *Progress of theoretical and experimental physics*, vol. 2015, no. 5, p. 053C02, 2015.

[128] T. Koseki, "J-parc accelerator: status, capacity and future plan." Talk presented at the Workshop for Neutrino Programs with Facilities in Japan, Tokai, Japan, 2014.

[129] T. Koseki, "J-parc accelerator: achievement and future upgrade." Talk presented at the Workshop for Neutrino Programs with Facilities in Japan, Tokai, Japan, 2015.

[130] T. Kobayashi, "Potential j-parc beam power improvement and beam delivery before 2026." Talk presented at the Workshop for Neutrino Programs with Facilities in Japan, Tokai, Japan, 2015.

[131] S. Igarashi, H. Harada, H. Hotchi, T. Koseki, and Y. Sato, "Accelerator concepts for the beam power of multi mw with j-parc mr," in *Proceedings of the*

2nd International Symposium on Science at J-PARC—Unlocking the Mysteries of Life, Matter and the Universe—, p. 012018, 2015.

[132] K. Abe, M. Smy, P. Hamacher-Baumann, E. Mazzucato, C. Densham, R. Owen, W. Ceria, R. Shah, H. Kakuno, H. O'Keeffe, *et al.*, "T2k nd280 upgrade-technical design report," tech. rep., 2019.

[133] R. Asfandiyarov, R. Bayes, A. Blondel, M. Bogomilov, A. Bross, F. Cadoux, A. Cervera, A. Izmaylov, Y. Karadzhov, I. Karpikov, *et al.*, "Proposal for sps beam time for the baby mind and tasd neutrino detector prototypes," *arXiv preprint arXiv:1405.6089*, 2014.

[134] R. Tamura, N. Chikuma, T. Koga, M. Yokoyama, M. Antonova, A. Izmaylov, M. Khabibullin, A. Khotjantsev, A. Kostin, Y. Kudenko, *et al.*, "Development of a neutrino detector and electronics for precise measurement of neutrino cross-section ratios," in *2017 IEEE Nuclear Science Symposium and Medical Imaging Conference (NSS/MIC)*, pp. 1–5, IEEE, 2017.

[135] K. Abe, J. Adam, H. Aihara, T. Akiri, C. Andreopoulos, S. Aoki, A. Ariga, S. Assylbekov, D. Autiero, M. Barbi, *et al.*, "Measurement of the inclusive ν μ charged current cross section on iron and hydrocarbon in the t2k on-axis neutrino beam," *Physical Review D*, vol. 90, no. 5, p. 052010, 2014.

[136] M. Scott, "An intermediate water cherenkov detector at j-parc," in *Proceedings of the 10th International Workshop on Neutrino-Nucleus Interactions in Few-GeV Region (NuInt15)*, p. 010039, 2016.

[137] S. Bhadra, A. Blondel, S. Bordoni, A. Bravar, C. Bronner, J. Caravaca-Rodriguez, M. Dziewiecki, T. Feusels, G. Fiorentini-Aguirre, M. Friend, *et al.*, "Letter of intent to construct a nuprism detector in the j-parc neutrino beamline," *arXiv preprint arXiv:1412.3086*, 2014.

[138] C. Athanassopoulos, L. Auerbach, R. Burman, D. Caldwell, E. Church, I. Cohen, J. Donahue, A. Fazely, F. Federspiel, G. Garvey, *et al.*, "Evidence for nu_mu-¿ nu_e neutrino oscillations from lsnd," *arXiv preprint nucl-ex/9709006*, 1997.

[139] A. Aguilar-Arevalo, C. Anderson, L. Bartoszek, A. Bazarko, S. Brice, B. Brown, L. Bugel, J. Cao, L. Coney, J. Conrad, *et al.*, "The miniboone detector," *Nuclear Instruments and Methods in Physics Research Section A: Accelerators, Spectrometers, Detectors and Associated Equipment*, vol. 599, no. 1, pp. 28–46, 2009.

[140] A. Aguilar-Arevalo, B. Brown, L. Bugel, G. Cheng, E. Church, J. Conrad, R. Dharmapalan, Z. Djurcic, D. Finley, R. Ford, *et al.*, "Improved search for $\nu\ \mu\rightarrow\ \nu$ e oscillations in the miniboone experiment," *Physical review letters*, vol. 110, no. 16, p. 161801, 2013.

[141] M. Scott, N. Collaboration, *et al.*, "Oscillation analysis with nuprism," in *Journal of Physics: Conference Series*, vol. 888, p. 012165, IOP Publishing, 2017.

[142] H. Watanabe *et al.*, "Super-kamiokande coll," *Astrop. Phys*, vol. 31, pp. 320–328, 2009.

[143] J. Alonso, N. Barros, M. Bergevin, A. Bernstein, L. Bignell, E. Blucher, F. Calaprice, J. Conrad, F. Descamps, M. Diwan, *et al.*, "Advanced scintillator detector concept (asdc): a concept paper on the physics potential of water-based liquid scintillator," *arXiv preprint arXiv:1409.5864*, 2014.

[144] K. Abe, H. Aihara, C. Andreopoulos, I. Anghel, A. Ariga, T. Ariga, R. Asfandiyarov, M. Askins, J. Back, P. Ballett, *et al.*, "A long baseline neutrino oscillation experiment using j-parc neutrino beam and hyper-kamiokande," *arXiv preprint arXiv:1412.4673*, 2014.

[145] P. Lasorak and N. Prouse, "Titus: An intermediate distance detector for the hyper-kamiokande neutrino beam," *arXiv preprint arXiv:1504.08272*, 2015.

[146] A. Suzuki, M. Mori, K. Kaneyuki, T. Tanimori, J. Takeuchi, H. Kyushima, and Y. Ohashi, "Improvement of 20 in. diameter photomultiplier tubes," *Nuclear Instruments and Methods in Physics Research Section A: Accelerators, Spectrometers, Detectors and Associated Equipment*, vol. 329, no. 1-2, pp. 299–313, 1993.

[147] H. Suzuki, “Physics and astrophysics of neutrinos,” *Springer-Verlag, Berlin*, vol. 763, 1994.

[148] Y. Fukuda *et al.*, “Nucl. instrum & meth,” *A501*, vol. 418, 2003.

[149] K. Abe, Y. Hayato, T. Iida, K. Iyogi, J. Kameda, Y. Kishimoto, Y. Koshio, L. Marti, M. Miura, S. Moriyama, *et al.*, “Calibration of the super-kamiokande detector,” *Nuclear Instruments and Methods in Physics Research Section A: Accelerators, Spectrometers, Detectors and Associated Equipment*, vol. 737, pp. 253–272, 2014.

[150] “The hyper-kamiokande project is officially approved: Press release.” `https://www.interactions.org/press-release/hyper-kamiokande-project-officially-approved`. Accessed: 2020-03-08.

[151] W. G. Vinning, “The narrow-beam diffuser subsystem of a prototype optical calibration system for the hyper-kamiokande detector,” *arXiv preprint arXiv:1904.01660*, 2019.

[152] S. A. Arduino, “Arduino,” *Arduino LLC*, 2015.

[153] Y. A. Badamasi, “The working principle of an arduino,” in *2014 11th international conference on electronics, computer and computation (ICECCO)*, pp. 1–4, IEEE, 2014.

[154] S. Valder, “Diffuser research and development for optical calibration systems in hyper-kamiokande,” *arXiv preprint arXiv:1904.06201*, 2019.

[155] G. W. Johnson, *LabVIEW graphical programming.* Tata McGraw-Hill Education, 1997.

[156] A. Mitra and K. Jewkes. Private Communication.

[157] W. G. S. Vinning. Private Communication.

[158] G. Venkateswarlu, R. Sharada, and R. Bhagvanth, “Polytetrafluoroethylene (ptfe) based composites,” *Journal of Chemical and Pharmaceutical Research*, vol. 6, no. 10, pp. 508–517, 2014.

[159] M. Glück, E. Reya, and A. Vogt, "Dynamical parton distributions revisited," *The European Physical Journal C-Particles and Fields*, vol. 5, no. 3, pp. 461–470, 1998.

[160] A. Bodek and U. Yang, "Modeling neutrino and electron scattering cross sections in the few gev region with effective lo pdfs," in *AIP Conference Proceedings*, vol. 670, pp. 110–117, American Institute of Physics, 2003.

[161] K. Graczyk, D. Kiełczewska, P. Przewłocki, and J. Sobczyk, "C 5 a axial form factor from bubble chamber experiments," *Physical Review D*, vol. 80, no. 9, p. 093001, 2009.

[162] P. Bartet, A. Garcia, F. Sanchez, A. Hillairet, A. Izmaylov, J. Lagoda, L. Magaletti, and J. Wilson, "ν_μ cc event selections in the nd280 tracker using run 2+3+4 data," Tech. Rep. 245, T2K, 2017. `https://www.t2k.org/docs/technotes/245/` (accessed July 2020).

[163] W. Oryszczak and W. Warzycha, "Fgd systematics: Pid and isorecon hybrid efficiency," Tech. Rep. 223, T2K, 2015. `https://www.t2k.org/docs/technotes/223/` (accessed July 2020).